Study of electrical properties of a-Si:H Hetro-junction solar cells and metal-oxide nano-fibers based photo-anode for application in advance generation solar cells.

Maham Akhlaq

NUST-MS Energy Systems Engineering- 00000119773

Session 2015-17

Supervisor

Dr. Zuhair S. Khan

U.S. Pakistan Center for Advanced Studies in Energy Systems (USPCAS-E)

National University of Sciences and Technology (NUST)

H-12, Islamabad 44000, Pakistan

Study of electrical properties of a-Si:H Hetro-junction solar cells and metal-oxide nano-fibers based photo-anode for application in advance generation solar cells.

Maham Akhlaq

NUST-MS Energy Systems Engineering- 00000119773

Session 2015-17

Supervised by

Dr. Zuhair S. Khan

A Thesis Submitted to the Centre for Energy Systems in partial fulfillment of the requirements for the degree of

MASTERS of Science in

ENERGY SYSTEMS ENGINEERING

U.S. Pakistan Center for Advanced Studies in Energy Systems (USPCAS-E)

National University of Sciences and Technology (NUST)

H-12, Islamabad 44000, Pakistan

Feburary 2018

THESIS ACCEPTANCE CERTIFICATE

It is certified that final copy of MS/MPhil thesis written by Ms. Maham Akhlaq (Registration No. NUST-MS Energy Systems Engineering-00000119773) of USPCAS-E (School/College/Institute) has been vetted by undersigned, found complete in all respects as per NUST Statues/Regulations, is free of plagiarism, errors, and mistakes and is accepted as partial fulfillment for award of MS/MPhil degree. It is further certified that necessary amendments as pointed out by GEC members of the scholar have also been incorporated in the said thesis.

Signature:

Name of Supervisor

Date:

Signature (HoD):

Date:

Signature (Dean/Principal):

Date:

Certificate

This is to certify that work in this thesis has been carried out by **Ms. Maham Akhlaq** and completed under my supervision in Advanced Energy Materials & Systems (AEMS) Laboratory, U.S. Pakistan Center for Advanced Studies in Energy (USPCAS-E), National University of Sciences and Technology, H-12, Islamabad, Pakistan.

Supervisor: _____

Dr. Zuhair S. Khan
USPCAS-E
NUST, Islamabad

GEC member # 1: _____

Dr. M. Pervez Akhtar
USPCAS-E
NUST, Islamabad

GEC member # 2: _____

Dr. Nadia Shahzad
USPCAS-E
NUST, Islamabad

GEC member # 3: _____

Dr. Sofia Javed
SCME
NUST, Islamabad

HoD _____

Dr. Naseem Iqbal
USPCAS-E
NUST, Islamabad

Principal/ Dean _____

Dr. Zuhair S. Khan
USPCAS-E
NUST, Islamabad

ABSTRACT:

Increase in world energy crisis and depletion of conventional energy resources are some of the major issue the world is facing nowadays. To mitigate the utilization of conventional energy and to overcome these energy crises, alternate and sustainable energy resources are obligatory. One of the potential ways is to use renewable energy resources. Among Renewable energy resources, photo-voltaic technology is an efficient one because of the availability of surplus amount of solar light. Solar cells consist of 3 major generation based on the materials used for generation of electron-hole pair. Among 2^{nd} generation solar cells, a-Si:H hetro-junction solar cells are an efficient type of solar cells that have currently obtained exceptional power conversion efficiency. But due high contact resistance on the surface of such solar cells, the theoretical efficiency has not been achieved yet. Similarly 3^{rd} generation Dye-sensitized solar cells are among the top candidate for solar cells with easy and low cost for fabrication. Among various components of DSSC, photo-anode is one of the most dominant component for which various metal oxide nano-structures are used. These nano-structures include nano-particles, nano-rods and nano-fibres. Metal oxide nano-fibres are been currently used in DSSC as photo-anode to obtain large-surface area to volume ratio for better electron transport. Among these Titania is widely used but because of the issues like recombination of electron-hole pair, composite of Titania and other metal oxides is used. In this work, transfer length measurement (TLM) pattern cells were successfully prepared using PECVD and RF sputtering. Different layer of a-Si:H hetro-junction were varied to study their effects on contact resistance. TLM pattern consist of multiple spacing between metal contacts. The effect of varing p a-Si:H layer, varing i-layer thickness with no p- a-Si:H layer, effect of annealing temperature and TMB flow in PECVD chamber was studied. Similarly electrical properties of indium oxide (IO) were also studied as transparent conductive oxide (TCO), which shows that increase in sputtering time increases the thickness of the deposited film which results in the increase in mobility and decrease in sheet resistance under constant Ar, oxygen and vacuum. With change in oxygen concentration thickness and carrier concentration decreases but mobility increases because of formation of grain size defects. Likewise, TiO_2 nano-fibres, SnO_2 nano-fibres and TiO_2-SnO_2 nano-fibres by using Poly-vinyl pyrollidone were

successfully synthesized using Electro-spinning for photo-anode of DSSC. Solution electro-spinning and co-axial electro-spinning was used to synthesize the fibers. The structural, optical and electrical properties of the prepared nano-fibres were carried out by the diversified techniques including X-ray diffraction, Scanning Electron microscopy, Fourier transform infrared spectroscopy, UV-VIS NIR spectrophotometer and Hall Effect measurement system. The effect of polymer concentration was studied which shows that with increase in polymer, the diameter of the fiber increases. The prepared TiO_2-SnO_2 film has more conductivity and have higher band-gap then bare TiO_2 nano-fibres. More-over the prepared films were successfully sensitized by using graphene nano-platelets using Di-methyl formamide (DMF) as a solvent. Graphene sensitization not only increases the conductivity of the film but also increases the band-gap. One of the draw-back of graphene sensitized nano-fibers is that it gives absorption in UV- region.

Keywords: a-Si:H Hetro-junction solar cells, Dye-sensitized solar cells, nano-fibres, TiO_2-SnO_2 composite, electro-spinning.

Table of Contents

Table of Figures

Table of Tables

List of Abbreviations:

SEM – Scanning Electron Microscopy

EDX – Energy dispersive X-ray spectroscopy

FT-IR – Fourier transformed infrared spectroscopy

Voc – open circuit voltage

Isc - Short circuit current

DSSC – dye-sensitized solar cells

a-Si:H – hydrogenated amorphous silicon

XRD – X-ray diffraction

PVP – Poly-vinyl pyrrolidone

List of Journal/Conference Papers

Original Research article: Maham Akhlaq , Nadia Shahzad , Zuhair S.Khan , 'Synthesis and characterization of Electro-spun TiO_2-SnO_2 composite nano-fibers for application in advance generation solar cells' to be submitted in June

*Conference Paper: Maham Akhlaq , Hina Pervaiz , Zuhair S.Khan, "Synthesis and characterization of TiO2 nano-fibres on FTO glass via Electro-spinning" , *Presented at 3rd Conference on Emerging Materials and Processes* (SCME), NUST, Islamabad.

Conference Paper: The influence of different electrophoretic deposition (EPD) parameters on thickness of Titanium dioxide (TiO_2) film", *Presented at 3rd Conference on Emerging Materials and Processes* (SCME), NUST, Islamabad. (2nd Author)

*Attached as Annexure I

CHAPTER 1

INTRODUCTION:

1.1 Energy Crisis:

The energy crisis of the world is the concern as the demands on the limited natural/conventional resources that are used to power industrial and domestic society are deteriorating. Current Energy demand of the world is increasing rapidly. The growing population, heavy industrialization and changing landscape of cities have increased energy demands immensely. The reasons behind this crisis include over-consumption, over-population, poor infrastructure, wastage of energy and unexplored renewable energy options. Currently the energy demand is 13 TWh which is predicted to rise to 25 TWh by 2050[1]. 80% of this energy demand of the world is met by using fossil fuel[2]. Due to rapid decline in fossil fuel resources, the costs of obtaining fuels both from domestic and foreign sources will increase rapidly. If current patterns continue for a while, fuel costs are expected to double or triple in a decade and the increase in the cost fivefold nearly by a century.

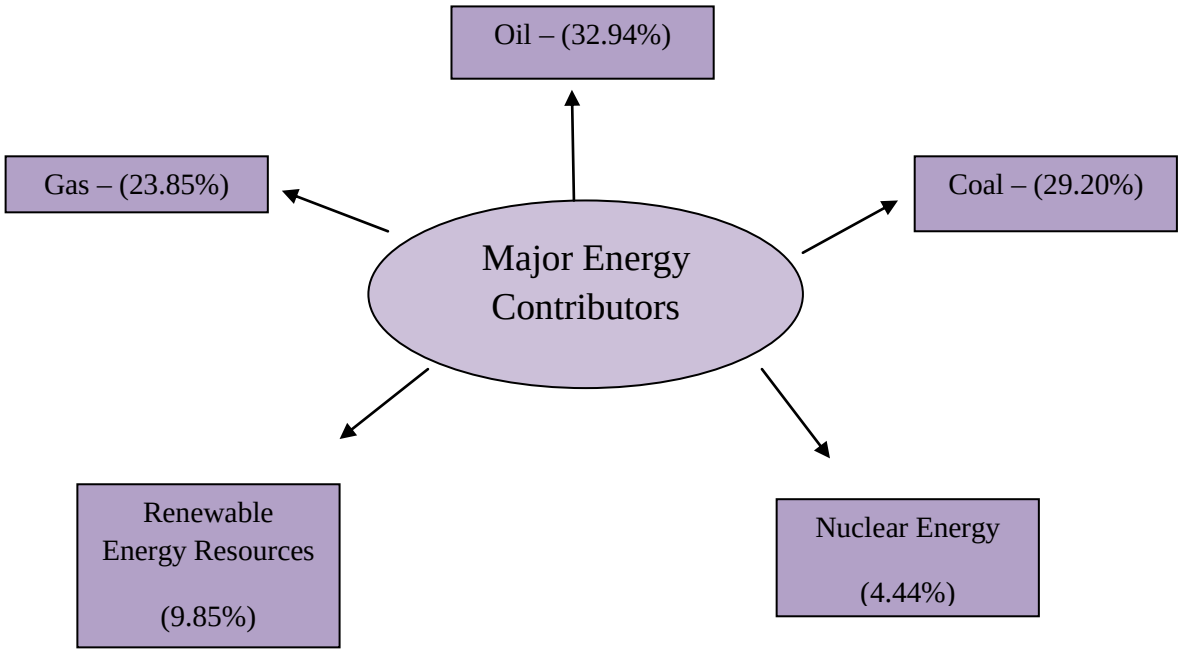

Figure 1.1 Percentage of major energy contributor towards Energy sector of the world.

‘Fossil fuels are not only causing environmental issue (because of CO_2 emissions), but are also depleting with time. Because of this increasing energy demand and fossil fuels related issues, there is a need of a sustainable energy technology Governments and concerned energy authorities are working to make the use of alternative fuels like renewable resources a priority, and to lessen the negligent use of natural supplies through increased conservation of those energy supplies. Renewable energy includes a collection of energy technologies i.e. solar, wind, bio-fuel, geothermal acquired from sources that are never-ending and can be replenished time after time. There is a massive amount of energy that can be produced by renewable energy resources. Renewable energy not only helps contribute to the world energy crisis but it is sustainable and eco-friendly (zero gas emissions).

1.2 Renewable and Conventional Resources:

Due to increase in energy demand, the need to generate clean and efficient way to produce energy is the most important problem the world is facing nowadays. Table 1 shows a comparison between two types of energy production techniques, Conventional and renewable energy technologies.

	Renewable Resources	**Conventional Resources**
Environment impact	Eco-friendly (zero carbon and green-house gas emissions)	Large amount of CO2 , CO and toxic gases emission
Resources	Sustainable resources	Limited resources

Cost	Only initial cost of installation of system	Varies depending upon the availability of resources
Maintenance	Less costly	Highly costly
Efficiency	Less Efficient	More Efficient [4]
Environment (origin of resources)	Not Detrimental to earth	Detrimental because extracting of these resources are done by mining and drilling
Reliability	Not Reliable , depends upon the weather etc	Reliable form of energy[5]

Table 1.1 Comparison between conventional and renewable energy resources

1.3 Solar Cell Technology:

Renewable energy technologies include solar, wind, biomass. These are new alternative energy resources for a sustainable and clean environment. Solar cell technology i.e. Photovoltaic technology is one of the most efficient technology[3] among the other renewable energy technologies because of the ample amount of solar radiation coming from sun.

Overall photo-voltaic solar cell requires two major functionalities[4].

1. It requires materials that have the capability to absorb light and excite an electron from lower energy state to higher energy state.
2. Movement of electron in the higher energy state, from solar cell to the external circuit.

1.3.1 Working of Solar Cell:

Solar cell work on the principle that when-ever light falls on the surface of the solar cell, an electron hole pair is generated which produces a current and voltage. Almost all devices that act a solar cell are in form of PN junction.

In solar cells, the absorption of photon takes place via sun-light which create an electron-hole pair. The energy of the incident photon must be greater than the band-gap of the semi-conductor material used. The generated electron hole pair is in a meta-stable state. It will either by collected to generate current or will recombine to generate no current.

The Quantum Efficiency of the solar cell is defined as the ratio of number of electrons collected by the solar cell to the number of incident photon on the solar cell. In case of no recombination i.e all the generated electrons are collected then the quantum efficiency is unity. The quantum efficiency is zero if energy of incident photon is less than bandgap of the material.

A typical silicon based solar cell consists of p-n junction where electron hole pair is generated, an anti-reflective coating for maximum absorption of sunlight, and front metal contacts for the collection of generated electrons.

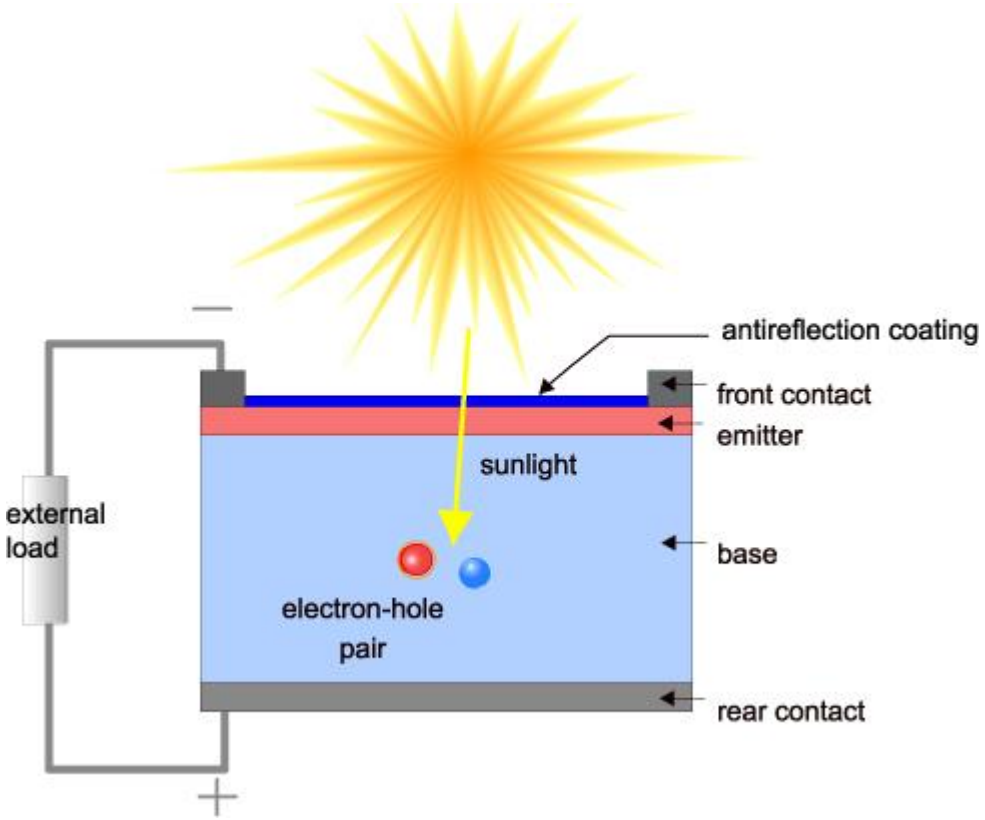

Figure 1.2 Working of a typical solar cell.

The generated electron from the incident of photon drifts towards the front metal contacts where it is collected by the external load. Factor involved in evaluation of a solar cell include open circuit voltage, peak power, fill factor and short circuit current density.

Short circuit current (I_{sc}) is generated when the electrodes of the solar cells are short circuited together. As the short circuit current depends on the area of the cell on which light is incident, it can be described as short circuit current density (J_{sc}). In an ideal case, where no recombination takes place and electron-hole pair generation is uniform, the J_{sc} is equal to the J_{ph}. In case of **open-circuit voltage**, no current flows through the external circuit. Voc is consider being the forward biased voltage, and depends directly on photo-generated current density. Now the fill-factor is considered as a ratio between the products of maximum power point current density and voltage with open circuit voltage and short circuit current density.

$$F.F = \frac{J_{mmp}.V_{mmp}}{J_{sc}.V_{oc}}$$

Where J_{mmp} is the maximum power point current density and V_{mmp} is the maximum power point open circuit voltage. Maximum power point is the point on J-V characteristic curve where solar cell gives the maximum power output.

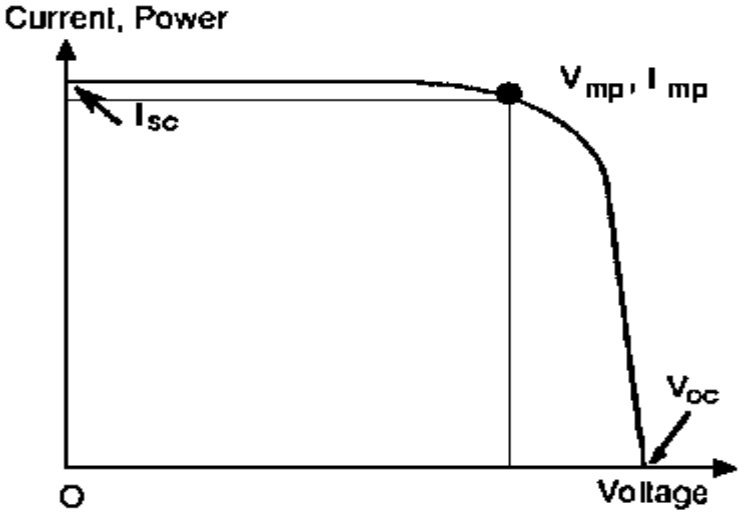

Figure 1.3 IV Characteristic curve of a typical solar cell.

Now the power conversion efficiency (PCE) of the solar cell can be calculated as the ratio between the maximum power generated (output) and the incident power (input). Solar cell efficiency measurements are usually done under AM 1.5 and temperature of 25°C.

$$Pmax = Voc.Isc.FF$$

$$\eta = \frac{P_{max}}{I_{in}} = \frac{V_{oc}.I_{sc}.FF}{I_{in}}$$

1.3.2 Generations of solar cells:

Photo-voltaic technology includes 3 generations.

1.3.2.1 First Generation Solar Cells:

First generation solar cells consist of silicon based solar cells that have achieved an excellent efficiency and are widely used for residential purpose. Silicon solar cells based on silicon wafer and hetro-junction silicon based solar cells have achieved a power conversion efficiency of 15% to 20%[5]. These types of solar cells consist of mono-crystalline silicon solar cell, poly-crystalline silicon solar cells and amorphous silicon solar cells.

Mono-crystalline solar cells are thin wafers of silicon sliced from a large single crystal of silicon. A number of such thin wafers are joined together to form a panel. Currently mono-crystalline solar cells have achieved an efficiency of 24.2%. These panels have high cost and making of single crystal of silicon for such cells are highly energy intensive. Moreover the efficiency of such cells decreases with increase in temperature.

Poly-crystalline silicon solar cells are made from multiple silicon crystals. Such type of crystal growth is not controlled like the one in mono-crystalline silicon solar cells. Because of crystal defects and grain-boundaries these types of solar cells have less efficiency. These cells are cheaper then mono-crystalline silicon based solar cells but have cell efficiency.

Amorphous silicon solar cells uses thin film of silicon deposited on a substrate, usually a glass or a metal. Multiple layers of silicon are also deposited to get absorbance in different spectrum. Due to highly flexible and thin structures, these type of solar cells are widely used for building integrated PV and can be used during travelling and on curved surfaces in solar thermal applications. But these cells cannot be used for industrial and domestic purposes, because these cells give a lower efficiency per unit area.

1.3.2.2 2nd Generation Solar Cells:

This generation of solar cell consist of thin-film solar cells, like hetro-junction solar cells, CIGS and CdTe based solar cells. These types of cells are made from thin layers of semi-conductor materials. Because of less cost and less material usage in these type of solar cells, these cells can be used instead of 1st generation silicon based solar cells. But mass production of this type of solar cells are difficult to achieve, moreover the techniques like vacuum processing and high temperature treatments of

thin films still require a large amount of energy consumption. These type of solar cells have achieved a power conversion efficiency of around 9%-18%.

1.3.2.3 3rd Generation Solar Cells:

To achieve higher efficiency at low cost, researchers have developed another generation of solar cells. This generation of solar cells mainly includes quantum dots solar cells, organic solar cells, dye-sensitized solar cells and pervoskite solar cells. These solar cells are low in cost of materials and manufacturing but have not achieved efficiency equal or greater than silicon based solar cells. Among this type of solar cells, DSSC have advantages over other solar cells of third generation because of semi-transparency for maximum light absorption.

1.4 Dye-Sensitized Solar cells:

Silicon solar cells are based on silicon wafer and hetro-junction silicon based solar cells have achieved a power conversion efficiency of 15% to 20%[5]. But due to their high manufacturing and material cost, O'Regan and Gratzel in 1991 developed a new low cost photo-voltaic solar cell known as Dye-sensitized solar cells[6]. Dye-sensitized solar cells (DSSC) are one of the most renowned types of third generation solar cells. Due to its tremendous properties like higher flexibility, low-cost fabrication, semi-transparency for more light absorption these type of solar cell are a key challenge for conventional silicon-based solar cells[7]. These solar cells have an efficiency reported as 7.1% to 7.9% depending on the materials used. The uniqueness of DSSC is that its electron generation, electron transport, light absorption and hole transport take place by different materials in the cell[8][9]. The power-conversion efficiency of these cells quickly climbed to 10% in the late 1990s and then gradually settled to 11.5%[10].

1.4.1 Advantages of DSSC:

1. Highly efficient for low density application like solar collectors mainly roof-top solar collectors.

2. No chances of recombination of electron hole pair un-like silicon based solar cells. In DSSC the generated electron by the dye moves to photo-anode and in no time an electron is supplied by the electrolyte to the dye[11].
3. This type of solar cell can work under low light conditions. DSSC can work under simple indoor room light[6].
4. DSSC use low cost materials and have fewer manufacturing cost. These type of solar cells are ecologically friendly solar cells.
5. The cells do not require any protection, hence they are mechanically robust.
6. These cells do not degrade in sun-light over time.
7. Unlike Silicon based solar cell, DSSC can operate in case of low internal temperature.
8. These solar cells are highly flexible, light weight and durable.

1.4.2 Limitations of DSSC:

1. Material purity is required. In case of less pure materials used in the cell, the lifetime of the cell will be affected.
2. The liquid electrolyte used in DSSC gives issues when it comes to temperature stability. At low temperature, the liquid electrolyte freeze leading to zero power production. At high temperature, the liquid electrolyte expands which affects the sealing of the cell.
3. The sealing of the cell must be done with great caution. The liquid electrolyte may evaporate because usually it is a volatile organic solution.
4. In outdoor condition, DSSC have stability issues with increase in temperature.

1.5 Nano-fibers:

Nano-fibers are one dimensional, continuous thread like nano-structures have a diameter in the range of 50nm to 500nm. Nano-fibers have gain attention in past few years owning to its superior properties like,

1. Large surface area to volume ratio.

2. High porosity

3. Small pore size

4. Low density

Nano-fibres can be sensitized using various methods including template-assisted synthesis[12], chemical vapor deposition (CVD)[13], self-assembly[14], wet chemical synthesis[15], and electro-spinning. Electro-spinning was developed in 1984 and is vastly used because of its high product-ability, simplicity and high yield. Furthermore Electro-spinning is divided into various methods like melt electro-spinning[16], co-axial Electro-spinning, Melt-electro-spinning[17] depending upon the solution and required morphology. It has various applications from field like medical to high-technology. It can be use for various Filtration Techniques and as an Anode in Solar Cells and Lithium Ion Batteries. In solar cells, metal oxide based nano-fibres are widely used because of their large surface area, high electrical conductivity, fast electron transport from dye to FTO, better dye loading and light-harvesting properties[18]

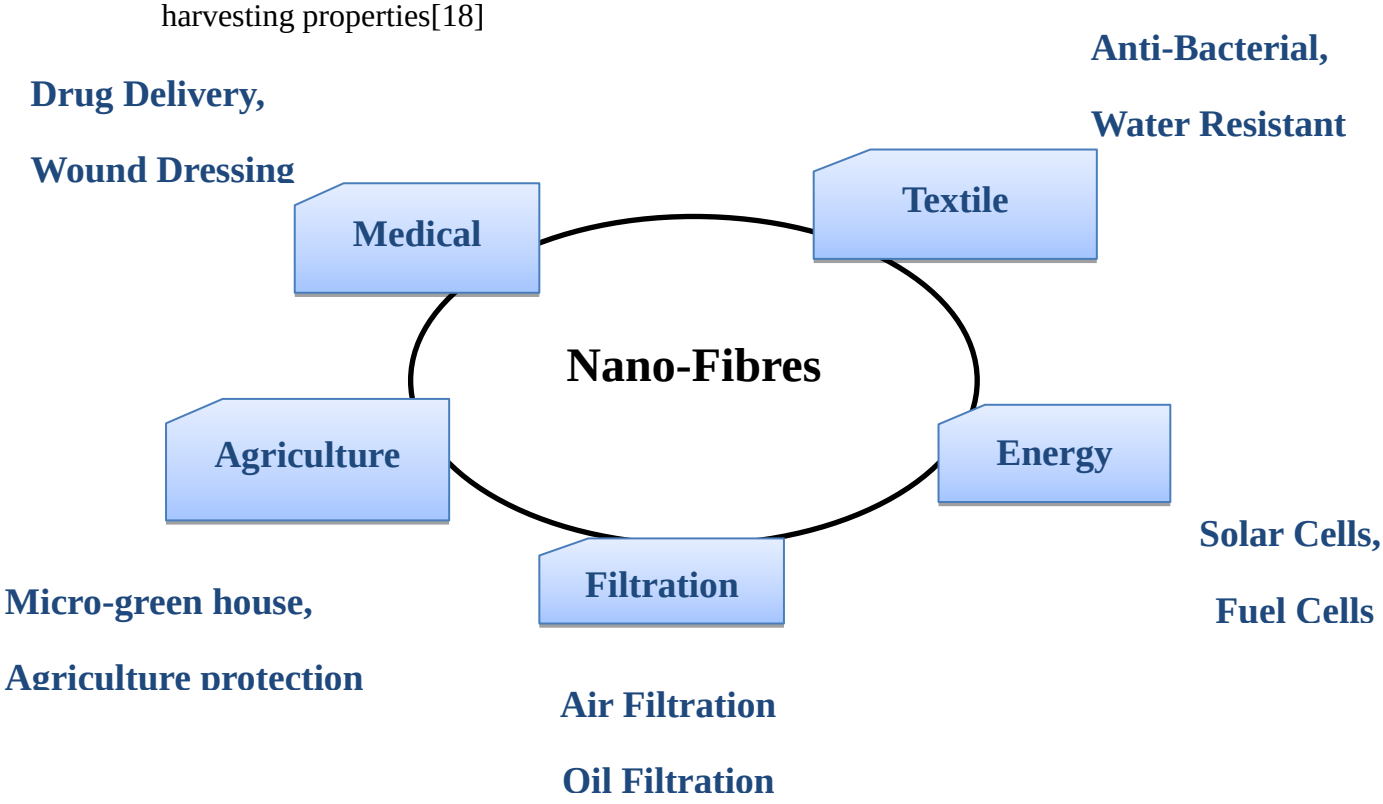

Figure 1.4 Application of Nano-fibres in various fields.

1.6 Amorphous Silicon Hetro-junction solar cell:

Due to low cost, stability, robustness and non-toxicity, thin-film solar cells are widely used in solar cell industries. At present, major materials used for thin film solar cells include a-Si/c-Si, CdS/CdTe and CdS/CuInGaSe.

a-Si-H/c-Si hetro-junction is a hybrid of both crystalline silicon and amorphous silicon with a phenomenal conversion efficiency[19]. In this type of solar cells a wider band-gap material such as a-Si-H is added to reduce the recombination of electron hole pair moreover higher capability of absorption in visible region. These hetro-junction solar cells have large area for better light absorption and give power conversion efficiency of 25-26%[20].

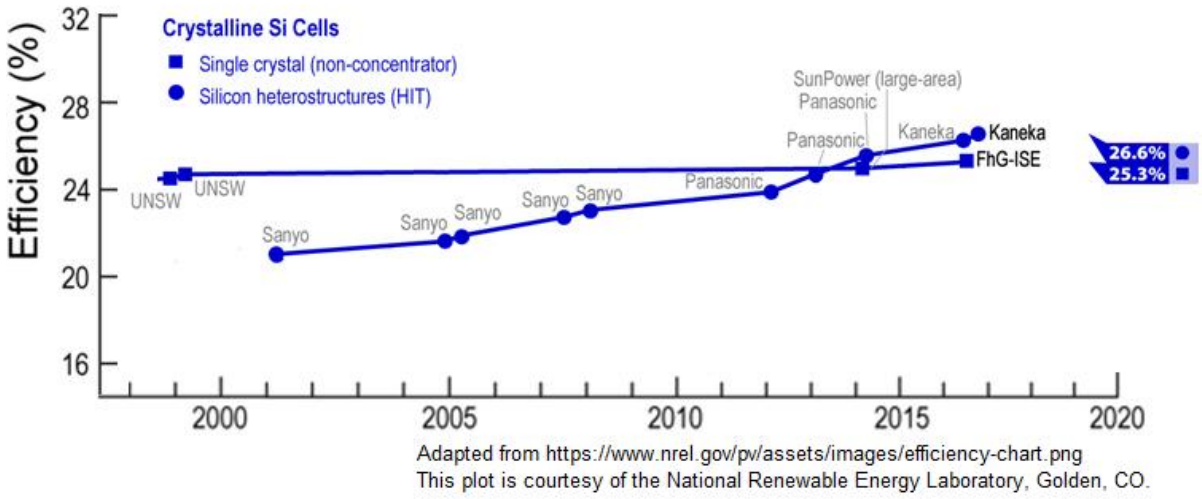

Figure 1.5 Comparison of Efficiency of Single crystal based solar cell and silicon hetro-structured based solar cells

1.6.1 Advantages of a-Si HJ solar cells:

1. Material used has wider and narrow band-gap which allow maximum light absorption.

2. Presence of 2 different types of light absorption layer i.e window layer and absorber layer make silicon hetro-junction solar cells more efficient for light absorption.
3. In case of dark current, the transport of generated electron-hole pair is carried out by the absorber layer.
4. Compared to 1st generation solar cells, these solar cells require comparatively easy low temperature production. Which means these solar cells saves energy and is economically friendly.

1.6.2 Limitations of a-Si HJ solar cells:

1. The uneven structure of amorphous silicon lead to high density states which creates dangling bonds[21]. This decreases the mobility and lifetime of free carriers as compared to crystalline materials.
2. Electron hole pair recombination can take place due to lattice mismatching between different layers of the hetro-junction solar cell.
3. Due to transversal current flow, voltage drop take place which leads to band gap discontinuity.
4. Contact resistance issue which decrease the fill factor of the solar cell, hence decreasing the overall efficiency of the cell.

1.7 Difference between a-Si:H hetro-junction solar cell and DSSC:

a-Si:H silicon based solar cells works like a pin diode. In an a-Si:H solar cell electron-hole pair is generation in the intrinsic region after which electron moves towards the n-region and hole moves towards the p-region. How-ever DSSC are not based on p-n junction solar cells, rather they work on the photo-generation of an electron by a dye, as in photosynthesis.

Summary:

This chapter gives an overview of energy crisis in the world. How conventional and renewable energy resources can benefit the energy crisis of the world. Renewable resources are an alternative form of energy because of its advantages like low cost, sustainable resource and eco-friendliness. Among renewable energy resources, solar cell technology is one of the most dominant technology. Solar cells use solar energy and convert it into electricity. There are 3 generation of solar of solar cells. 1st generation deals with silicon based solar cells, 2nd generation deals with thin film solar cells while 3rd generation deals with different nano-materials based solar cells. a-Si hetro-junction solar cells are among thin films solar cells having multi layer structure. These cells have achieved an efficiency of 24-25%. Similarly DSSC is among 3rd generation solar cells which provide electricity by using a dye. These cells are high cost effective and easy to fabricate. Certain types of nano-structures are used in DSSC like nano-particles, nano-fibres, nano-rods. Nano-fibres are widely used in DSSC because of its large surface area, high electrical conductivity, fast electron transport from dye to FTO, better dye loading and light-harvesting properties

References:

[1] H. A. Ribeiro, “Dye-Sensitized Solar Cells : an Overview,” 2011.

[2] B. Li, L. Wang, B. Kang, P. Wang, and Y. Qiu, “Review of recent progress in solid-state dye-sensitized solar cells,” *Sol. Energy Mater. Sol. Cells*, vol. 90, no. 5, pp. 549–573, 2006.

[3] J. Gong, J. Liang, and K. Sumathy, “Review on dye-sensitized solar cells (DSSCs): Fundamental concepts and novel materials,” *Renew. Sustain. Energy Rev.*, vol. 16, no. 8, pp. 5848–5860, 2012.

[4] A. Mohammad Bagher, “Types of Solar Cells and Application,” *Am. J. Opt. Photonics*, vol. 3, no. 5, p. 94, 2015.

[5] C. D. Grant, A. M. Schwartzberg, G. P. Smestad, J. Kowalik, L. M. Tolbert, and J. Z. Zhang, “Characterization of nanocrystalline and thin film TiO2solar cells with poly(3-undecyl-2,2’-bithiophene) as a sensitizer and hole conductor,” *J. Electroanal. Chem.*, vol. 522, no. 1, pp. 40–48, 2002.

[6] B. O’Regan and M. Gratzel, “A Low-Cost, High-Efficiency Solar-Cell Based on Dye-Sensitized Colloidal TiO_2 Films,” *Nature*, vol. 353, no. 6346, pp. 737–740, 1991.

[7] U. Mehmood, S. Rahman, K. Harrabi, I. A. Hussein, and B. V. S. Reddy, “Recent Advances in Dye Sensitized Solar Cells,” *Adv. Mater. Sci. Eng.*, vol. 2014, pp. 1–12, 2014.

[8] S. Gauthier *et al.*, “Mild cognitive impairment,” *Lancet*, vol. 367, no. 9518, pp. 1262–1270, 2006.

[9] A. Hagfeldt and M. Grätzel, “Molecular photovoltaics,” *Acc. Chem. Res.*, vol. 33, no. 5, pp. 269–277, 2000.

[10] M. K. Nazeeruddin *et al.*, “Combined experimental and DFT-TDDFT computational study of photoelectrochemical cell ruthenium sensitizers,” *J. Am. Chem. Soc.*, vol. 127, no. 48, pp. 16835–16847, 2005.

[11] M. Law, L. E. Greene, J. C. Johnson, R. Saykally, and P. Yang, “Nanowire dye-sensitized solar cells,” *Nat. Mater.*, vol. 4, no. 6, pp. 455–459, 2005.

[12] Y. Liu, J. Goebl, and Y. Yin, “Templated synthesis of nanostructured materials,” *Chem. Soc. Rev.*, vol. 42, no. 7, pp. 2610–2653, 2013.

[13] M. Chi, Y. Zhao, Q. Fan, and W. Han, “The synthesis of PrB6 nanowires and

nanotubes by the self-catalyzed method," *Ceram. Int.*, vol. 40, no. 6, pp. 8921–8924, 2014.

[14] N. I. Kovtyukhova, B. R. Martin, J. K. N. Mbindyo, T. E. Mallouk, M. Cabassi, and T. S. Mayer, "Layer-by-layer self-assembly strategy for template synthesis of nanoscale devices," *Mater. Sci. Eng. C*, vol. 19, no. 1–2, pp. 255–262, 2002.

[15] H. Zhu, X. Gao, Y. Lan, D. Song, Y. Xi, and J. Zhao, "Hydrogen titanate nanofibers covered with anatase nanocrystals: A delicate structure achieved by the wet chemistry reaction of the titanate nanofibers," *J. Am. Chem. Soc.*, vol. 126, no. 27, pp. 8380–8381, 2004.

[16] L. Larrondo and R. S. J. Manley, "Electrostatic fiber spinning from polymer melts. II. Examination of the flow field in an electrically driven jet," *... Polym. Sci. Polym. ...*, vol. 19, pp. 921–932, 1981.

[17] J.-H. He, Y. Liu, L.-F. Mo, Y.-Q. Wan, and L. Xu, "Electrospun nanofibres and their applications," *iSmithers, Shawbury, Shrewsbury, Shropshire, UK*, p. 260, 2008.

[18] P. F. . b Du, L. X. . Song, and J. . Xiong, "Enhanced conversion efficiency in Dye-sensitized solar cells based on bilayered nano-composite photoanode film consisting of TiO2 nanoparticles and nanofibers," *J. Nanosci. Nanotechnol.*, vol. 14, no. 6, pp. 4164–4169, 2014.

[19] K. Yoshikawa *et al.*, "Silicon heterojunction solar cell with interdigitated back contacts for a photoconversion efficiency over 26%," *Nat. Energy*, vol. 2, no. 5, 2017.

[20] M. Taguchi *et al.*, "24.7% Record efficiency HIT solar cell on thin silicon wafer," *IEEE J. Photovoltaics*, vol. 4, no. 1, pp. 96–99, 2014.

[21] A. S. Alloys and F. O. R. S. Cells, "AMORPHOUS SILICON ALLOYS," vol. 7, 1985.

CHAPTER 2:

LITERATURE REVIEW

2.1 Working of DSSC:

At first the dye absorbs light and produces an electron hole pair. The electron produced in dye become excited from its ground state to the excited state. The dye molecules have an energy band gap higher than that of the semi-conductor material next to it. The electron moves to the conduction band of the semiconductor keeping the dye in its oxidizing state. At electrolyte, the redox reaction takes place that reduces the dye back to its neutral state[1]. The semi-conductor then transfers the electron to the counter electrode or cathode[2]. The cathode moves the electron to the electrolyte. At electrode the reduction reaction takes place and electrolyte restores its initial state by accepting electrons from the external circuit[3].

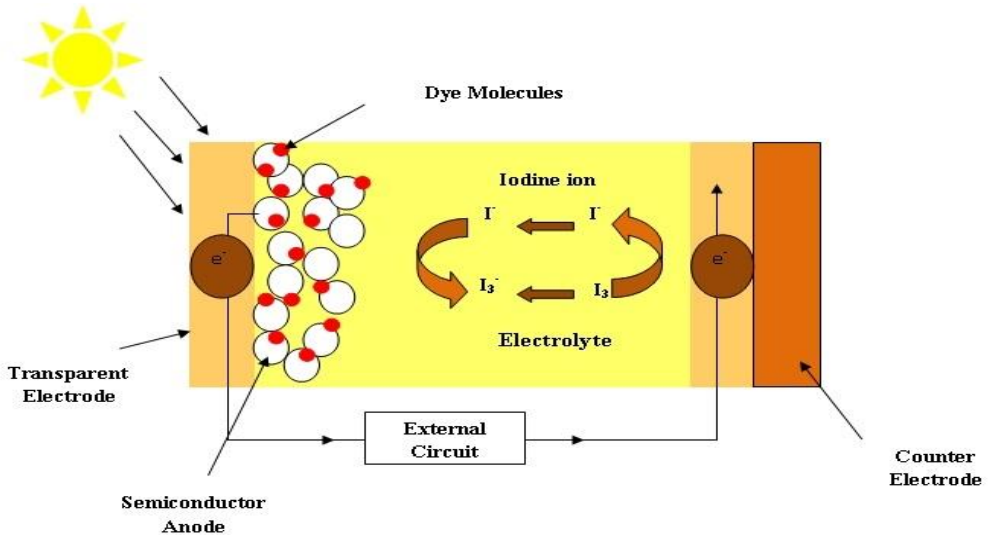

Figure 2.1 Working of a Dye Sensitized Solar Cell

2.1.1 Components for DSSC:

DSSC consists of following components,

2.1.1.1 Photo-anode: It consists of a transparent conductive substrate on which a semi-conductor film is deposited. Both the conductive substrate and semi-conductor deposited onto the substrate are known as photo-anode. The anode must be transparent to allow maximum light to reach the active area of the cell i.e. Dye. The semiconductor should have a large surface area to volume ratio, to give large area for dye absorption and electron transport to external circuit[4]. The conductivity of the semi-conductor film must be high so that there are less energy losses and more charge transfer to the external circuit[5]. Conductive substrate includes ITO and FTO. A comparison of conductive substrate was done by Sima et al, in which they propose that after annealing, the sheet resistance of FTO remains constant but the sheet resistance for ITO increases[6].

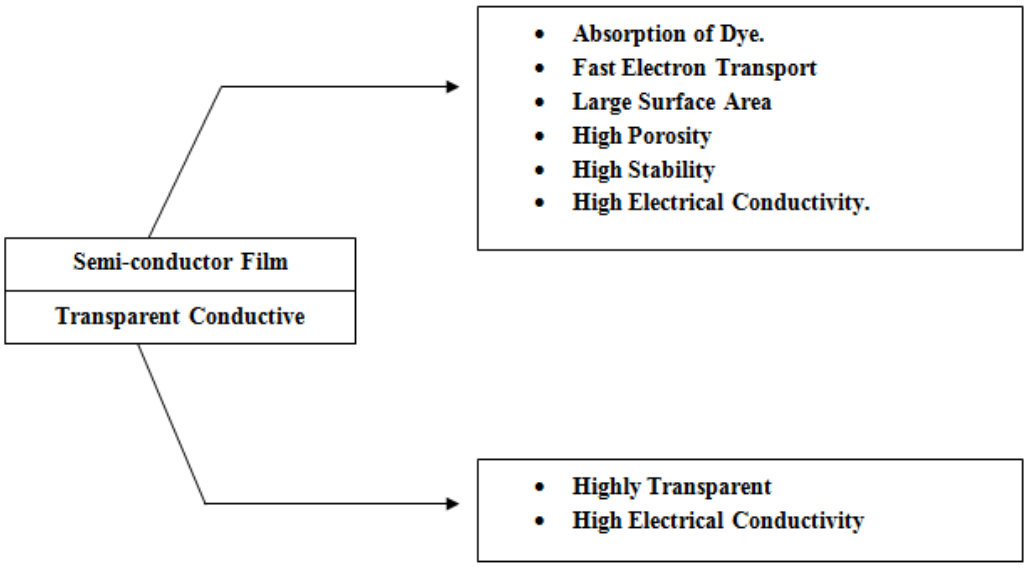

Figure 2.2 Properties of a semi-conductor film and transparent conductive oxide in a typical DSSC.

Multiple metal oxides based nano structures including nano-particles, nano-spheres, nano-rods and nano-fibres are used for the semi-conductor anode in DSSC. Metal oxides include TiO_2, SnO_2, ZnO, Nb_2O_3 and composite based metal oxides. Currently nano-fibres based photo-anodes are getting much attention because of the large surface area to volume ratio, fast electron transport from dye to FTO, better dye loading and light-harvesting properties[7]. By using I-D nanostructures for photo-anode, the issue of recombination between photo-anode/dye/electrolyte interfaces can be controlled.

2.1.1.2 Dye: The function of a photo-sensitizer (Dye) is to absorb light, generate an electron-hole pair and transfer that electron to the conduction band of the semi-conductor anode next to it. Dye sensitizer based on transition metals has given the best efficiency till now[8]. There are multiple metal based dyes, metal free dyes and natural dyes that are being used in DSSC. The dye should have following properties for a better efficiency of a DSSC,

- The band-gap of dye must be higher than that of the semi-conductor anode next to it. Or in other words, the LUMO of the dye must be more negative then the conduction band of the semi-conductor.
- Show absorption in visible region
- Load/absorb properly on to the semi-conductor surface.
- Must possess the ability to remain stable in its oxidized form. In its oxidized form, the electrolyte donates an electron to dye molecules.
- Molecular structure of the Dye.
- The HOMO of the Dye must be more positive then the redox potential of the Electrolyte.

In case of metal complex sensitizer, the ligand plays the role of defining the properties of the dye. Properties like adhesion with the semiconductor, charge transfer properties are defined by the ligand. Considering the properties required for a dye, Ruthenium(II) polypyridyl give the best power conversion efficiency[9]. This Ruthenium based dye i.e N-719 gives photo-stability[10], excitation properties like good life time and more-over easy redox reaction from

electrolyte. This dye consists of two photons which gives better absorption of light and electron transfer to the semi-conductor.

Metal-free dyes are also used in DSSC. The efficiency of these dyes depends on proper selection of the substituent with the acceptor and donor molecules and proper tuning of the complex that is being used. These dyes give different efficiencies in liquid, ionic and solid states of electrolyte[11]. This type of dye does not give sufficient efficiency to be used on industrial scale.

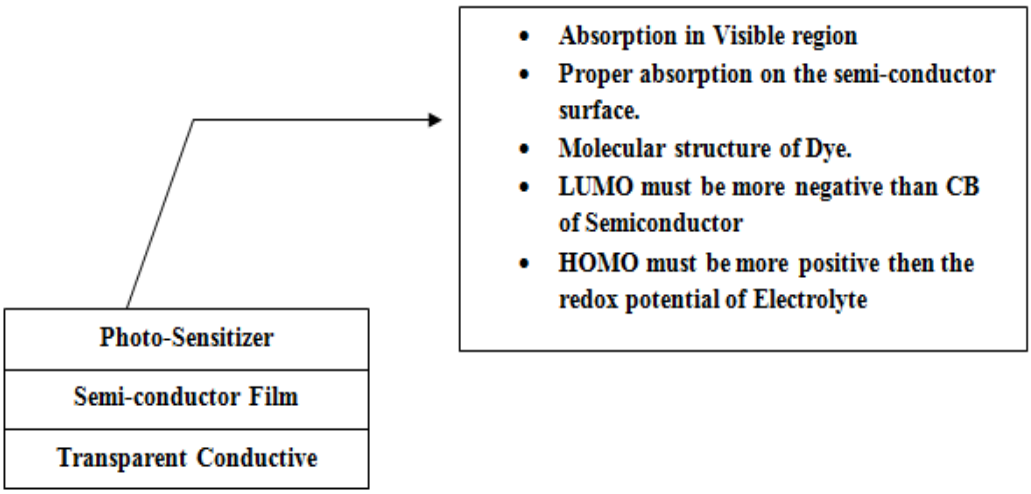

Figure 2.3 Properties of Dye in a typical DSSC.

Natural dyes are widely used because of their low cost, easy availability, less toxic properties and environmental friendliness. The absorption range of the natural dye depends on the fruit extract used and solvent[12]. But due to weak interaction between natural dye molecules and semi-conductor, the efficiency of the cell is low. Dye aggregation on the semi-conductor nano-structure also decreases the efficiency of the cell.

Carbon based materials like graphene is also use as a dye because of the high conductivity of graphene based materials. Yan.et al (2010) have use graphene quantum dots because of its tunable band-gap. This tunable band-gap effect is seen because of the quantum confinement effect. He also added 1, 3, 5 tri-alkyl phenyl as a substituent to reduce the effect of aggregation of quantum dots. With TiO2 as

photo-anode, graphene quantum dots have achieved a fill factor of only 0.58. As a Sensitizer, graphene has not achieved much efficiency. It can be use as a co-sensitizer. Zhu et al (2015) report the use of graphene quantum dots along-side N-719 dye molecules. The efficiency of the cell increases from 7.28% to 7.95%. Other graphene and carbon based materials have not been reported in literature for use as sensitizer or as a co-sensitizer.

2.1.1.3 Electrolyte: The main function of electrolyte is to regenerate the dye after the production of electron-hole pair in dye molecules. Moreover it also transfer positive charges, or generated holes towards the counter electrode. Electrode is an important component of DSSC because it provides stability to the DSSC. The efficiency of a typical DSSC depends upon the Donor number of the solvent used as an electrolyte. Increase in the donor number of the solvent increases the V_{oc} and decreases the J_{sc}[13].

A highly efficient electrolyte for DSSC must have,

1. Electrolyte must not absorb light in visible region.
2. Electrolyte must not cause the degradation of dye and desorption of dye.
3. It must have higher conductivity.
4. It must have low viscosity for faster diffusion of electron.
5. Good interfacial contact with semi-conductor and counter electrode.

There are multiple types of electrolytes that are being currently used for increasing the efficiency of DSSC. These types of electrolyte include liquid electrolyte, solid-state electrolyte, and quasi-state electrolyte.

Liquid Electrolyte consists of organic and ionic electrolytes depending upon the solvent used. In case of organic electrolytes, the major component is redox couple. There are various type of organic electrolytes that are used including Br^{-}/Br_3[14], $SCN^{-}/(SCN)_2$ but I_3^{-}/I^{-} is considered an excellent redox couple. I_3^{-}/I^{-} exhibits all the properties that are essentially required for an efficient electrolyte. Moreover I_3^{-}/I^{-} gives slow recombination between generated electrons and I_3[15]. Ionic Electrolyte at room temperature encounters issues like evaporation rate and leakage. N, N' bis-alkyl-substituted imidazoliumiodides[16] is considered to be an efficient ionic

electrolyte in DSSC. But considering their high viscosity these electrolytes gives low efficiencies in DSSC.

Solid-state Electrolytes are developed to reduce the leakage effects in DSSC[17]. These types of electrolytes consist of a p-type semi-conductor with a band-gap structure that is well-matched with the HOMO level of the dye/photo-sensitizer[5]. Materials like CuI, CuBr have shown better hole transport and good conductivity. But these type of electrolyte show poor contact between semi-conductor material and electrolyte. The electrolyte does not penetrate properly in the pores of the semi-conductor material. Moreover, there are high chances of charge recombination between the semi-conductor electrode and electrolyte.

Quasi-state Electrolytes are mixture of polymer and liquid electrolyte[18]. This type of electrolyte is in gel state, which solve the issue of leakage of electrolyte and weak contact between semi-conductor material and electrolyte as in case of solid-state electrolyte. These types of electrolytes give long-term stability and better interfacial contacts[19]. The efficiency of this type of electrolyte depends on the morphology and molecular weight of the polymer used. Moreover the temperature of the DSSC is an important parameter in quasi-state electrolyte because increase in temperature changes the phase from gel like to solution (Liquid)[20]

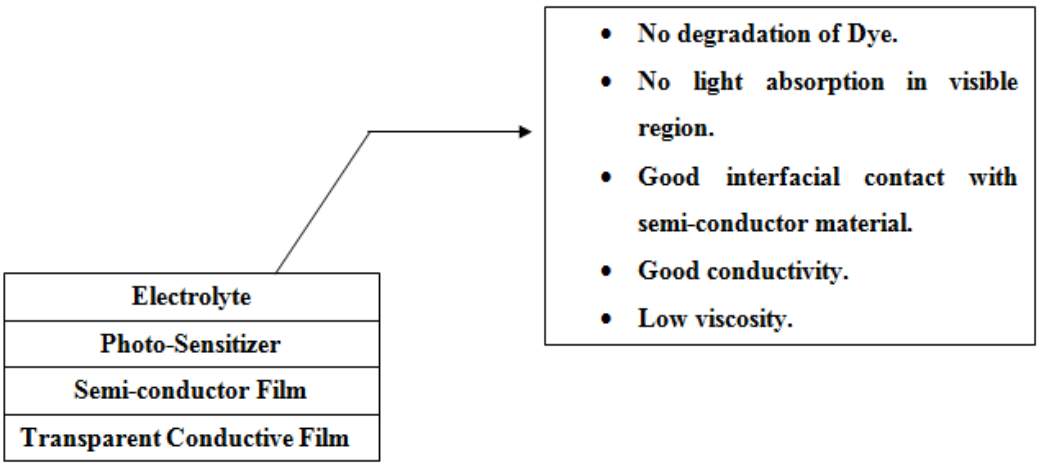

Figure 2.4 Properties of Electrolyte in a typical DSSC.

2.1.1.4 Counter Electrode: The main function of a counter electrode is,

1. To act as a catalyst and perform reduction of the electrolyte and re-generation of dye sensitizer for electron injection
2. For hole collection from the hole-transport material in solid state DSSC.

An efficient counter electrode must have high conductivity and high photo-catalytic properties for reduction of the redox couple. In case of uncoated conductive substrate like FTO and ITO, the reduction reaction is extremely slow[15]. To get an efficient counter electrode, the conductive substrate must be coated with a catalytic material to speed up the reaction.

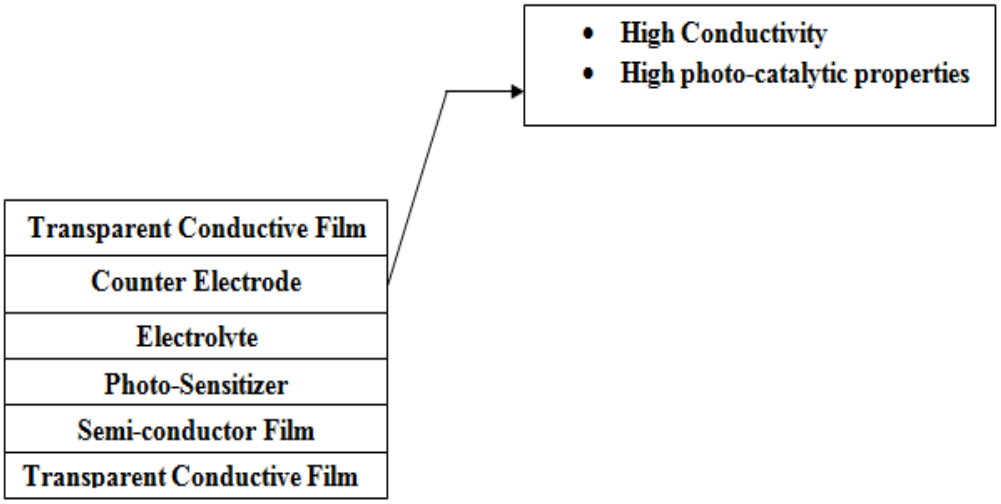

Figure 2.5 Properties of Counter Electrode of a typical DSSC

There are multiple types of materials that are used as counter electrode materials including platinum counter electrodes, Carbon materials based counter electrodes, polymer based materials, transition metal oxide based materials, hybrid counter electrode materials. Platinum based counter electrode materials have achieved a PCE of 12% in DSSC[21]. Multiple materials used for counter electrode and their PCE is shown in the table.

Counter Electrode Material	PCE	Reference

$Pt_{0.02}Co$	10.23	[22]
PtCuNi	9.66	[23]
MWCNT's (CVD)	8.80	[24]
Carbon black	7.60	[25]
PEDOT	7.93	[26]
PANI-SDS	7.40	[27]
Carbon/Fe3O4	8.37	[28]

Table 2.1 PCE of some commonly used counter electrode materials

2.1.2 Metal Oxide based Photo-anodes in DSSC:

Several metal-oxides are used as photo-anode to enhance the efficiency of DSSC. These Metal oxides like TiO_2, SnO_2, ZnO and Nb_2O_3 are use in different nano-structures for use as photo-anode in advance generation solar cells. TiO_2 nano-structures are widely used as working anode of DSSC because of its wider band-gap, stability, cost-effectiveness and environmental friendly characteristics[29]. These TiO_2 nano-structures include nano-particles, nano-rods, nano-wires and nano-fibres.

Structure	Dye	Efficiency	Reference
TiO_2 nano-fibres	N719	4.4%	[30]
TiO_2 nano-fibres	bryophyte	0.0036%	[31]

TiO_2 multi-scale porous nano-fibres	N719	6-8.5%	[32]
Bi-layer TiO_2 nano-fibres	N719	8.40%	[33]
Mesoporous TiO_2 nano-fibres	N719	8.14%	[34]
TiO_2 nanofibres on TiO_2 nano-particles	N719	8.14%	[35]

Table 2.2 PCE of TiO_2 nano-fibre based materials with different dyes.

In solar cells, metal oxide based nano-fibres are widely used because of its large surface area and high porosity for better dye absorption. Photo-anode should have high porosity, better stability, high electrical conductivity, Large surface area to volume ratio and better dye absorption. Currently nano-fibres based photo-anodes are getting much attention because of their high electrical conductivity, large surface area to volume ratio, fast electron transport from dye to FTO, better dye loading and light-harvesting properties[7]. TiO_2 nano-structures are widely used as working anode of DSSC because of its wider band-gap, stability, cost-effectiveness and environmental friendly characteristics[36], but because of its large band-gap, absorption in UV region and recombination of electrons it does not provide the required efficiency. TiO_2 can be use with metal oxide structures like SnO_2, ZnO and Nb_2O_3 as composite to reduce the recombination rate. SnO_2 is an n-type wide band gap metal oxide semiconductor having application in the field of gas sensors[37] and optoelectronic devices[38]. But it gave issues like poor absorption with dye molecules and recombination. Coupling TiO_2 nano-fibres with other materials will enhance its photo-catalytic activities[39]. This is because of the enhancement of charge separation. Various semi-conductor to semi-conductor based hetro-structures of TiO_2 are used including TiO_2/SnO_2[40], TiO_2/ZnO[41]. TiO_2/SnO_2 based hetro-

strucutres have advantages over other because of the low cost of SnO_2 and some precise crystallographic planes of nano-crystals of TiO_2 and SnO_2 [42]. Recombination in these hetro-structures is reduced because the valence band of TiO_2 is less positive then SnO_2 valance band. One the other hand, the conduction band of TiO_2 is more negative than SnO_2 [43]. When UV light falls on this structure, the photon of energy higher than or equal to the band gaps of TiO_2 and SnO_2, the photo-generated electrons in the irradiated TiO_2 can move to the CB of SnO_2 and the photo-generated holes in the irradiated SnO_2 move to the VB of TiO_2 as shown in figure. As a result, TiO_2 /SnO_2 hetero-structures could hinder the charge recombination and improve the required efficiency. Moreover, Band-gap can also be adjusted by using hetro-strucutres.

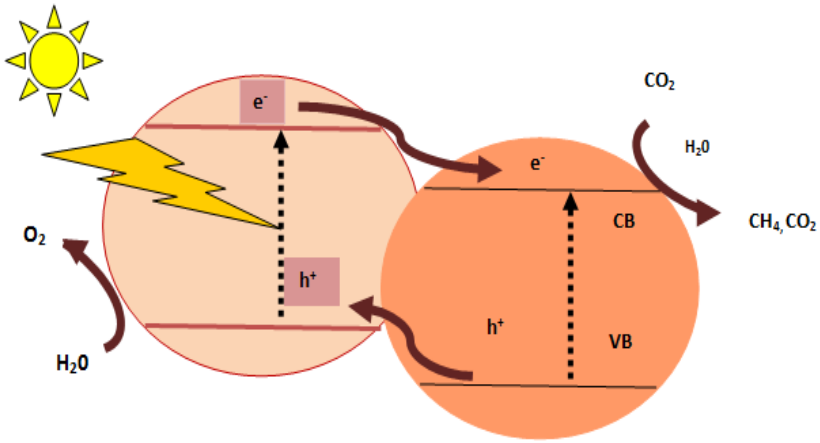

Figure 2.6 Schematic illustration of a semiconductor heterostructure

	TiO_2	**SnO_2**	**TiO_2/SnO_2 Composite**
	High Stability.	Fast Electron diffusion rate.	Better Performance Under all Regions.

Advantages	Wide Band-gap.	Wide Band-gap. Higher Light reflective index.	Improve Charge Separation. Improve Photo-catalyst Properties
Dis-Advantages	Fast photo-generated electron hole pair recombination. Work only in UV Region	Poor Photovoltaic Performance Fast Interfacial Electron Recombination. Insufficient Attachment of Dye Molecule.	Difficult to control their synthesis.

Table 2.3 Advantages and Disadvantages of TiO_2, SnO_2 and TiO_2/SnO_2 composite material.

Electrical conductivity of the film will increase if recombination of electron decrease and its mobility and carrier concentration increases i.e more light will be absorbed and more electrons will move away from the photo-anode.

Objective of this research work includes,

- Formation of TiO_2 and SnO_2 Nano-fibers by varying polymer concentration during Electro-spinning.

- In cogitate with producing high efficiency DSSC, to prepare and study the properties of TiO_2/SnO_2 Composite Nano-fiber and Graphene Sensitized TiO_2/SnO_2 Composite Nano-fiber as Photo-anode.
- To Make DSSC more cost Effective by Graphene Sensitization.

2.2 a-Si:H hetro-junction solar cells:

Hetro-junction solar cells consist of a stack of various layers of thin-film silicon in crystalline and amorphous forms.

2.2.1 Working of Silicon Hetro-junction solar cells:

Silicon Hetro-junction solar cells works as a PIN diode. PIN refers to a semi-conductor device having a structure of p^+-intrinsic-n^+. In Silicon Hetro-junction solar cells the intrinsic layer is of i-Si which has a very small doping with respect to the p+ a-Si and n+ a-Si layers. When such a structure is formed, the holes diffuse from the p+ side and the electrons diffuses from the n+ layer recombine and disappear leaving behind a separation layer of i-Si between both the layers. When a reverse biased is applied to such a system and a photon of light higher than the band-gap of i-Si is incident on the cell , the photo-generation of electron hole pair take place. Due to reverse biasing the electron moves towards the n+ region (electron collecting stack) and the hole moves towards the p+ region (hole collecting stack). A typical silicon hetro-junction solar cell has following parts.

1. **Metal contacts:** The metal contacts on the surface of the cell and at the bottom of the cell refer to the collection of electron and movement of electrons to the external circuit.

2. **Transparent conductive oxide:** TCO enhance the photo-generation of electron-hole pair and transport the produced electrons to the metal contacts. High absorption to ensure maximum photon of light to enter the cell. Large band-gap materials like indium, zinc and tin can be use as TCO. Indium tin oxide is use for TCO because of its high conductivity, mobility and carrier concentration. TCO layer on top of the cell is use as an anti-reflective coating.

However the TCO at the back of the cell refers to optimized layer with the metal contact to form a infrared reflector.

3. **Passivation layer:** Passivation layer in silicon hetro-junction solar cells are use to ensure that there are no active defects on the surface of wafer. The surface defects are involved in the recombination of electrons resulting in decrease of cell efficiency. a-Si:H is use as a passivation layer because of its properties like large carrier lifetime in silicon wafers and higher efficiency.

4. **Absorption layer:** This is the layer were photons of light are absorbed and electron hole pairs are generated. In typical silicon hetro-junction solar cells, this layer refers to the middle intrinsic crystalline silicon layer.

5. **Semi-permeable layer:** This layer allow passing of only one type of charges, either holes or electrons. There are two type of semi-permeable layers in a hetro-junction solar cell.
    - Hole Collecting Stack: Hole collecting stack (usually at the upper side of the cell) is use to collect holes. This layer is highly p+ doped a-Si:H. As the cell is reversed biased, photo-generated holes move towards the p+ a-Si:H.
    - Electron collecting stack: Electron collecting stack (usually at the lower side of the cell) is use to collect electrons. This layer is highly n+ doped a-Si:H. As the cell is reversed biased, photo-generated holes move towards the n+ a-Si:H.

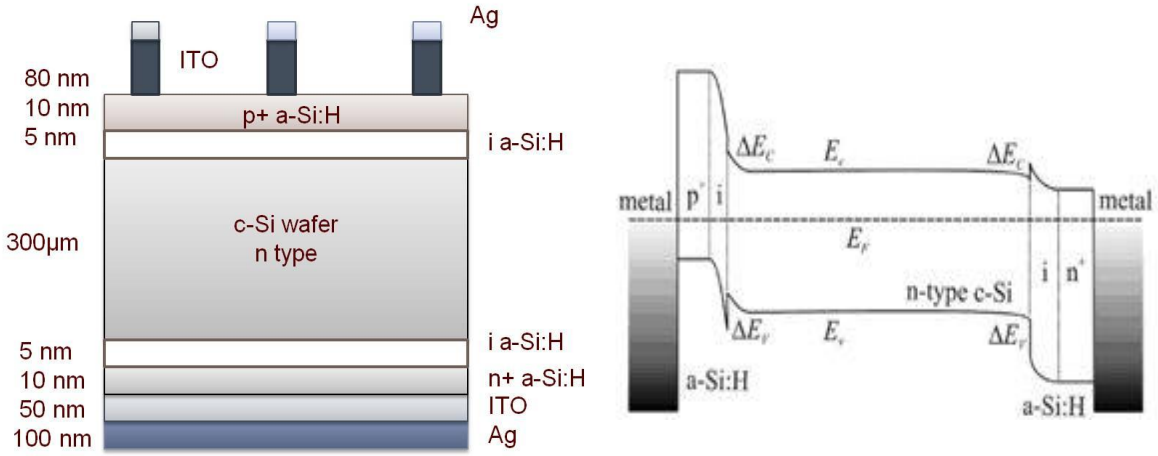

Figure 2.7 (a) Basic Structure of a-Si:H HJ Solar cell (b) band-gap description of a-Si:H HJ solar cell

2.2.2 Contact Resistance of Si-Hetro-junction solar cells:

Contact resistance in a solar cell is refer to the energy losses at the junction between metal contacts and semi-conductor beneath it. This effect can be minimize by using a highly doped semi-conductor material in silicon solar cells. By using a highly doped material, a dead layer maybe created between the interface of the metal contact and semi-conductor which lead to a high voltage drop across the device[44]. To measure the contact resistance of the cell Transmission line measurement (TLM) is use.

2.2.3 Transfer length measurement for a-Si hetro-junction solar cell:

Thin film solar cells offer high contact resistance at the semi-conductor and metal junction. This contact resistance results in low efficiency of the cell. Transfer length measurement is used to determine the contact resistance between two metal contacts. A series of metal contacts are made as shown in figure with various spacing between the metal contacts. When probes (voltage) is applied between two contacts, followed resistances are offered (measured using ammeter)

1. Metal-semi-conductor contact resistance of the first contact.
2. Sheet resistance of the semi-conductor in-between the contacts.
3. Metal-semi-conductor contact resistance of the second contact.

This resistance measured is a linear combination of all these resistances. If numerous measurements are made between various metal contacts that are split by different distances, a plot of resistance versus contact separation can be attained.

If the separation between the contacts is uttered in terms of the ratio L/W - where L is the length and W is the width of the area in-between the contacts , a linear plot is observed , where the slope of the line is the sheet resistance in-between the metal contacts. The intercept of the line with the y-axis, is two times the contact resistance. This depicts that the sheet resistance as well as the contact resistance can be determined from this technique.

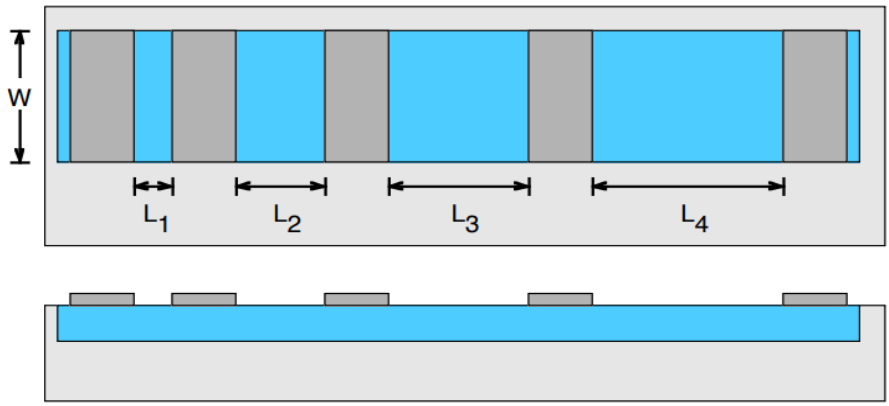

Figure 2.8 TLM patterns with various spacing between metal contacts

In this research we investigate the effect of various parameters on the contact resistance of the cells. The parameters are,

- Systematic analysis to determine the important interactions between the different layers in the hole-collecting contact.
- Performance of the stack when its constituent layers are varied.
- How the thickness of a-Si:H , ITO annealing temperature and time contribute to the overall series resistance of the cell.

2.2.4 Anti-reflective coating in hetro-junction solar cells:

An anti-reflective coating is a thin layer added between the metal contact and doped semi-conductor material that increase the light absorption. In a-Si:H hetro-junction solar cell the lateral conductivity is very low. So a TCO (transparent conductive oxide) is use as an anti-reflective coating. This layer should have following properties,

1. Enhance the photo-generation of electron-hole pair and transport the produced electrons to the metal contacts.
2. Must have high absorption to ensure maximum photon of light to enter the cell.

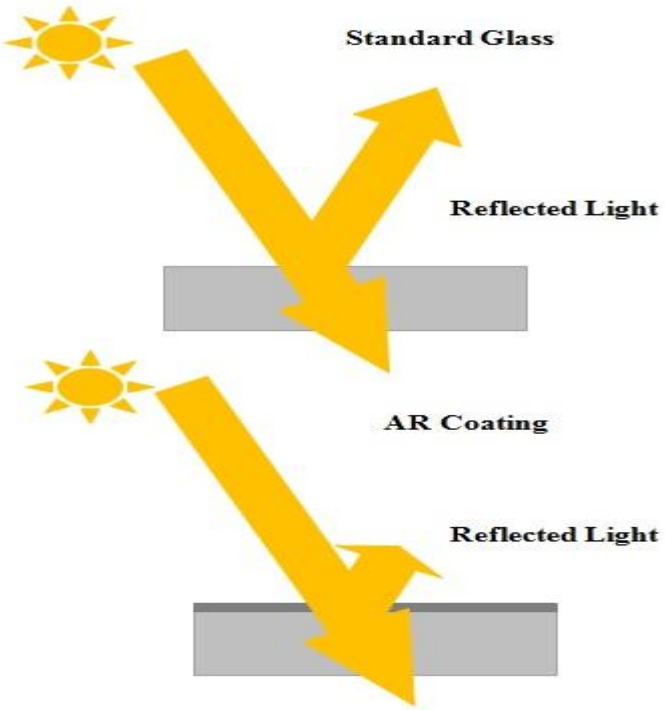

Figure 2.9 Systematic description of a cell with and without anti-reflective coating

For a-Si:H hetro-junction solar cell, large band-gap materials like indium, zinc and tin[45] can be use as TCO. Currently Indium tin oxide is use for TCO because of its high conducitivity, mobility and carrier concentration. Like ITO, Indium Oxide is a transparent conductor that passes over 90% of visible light and gives very low electrical resistivity[46]. These properties have led to a wide range of applications

both in coating glass for energy-efficient windows and as transparent elements in optoelectronic devices such as solar cells. Indium oxide is a wide bandgap transparent semi-conductor with a bandgap of 3.6eV. In_2O_3 in the bulk form has been extensively used in solar cells and organic light emitting diodes[47].

In this research, electrical properties of IO are studied. The objectives behind this work is,

- Sputter deposition of Indium Oxide on a-Si:H layer.
- To Study the Electrical properties of prepared films when the thickness and sputtering gas concentration is varied.

Summary:

This Chapter summarize the working principle, components and materials used for DSSC and a-Si:H solar cells. DSSC works when a dye molecule produces electron hole pair which is transfer to the external circuit and the hole pair generated in dye is filled by electrolyte. A redox reaction takes places at electrolyte and the deficiency of the dye is filled. Several nano-materials have been used as anode, dye, electrolyte and counter electrode in DSSC. Some metal-oxide based materials are also discussed as photo-anodes materials. Similarly a-Si:H hetro-junction solar cells consist of stack of thin films including passivation layer, TCO, n/p type a-Si. Each layer constitutes to a different function. The contact resistance on the surface of such cells are studied by creating transfer length measurement (TLM) patterns. Similarly importance of TCO layer is also discussed. Moreover the objective of the research is also discussed in this chapter.

Reference:

[1] H. H. Kim, C. Park, W. Choi, S. Cho, B. Moon, and D. I. Son, "Dye-sensitized Solar Cells," vol. 65, no. 9, pp. 1315–1319, 2014.

[2] S. Ardo and G. J. Meyer, "Photodriven heterogeneous charge transfer with transition-metal compounds anchored to TiO_2 semiconductor surfaces," *Chem. Soc. Rev.*, vol. 38, no. 1, pp. 115–164, 2009.

[3] U. Mehmood, S. Rahman, K. Harrabi, I. A. Hussein, and B. V. S. Reddy, "Recent Advances in Dye Sensitized Solar Cells," *Adv. Mater. Sci. Eng.*, vol. 2014, pp. 1–12, 2014.

[4] M. R. Hoffmann, S. T. Martin, W. Choi, and D. W. Bahnemann, "Environmental Applications of Semiconductor Photocatalysis," *Chem. Rev.*, vol. 95, no. 1, pp. 69–96, 1995.

[5] J. Gong, J. Liang, and K. Sumathy, "Review on dye-sensitized solar cells (DSSCs): Fundamental concepts and novel materials," *Renew. Sustain. Energy Rev.*, vol. 16, no. 8, pp. 5848–5860, 2012.

[6] C. Sima, C. Grigoriu, and S. Antohe, "Comparison of the dye-sensitized solar cells performances based on transparent conductive ITO and FTO," *Thin Solid Films*, vol. 519, no. 2, pp. 595–597, 2010.

[7] P. F. . b Du, L. X. . Song, and J. . Xiong, "Enhanced conversion efficiency in Dye-sensitized solar cells based on bilayered nano-composite photoanode film consisting of TiO2 nanoparticles and nanofibers," *J. Nanosci. Nanotechnol.*, vol. 14, no. 6, pp. 4164–4169, 2014.

[8] K. Kalyanasundaram and M. Grätzel, "Efficient Dye-Sensitized Solar Cells for Direct Conversion of Sunlight to Electricity," *Mater. Matters*, pp. 1–6, 2009.

[9] A. S. Polo, M. K. Itokazu, and N. Y. Murakami Iha, "Metal complex sensitizers in dye-sensitized solar cells," *Coord. Chem. Rev.*, vol. 248, no. 13–14, pp. 1343–1361, 2004.

[10] Y. Takahashi *et al.*, "Highly efficient polypyridyl-ruthenium(II) photosensitizers with chelating oxygen donor ligands: β-diketonato-bis(dicarboxybipyridine)ruthenium," *Inorganica Chim. Acta*, vol. 310, no. 2, pp. 169–174, 2000.

[11] A. Mishra, M. K. R. Fischer, and P. Bäuerle, "Metal-Free Organic Dyes for Dye-Sensitized Solar Cells: From Structure: Property Relationships to Design Rules," *Angew. Chemie Int. Ed.*, vol. 48, no. 14, pp. 2474–2499, 2009.

[12] M. R. Narayan, "Review: Dye sensitized solar cells based on natural photosensitizers," *Renew. Sustain. Energy Rev.*, vol. 16, no. 1, pp. 208–215, 2012.

[13] J. Wu, Z. Lan, J. Lin, M. Huang, and P. Li, "Effect of solvents in liquid electrolyte on the photovoltaic performance of dye-sensitized solar cells," *J. Power Sources*, vol. 173, no. 1, pp. 585–591, 2007.

[14] Z. S. Wang, K. Sayama, and H. Sugihara, "Efficient eosin Y dye-sensitized solar cell containing Br -/Br3- electrolyte," *J. Phys. Chem. B*, vol. 109, no. 47, pp. 22449–22455, 2005.

[15] N. Papageorgiou, "An Iodine/Triiodide Reduction Electrocatalyst for Aqueous and Organic Media," *J. Electrochem. Soc.*, vol. 144, no. 3, p. 876, 1997.

[16] P. Wang, S. M. Zakeeruddin, J.-E. J. E. Moser, and M. Grätzel, "A new ionic liquid electrolyte enhances the conversion efficiency of dye-sensitized solar cells," *J. Phys. Chem. B*, vol. 107, no. 48, pp. 13280–13285, 2003.

[17] B. Li, L. Wang, B. Kang, P. Wang, and Y. Qiu, "Review of recent progress in solid-state dye-sensitized solar cells," *Sol. Energy Mater. Sol. Cells*, vol. 90, no. 5, pp. 549–573, 2006.

[18] N. Mohmeyer, P. Wang, H.-W. H.-W. Schmidt, S. M. Zakeeruddin, M. Gr�tzel, and M. Grätzel, "Quasi-solid-state dye sensitized solar cells with 1,3:2,4-di-O-benzylidene- D-sorbitol derivatives as low molecular weight organic gelators," *J. Mater. Chem.*, vol. 14, no. 12, pp. 1905–1909, 2004.

[19] J. Y. Song, Y. Y. Wang, and C. C. Wan, "Review of gel-type polymer

electrolytes for lithium-ion batteries," *J. Power Sources*, vol. 77, no. 2, pp. 183–197, 1999.

[20] J. Wu *et al.*, "Progress on the electrolytes for dye-sensitized solar cells," *Pure Appl. Chem.*, vol. 80, no. 11, pp. 2241–2258, 2008.

[21] K. Kakiage, Y. Aoyama, T. Yano, K. Oya, J. Fujisawa, and M. Hanaya, "Highly-efficient dye-sensitized solar cells with collaborative sensitization by silyl-anchor and carboxy-anchor dyes," *Chem. Commun.*, vol. 51, no. 88, pp. 15894–15897, 2015.

[22] B. He, X. Meng, and Q. Tang, "Low-Cost Counter Electrodes From CoPt Alloys For Efficient Dye-Sensitized Solar Cells," *ACS Appl. Mater. Interfaces*, vol. 6, no. 7, pp. 4812–4818, 2014.

[23] P. Yang and Q. Tang, "A branching NiCuPt alloy counter electrode for high-efficiency dye-sensitized solar cell," *Appl. Surf. Sci.*, vol. 362, pp. 28–34, 2016.

[24] M. S. Wu, C. Y. Chen, Y. R. Chen, and H. C. Shih, "Synthesis of bimodal mesoporous carbon with embedded nickel nanoparticles through pyrolysis of nickel-organic framework as a counter-electrode catalyst for dye-sensitized solar cells," *Electrochim. Acta*, vol. 215, pp. 50–56, 2016.

[25] J. M. Kim and S. W. Rhee, "Electrochemical properties of porous carbon black layer as an electron injector into iodide redox couple," *Electrochim. Acta*, vol. 83, pp. 264–270, 2012.

[26] S. Ahmad, J.-H. Yum, Z. Xianxi, M. Grätzel, H.-J. Butt, and M. K. Nazeeruddin, "Dye-sensitized solar cells based on poly (3,4-ethylenedioxythiophene) counter electrode derived from ionic liquids," *J. Mater. Chem.*, vol. 20, no. 9, p. 1654, 2010.

[27] Y. Qiu, S. Lu, S. Wang, X. Zhang, S. He, and T. He, "High-performance polyaniline counter electrode electropolymerized in presence of sodium dodecyl sulfate for dye-sensitized solar cells," *J. Power Sources*, vol. 253, pp. 300–304, 2014.

[28] L. Wang *et al.*, “Composite catalyst of rosin carbon/Fe3O4: highly efficient counter electrode for dye-sensitized solar cells.,” *Chem. Commun. (Camb).*, vol. 50, no. 14, pp. 1701–3, 2014.

[29] J.-H. He, Y. Liu, L.-F. Mo, Y.-Q. Wan, and L. Xu, “Electrospun nanofibres and their applications,” *iSmithers, Shawbury, Shrewsbury, Shropshire, UK*, p. 260, 2008.

[30] O. Of, “Vol. 7 No 4, 04024(4pp) (2015) Ж,” vol. 7, no. 4, pp. 4–7, 2015.

[31] H. Seo and Y. Wang, “International Conference on Recent Trends in Physics 2016 (ICRTP2016),” *J. Phys. Conf. Ser.*, vol. 755, p. 11001, 2016.

[32] S. H. Hwang, C. Kim, H. Song, S. Son, and J. Jang, “Designed Architecture of Multiscale Porous TiO2 Nano fi bers for Dye- Sensitized Solar Cells Photoanode,” *ACS Appl. Mater. Interfaces*, vol. 4, pp. 5287–5292, 2012.

[33] L. Yang and W. W. F. Leung, “Application of a bilayer TiO2 nanofiber photoanode for optimization of dye-sensitized solar cells,” *Adv. Mater.*, vol. 23, no. 39, pp. 4559–4562, 2011.

[34] F. H. Bijarbooneh *et al.*, “Structurally stabilized mesoporous TiO[sub 2] nanofibres for efficient dye-sensitized solar cells,” *APL Mater.*, vol. 1, no. 3, pp. 32106–32107, 2013.

[35] S. Chuangchote, T. Sagawa, and S. Yoshikawa, “Efficient dye-sensitized solar cells using electrospun Ti O2 nanofibers as a light harvesting layer,” *Appl. Phys. Lett.*, vol. 93, no. 3, pp. 2012–2015, 2008.

[36] A. Hagfeldt and M. Grätzel, “Molecular photovoltaics,” *Acc. Chem. Res.*, vol. 33, no. 5, pp. 269–277, 2000.

[37] X. Song, Q. Qi, T. Zhang, and C. Wang, “A humidity sensor based on KCl-doped SnO2 nanofibers,” *Sensors Actuators, B Chem.*, vol. 138, no. 1, pp. 368–373, 2009.

[38] Z. Zhang *et al.*, “Electrospun nanofibers of ZnO-SnO2 heterojunction with high photocatalytic activity,” *J. Phys. Chem. C*, vol. 114, no. 17, pp. 7920–

7925, 2010.

[39] B. Levy, W. Liu, and S. E. Gilbert, “Directed Photocurrents in Nanostructured TiO $_2$ /SnO $_2$ Heterojunction Diodes,” *J. Phys. Chem. B*, vol. 101, no. 10, pp. 1810–1816, 1997.

[40] A. A. Madhavan *et al.*, “Electrospun continuous nanofibers based on a TiO2–ZnO–graphene composite,” *RSC Adv.*, vol. 3, no. 47, p. 25312, 2013.

[41] Z.-Q. Liu *et al.*, “ZnO/SnO2 hierarchical and flower-like nanostructures: facile synthesis, formation mechanism, and optical and magnetic properties,” *CrystEngComm*, vol. 14, no. 6, p. 2289, 2012.

[42] A. Birkel *et al.*, “Highly efficient and stable dye-sensitized solar cells based on SnO $_2$ nanocrystals prepared by microwave-assisted synthesis,” *Energy Environ. Sci.*, vol. 5, no. 1, pp. 5392–5400, 2012.

[43] S. Zhang, B. Yin, Y. Jiao, Y. Liu, F. Qu, and X. Wu, “Nanosheet based SnO2 assembles grown on a flexible substrate,” *Appl. Surf. Sci.*, vol. 305, pp. 626–629, 2014.

[44] A. Van Der Heide and a Schönecker, “Mapping of contact resistance and locating shunts on solar cells using resistance analysis by mapping of potential (RAMP) techniques,” *... Photovolt. Sol. ...*, 2000.

[45] J. R. Bellingham, P. W.A., and C. . Adkins, “Electrical and optical properties of amorphous indium oxide,” *J. Pphys. Condens. Matter*, vol. 2, no. 6207–6221, 1990.

[46] K. Sreenivas, T. Sudersena Rao, A. Mansingh, and S. Chandra, “Preparation and characterization of rf sputtered indium tin oxide films,” *J. Appl. Phys.*, vol. 57, no. 2, pp. 384–392, 1985.

[47] Y. Shigesato, S. Takaki, and T. Haranoh, “Electrical and structural properties of low resistivity tin-doped indium oxide films,” *J. Appl. Phys.*, vol. 71, no. 7, pp. 3356–3364, 1992.

CHAPTER 3:

FABRICATION AND CHARACTERIZATION TECHNIQUES

3.1 Nanofibers Deposition Techniques:

There are multiple techniques which are currently being used to make nano-fibres. These nano-fibres are generated with different internal morphology including porous, core-shell, hollow and in micro-tubular arrangement. These fibres may differ in diameter ranging from several microns to below 100nm. There are various types of materials that can be obtained by different nano-fibres fabrication techniques. The most appropriate and suitable one is Electro-spinning[1].

3.2 Electrospinning:

3.2.1 Solution Electrospinning

Electro-spinning is a process of fabricating continuous fibres[2] ranging from 20nm to several micro meters. More than fifty different polymers have been successfully electro-spun into ultra fine fibres with diameters ranging from <3 nm to over 1 mm. In 1934, Formhals worked on production of artificial filaments using high electric field. He concluded that when a suitable electrically charge material is brought near to a droplet of the solution held in a capillary tube of very small diameter, cone shape jets are formed at the tip of the needle. There are four basic components of a simple electro-spinning process,

1. A High Voltage Supplier (ranging from 5kV-30kV)
2. A Motor pump to control the solution feed rate (ranging from several ul/h to ml/h)
3. A capillary Tube (small diameter needle)
4. A metal collecting screen (flat plate, Rotating drum e.tc)

The high voltage is connected to the needle. The voltage creates an electrically charged jet of polymer solution which forms a Taylor cone on the edge of the needle[3]. Taylor cone is a conical shape cone formed at the tip of the needle/capillary tube. This cone is formed due to the hemispherical shape of the solution at the needle tip with increase in voltage[4]. Due to the effect of the electrostatic force, the pulled polymer solution jet passes through an elongation and instability phase, which makes the jet very thin and long.

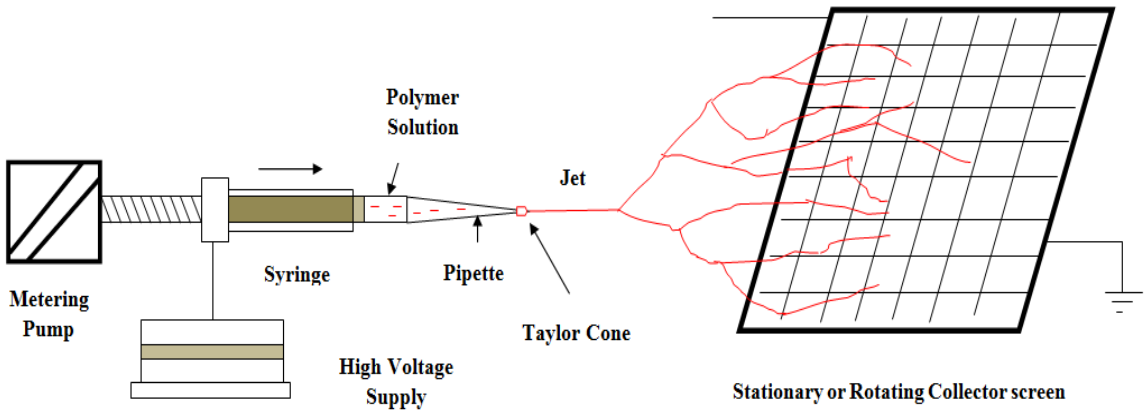

Figure 3.1 Schematic Diagram of Solution Electro-spinning

The solvent evaporates leaving behind a charged polymer fibre which got attached to the collector plate in front of the needle. The collector plate is grounded. This collector plate can be an Aluminium foil, ITO/FTO, Metallic collector, rotating drum. Electro-spinning is conducted at room temperature and suitable humidity.

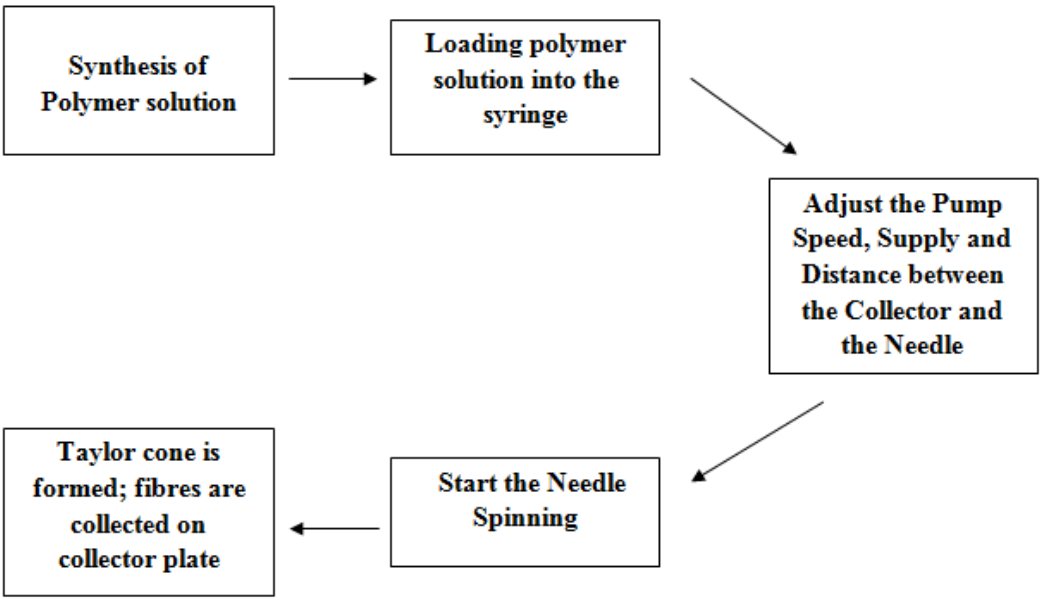

Figure 3.2 Step-wise synthesis of Nano-fibers production using Electro-spinning

3.2.2 Co-axial Electro-spinning:

This technique can be used to combine two different solutions/melts to make their composite nano-fibres. The solutions contact each other at the tip of the needle[5] where a high voltage stretches the droplet of the solution into a taylor cone. During the complete spinning process, the solvent evaporate leaving behind the mixed nano-fibres of both the solutions.

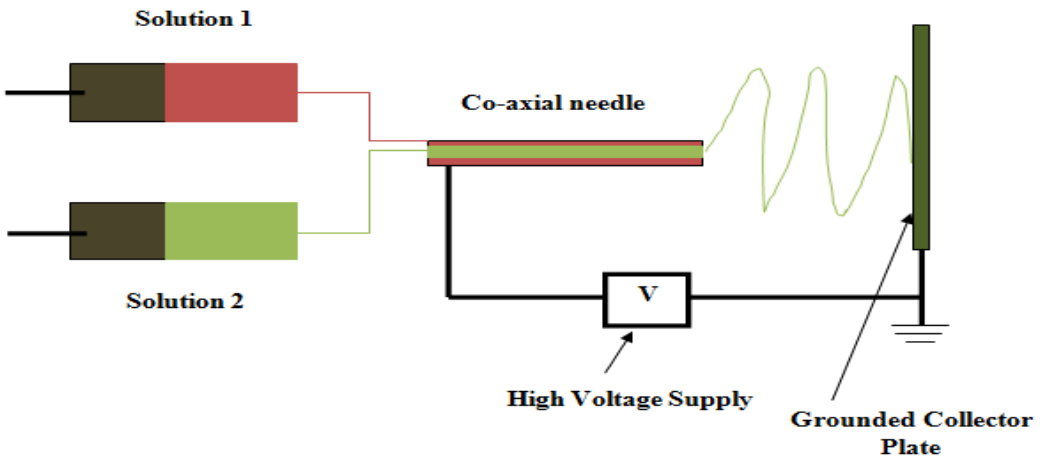

Figure 3.3 Schematic Diagram of Co-axial Electrospinning

Materials that cannot be electro-spun by solution electo-spinning can easily be spun by using this technique. Moreover, Polymer nano-tubes can also be created by this technique[6].

3.2.3 Melt Electro-Spinning:

For polymer materials, molten at higher temperature can be converted to nano-fibres using Melt Electro-spinning. Unlike solution electro-spinning, Melt electro-spinning is performed in vacuum conditions[7]. The polymer solution is heated through-out the spinning process, so that the solution remains in the molten state. In this type of spinning, the distance between the collector and needle is very small as ejected jet solidifies while travelling in the air[8]. Similarly large charge is applied because jet initiation is difficult in this type of spinning[9]. In most cases vertical electro-spinning in used.

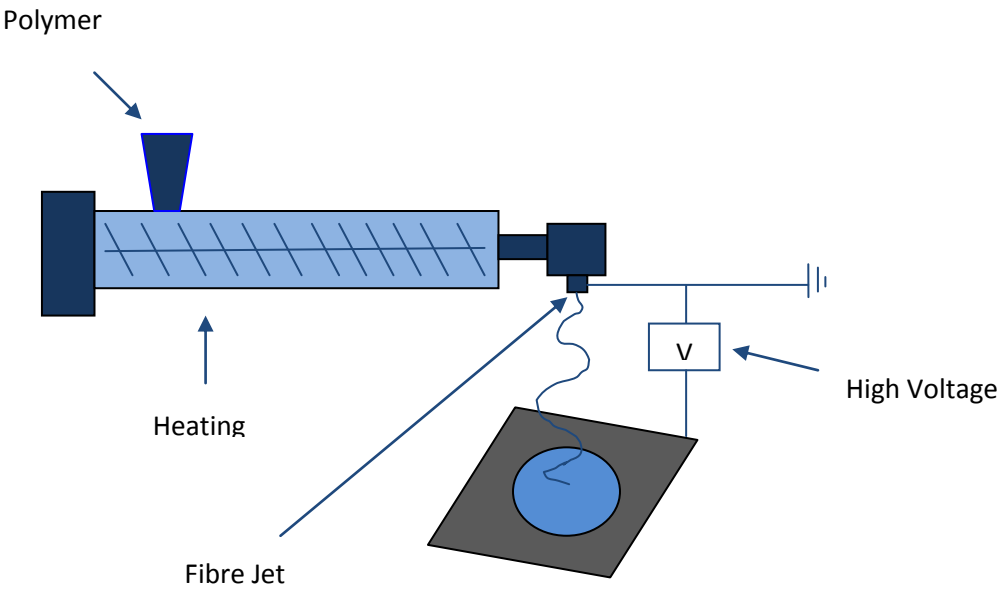

Figure 3.4 Schematic Diagram of Melt-Electrospinning

3.2.4 Magneto Electro-spinning:

A magnetic field is applied[10] in the presence of electric force, which results in shrinking of the jet. This shrinking of fibre results in increasing the radius of the whipping circle.

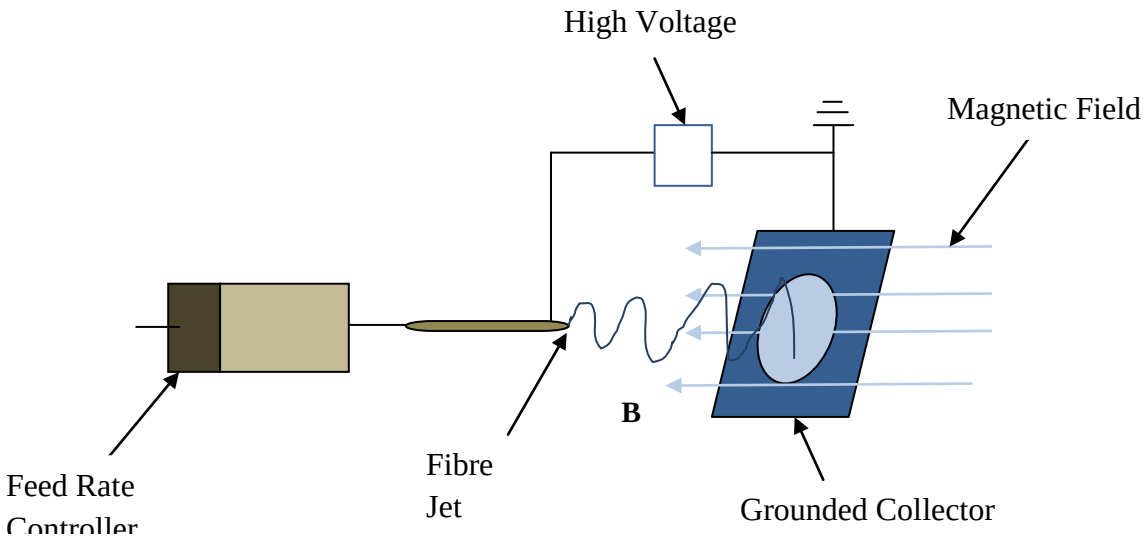

Figure 3.5 Schematic diagram of Magneto-Electrospinning

The magnetic field affects the swing of the fiber jet in such a way that with increase is magnetic field, the swing of the fibre decreases. This type of spinning results in production of nano-sized fibre in the range of 5nm to 100nm. This technique is not suitable for mass production

3.3 Vacuum Based Deposition Techniques:

3.3.1 Physical Vapour deposition:

Physical vapour deposition is a technique for the deposition of thin film by using ultra-high pressure and vacuum environment. It includes techniques like ion plating, electron beam evaporation and sputtering. The thickness of the deposited film may vary from several angstrom to millimetres depending upon the requirement. PVD is a flexible technique because it can deposit nearly all type of in-organic materials like alloys, mixtures, metals and others.

Physical vapour deposition technique mainly includes,

1. Evaporation

2. Sputtering

3.3.1.1 Evaporation:

In evaporation, thermal energy is required for the deposition of thin films on the substrate. The material to be deposited is placed inside a crucible and thermal energy is supplied to the crucible for the evaporation of the atoms. These evaporated atoms moves through the evacuated space between the crucible and substrate and stick to the surface of the substrate.

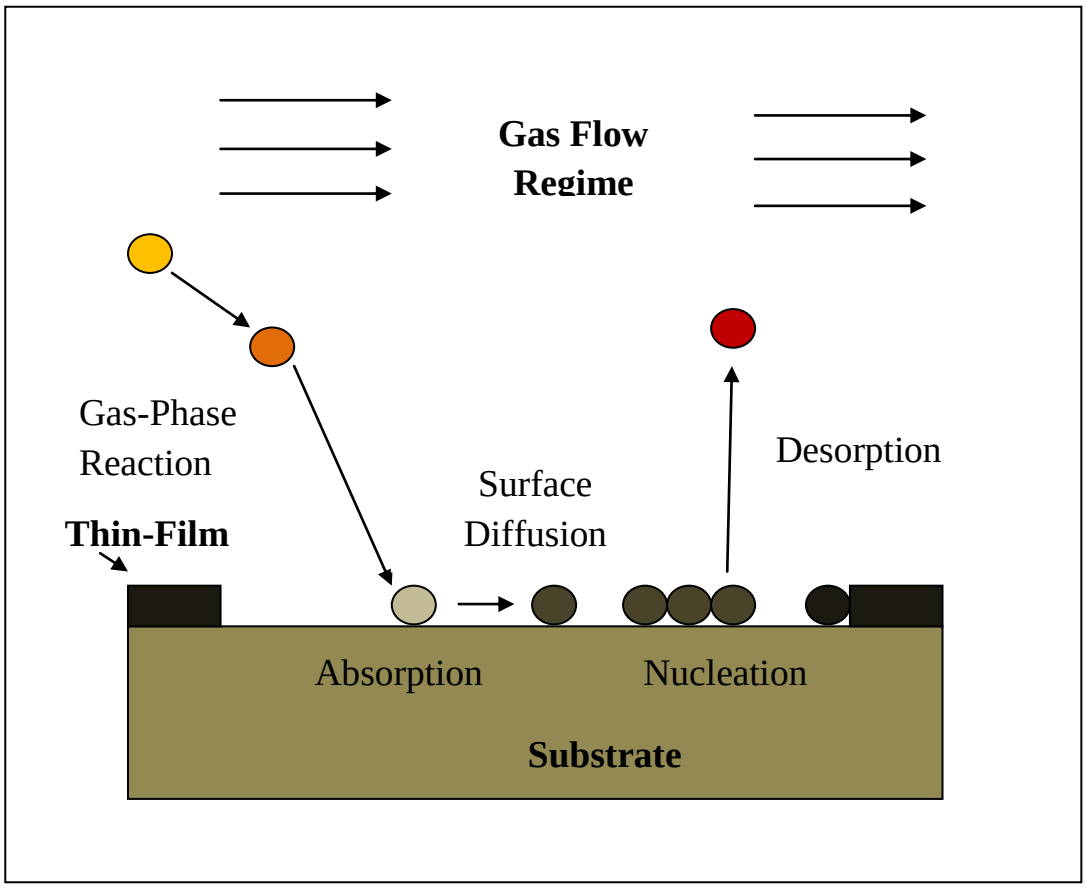

Figure 3.6 Basic Working of Evaporation (CVD)

A suitable pressure is created inside the chamber and the thermal energy is supplied using.

1. Resistance - W, Mo, Ta filament.

2. Electron- beam.

The reaction on the surface of the substrate is very fast which leads to the improper arrangement of the atoms on the surface. This affects the topology, film thickness

and step coverage of the film deposited. Moreover, in case of deposition of alloy, evaporation is difficult to carry out because of the different vapour pressures.

3.3.1.2 Sputtering:

Sputtering is another type of PVD which involves the ejection of material from the source and deposition of that material onto the substrate. A strong vacuum and plasma is created for the ejection and deposition of the source material.

A typical sputtering process consist of following steps,

1. The source material and the target are placed inside a vacuum chamber.

2. A suitable voltage is applied to the target and source, such that, the target is attached to the cathode and substrate to the anode.

3. Plasma is created inside the chamber by inserting a sputtering gas (usually Argon).

4. Current flow in between the two electrodes (anode and cathode) which leads to the formation of Ar+ ions. These Ar+ ions collide with other Argon molecules to create more Ar+ ions and electrons. This effect is known as avalanche multiplication effect.

5. The ionized atoms of the sputtering gas bombard the target and sputter the source material.

6. These sputtered atoms are transported to the substrate for deposition/coating[11].

Sputtering begins when an electron moves from cathode to anode and collides with a sputtering gas atom and forms a positively charged ion. Pressure is maintained inside the chamber for maximum collision between the electron and sputtering gas atom. With increase in collision, current increases which leads the plasma to become self-sustaining. To further maintain the plasma every electron has to maintain and produce sufficient secondary emission. In some cases, collision can also result in glow discharge instead of ions production.

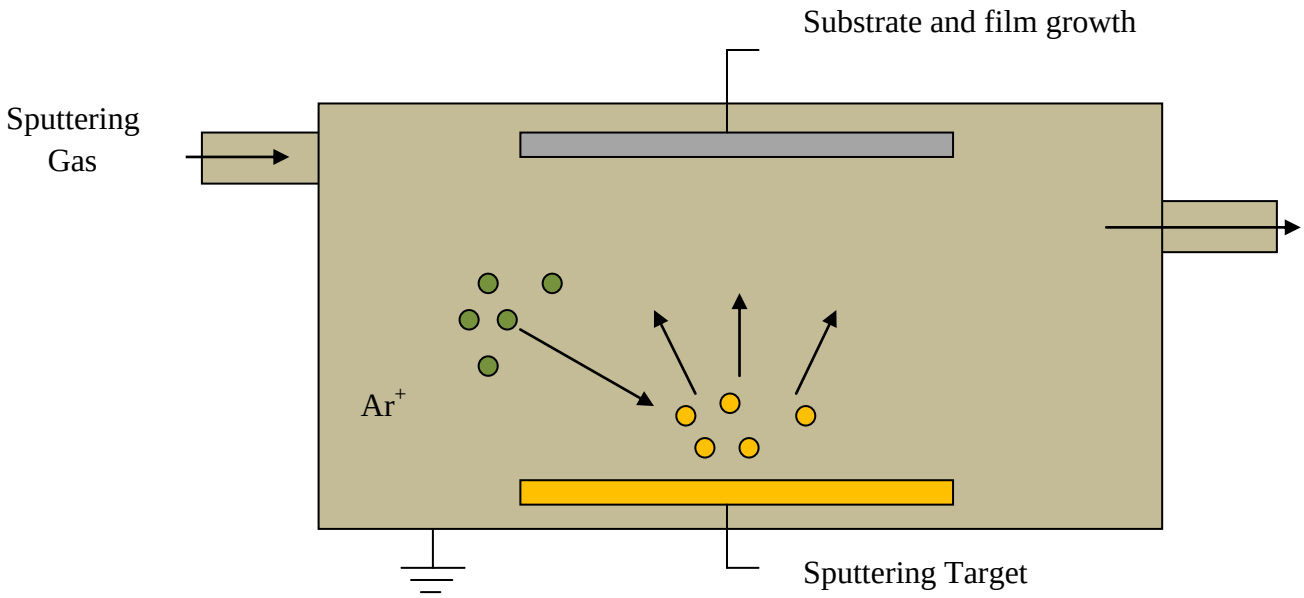

Figure 3 Schematic Diagram of Sputtering

Sputtering is divided into two types depending upon the voltage source,

1. **DC Sputtering** - utilize a DC gaseous discharge (DC voltage source).

2. **RF Sputtering** - Power supply is a high voltage RF source fixed at 13.56 MHz.

RF sputtering can be use to deposit metal, semi-conductors as well as insulators. In case of this type of sputtering, in the first cycle the source is given negative charge which lead to polarization on the surface of the source. This polarization results in the attraction of sputter gas atoms on the source and knocking off of the source atoms. In the other cycle when target is given a positive charge, the source atoms are ejected from the surface due to reverse polarization and are accelerated towards the substrate for deposition.

	DC Sputtering	**RF Sputtering**
Current Source	Use DC current source	Use AC current source fixed at 13.56 MHz connected with a impedance matching network

Sputter materials	Can only sputter conductive materials	Can sputter metal, semi-conductors and even insulators.
Cost	Less Costly	Expensive,Require impedance matching network along with the current source
Speed	Fast	Slow , because of different number of cycles

Table 3.1 Comparison between DC sputtering and RF sputtering.

Types of Sputtering:

Sputtering is divided into following types,

1. **Magnetron Sputtering:** The sputtering gas is ionized by a magnetic field.

2. **Reactive Sputtering:** A chemical reaction takes place before deposition. Other gas like O_2, H_2 and N_2 are used to assist chemical reaction. The target material is different from the material deposited.

3. Ion Assisted Sputtering: A secondary ion beam is exposed on the substrate. Usually used to deposit carbon based materials like diamond.

3.3.2 Chemical Vapour Deposition:

Chemical vapour deposition is a widely used technique to deposit thin film. Unlike PVD, CVD have a gaseous source material. The source gas, other gases and the substrate are placed in a heated vacuum chamber where the required chemical reaction takes place converting the gases to form the desired material on the surface of the substrate. The operating temperature of the chamber varies from 400^{o}C-

1200^{o}C. The temperature/pressure must be optimized to get the required reaction on the substrate.

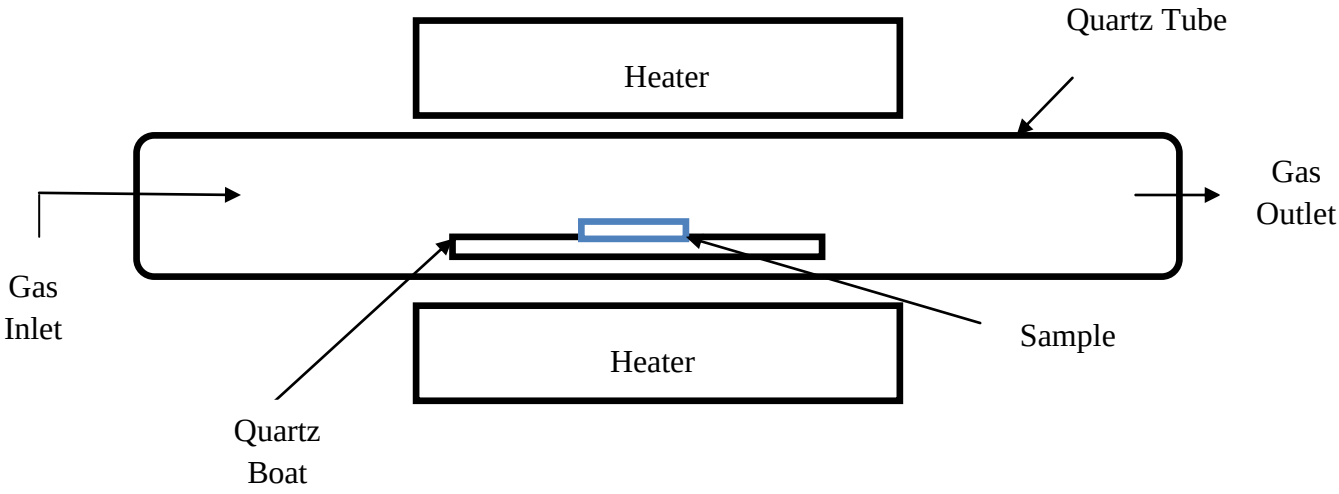

Figure 3.8 Basic working of CVD

A typical CVD process consist of following steps,

1. Transport of the reactants to the reaction chamber
2. Gas phase reaction.
3. Transport of the produced reactants to the surface of the substrate
4. Adsorption of the reactants (can be physical or chemical adsorption)
5. Reaction on the surface of the substrate, formation of thin film.
6. Desorption of the by-products from the surface of the substrate.
7. Transport of by-products away from the reaction chamber.

There are varies types of CVD depending upon the way in which the chemical reaction is initiated. This includes,

1. Atmospheric pressure CVD – Works at atmospheric pressure.
2. Low-pressure CVD – Works at sub-atmospheric pressure.
3. Plasma Enhanced CVD – Require plasma for the initiation of chemical reaction.

3.3.2.1 PECVD:

Plasma enhanced CVD uses plasma to get the required energy for the chemical reaction. The plasma is created by using RF electro-magnetic waves. Due to low temperature required (in the range of 200-400^{o}C) for PECVD and high growth rate of the material on the substrate, it is considered to be an efficient and cost effective method as compared to other vacuum based deposition techniques. Like a simple CVD process, PECVD process has following steps,

1. The substrate on which reaction is to be carried out is placed inside the reaction chamber.
2. Gases are inserted in the reaction chamber. These gases include the precursor gas and the carrier gas.
3. An RF electric field is applied to create plasma within the reaction chamber.
4. Active electrons of the carrier gas react with the precursor molecules to form free radicals.
5. The created free radicals move towards the substrate. These radicals are then bombarded /absorbed by the surface of the substrate.
6. The absorbed radical forms a layer on the substrate surface.
7. The by-products are pumped out of the chamber after the required thickness of the layer is achieved.

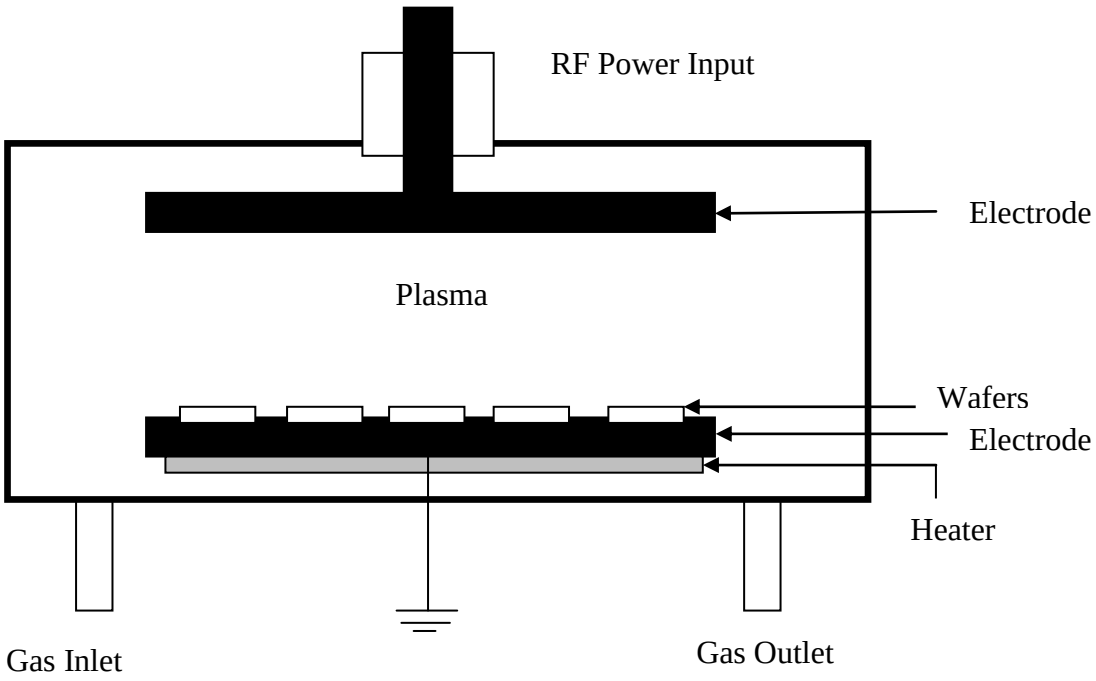

Figure 3.9 Schematic Diagram of Working of PECVD

3.4 Characterization Techniques:

In material sciences, Characterization is a widespread process to study material structure and properties. These properties include electrical properties, optical properties, morphology, chemical composition and elemental analysis. Characterization technique used in my work to analyze the prepared samples are,

3.4.1 XRD:

XRD is a versatile characterization technique that reveals the crystallographic information and chemical composition of the material. It is used for quantitative determination of the phase of the compound. Moreover it can also be used to identify the structural properties of the material like crystal structure, lattice parameters, orientation in crystalline components, cell volume, arrangement of atoms, type and length of chemical bonds and particle size [12].

Working Principle: "X-ray diffration works on the principle of constructive interference of refracted x-rays". Both constructive and destructive interference occurs when an X-ray interact with a matter. When a wavelength of incident X-ray is similar to the inter-atomic distance, diffration occurs. Diffration is actually the angle of reflection becomes equal to the angle of incidence. It is described with the help of Bragg's Law

$$2d\sin\theta = n\lambda$$

Where n= integer, λ = wavelength of X-rays, d= interplanar spacing, θ= diffraction angle. Constructive interference occurs, when Bragg's law is satisfied. The structural information of the material is determined by,

1. Position of the reflected rays provides information about the inter-layer spacing.

2. Peak intensity provides quantitative information about how much of the incident X-ray has contributed to the reflection.

3. Diffraction pattern provides information about the phases present in a sample, crystallinity of material, lattice parameters, crystal structure, cell volume, density etc.

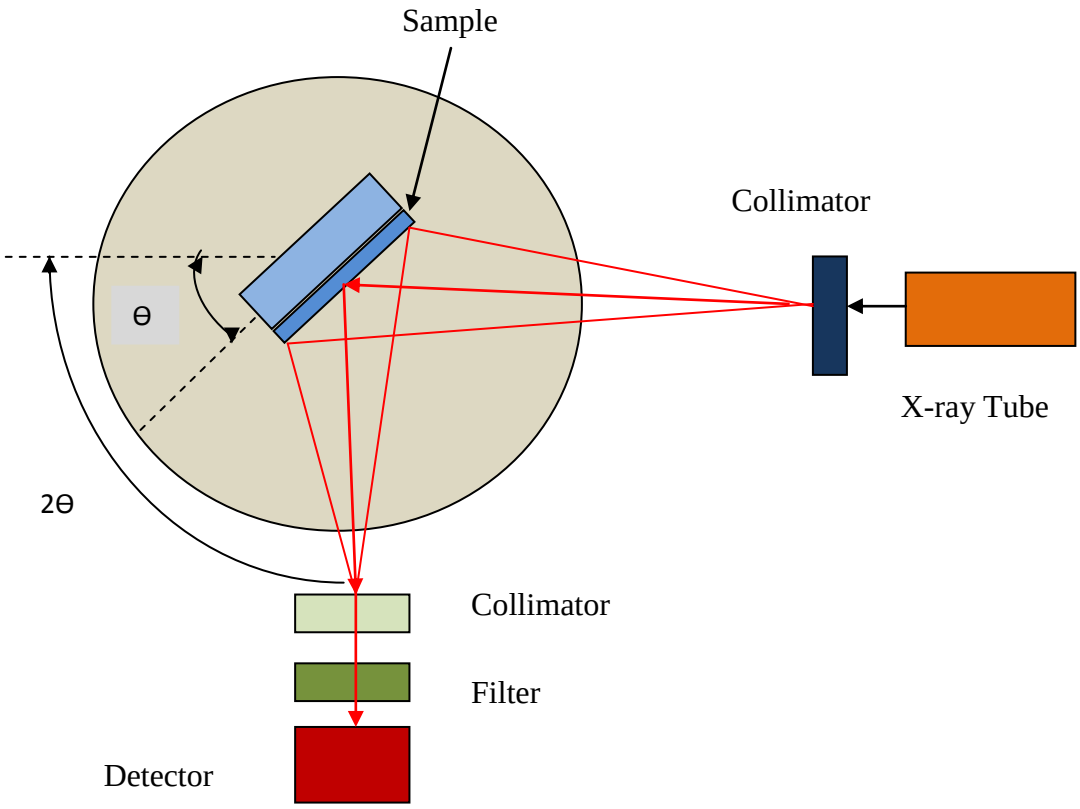

Figure 3.10 Schematic Diagram and components of XRD.

XRD consist of following components,

1. Sample holder - where sample is placed.

2. X-ray Source - A continuous X-ray spectrum is obtained when the electrons emitted from the cathode, dislodge the electrons from the target material. Most commonly used target material is Copper, with Cu Kα = 0.54nm (where Kα is the component of the spectra)

3. Mono-chromator - Filter the X-rays which afterwards strikes the sample

4. Goniometer - Rotate the sample.

5. Detector - swaps at an angle of 2θ and collects the diffracted X-rays. X-rays diffract and reflect from the layers of the crystal, giving rise to constructive interference. These patterns are collected.

3.4.2 SEM:

SEM is a imaging technique that is use to study the morphology, particle size and defects in films and powder by using a high energy electron beam. SEM gives magnification of the sample up to 300,000X.

Working principle: In presence of vacuum, when a high beam of electron strikes the sample, it gets scattered. This scattering results in the production of secondary electrons and back-scattered electrons. These electrons when knock out of the sample an electric current is generated which results in the formation of an image. Greater the number of electrons that strikes the sample, greater would be the magnification obtained [13]. The different types of electrons emitted give different types of information about the morphology of the sample,

1. Secondary Electron - surface topology and morphology of the material

2. Back scattered electron - distinctions in multi-phase samples [14].

Components of SEM includes,

1. Electron probe - An electron gun that is use as a source of electron beam. Guns use for generation of electron are,

- Field emission gun.
- Thermionic gun.

2. Specimen stage - sample is placed. This stage can rotate.
3. Electromagnetic lens - direct the electrons towards the sample.
4. Secondary electron detector - detected the ejected secondary electrons.
5. Image display unit - display the image of the sample.

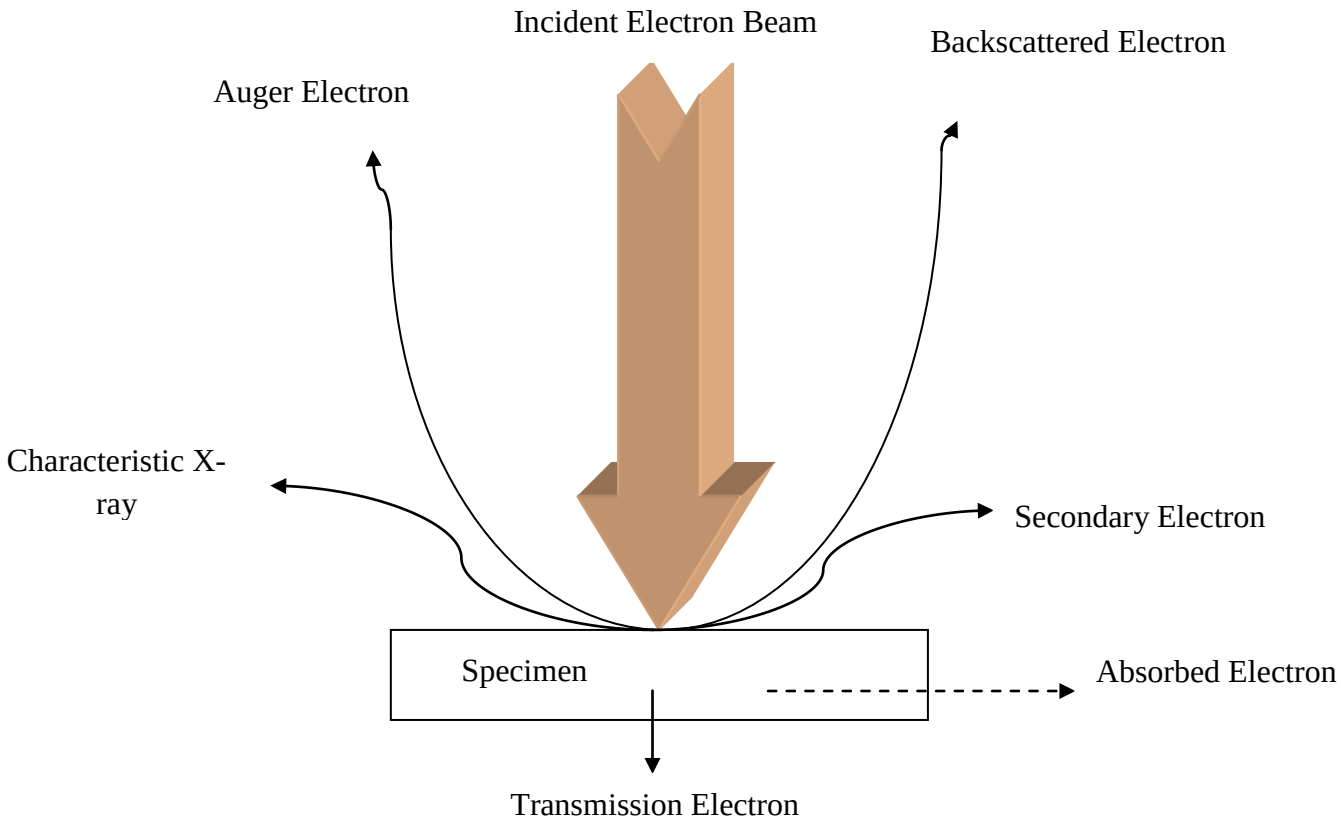

Figure 3.11 Diagram of basic phenomenon of electron beam interaction

3.4.2.1 Sample preparation:

SEM require proper sample preparation depending upon the imaging sample . For example

1. In case of insulator a coating of conductive film is deposited on the sample before imaging to avoid surface charging.
2. If sample is already conductive, no coating is required.
3. For a powder sample, the sample is directly placed on the stub for further imaging.
4. For a film, sample is prepared by cutting or slicing the sample in required size followed by mounting and polishing on the sample.

3.4.3 EDX:

Energy Dispersive X-ray Spectroscopy elemental analysis technique used for the qualitative as well as quantitative analysis of a material. Chemical composition of a sample, with elements having atomic number greater than 3, i.e from beryllium to uranium can be analyzed by using EDX.

Working principle: When high energy electron strikes the sample, electrons are excited to higher energy levels, leaving behind an electron vacancy. This electron vacancy is filled by a electron from the higher state by releasing an x-ray. These released x-rays (energy) is measured by EDX. The atomic structure of every element gives it a characteristic emission pattern. Every element emits x-ray with a characteristic energy values. Sample preparation of EDX is same as SEM. Main components of EDX analyzer are,

1. Electron beam
2. X-ray detector
3. Pulse processor
4. Analyzer

3.4.4 FT-IR:

FTIR stands for Fourier transform infra–red spectroscopy. This technique work in the infrared region of electro-magnetic spectrum. As compared to the visible region, infrared spectrum has low frequency and longer wavelength. Infrared region ranges from 12800~ 10cm-1. FTIR spectroscopy works in the infrared region of (4000 ~ 200 cm-1), because most of the organic and inorganic ions show absorption in this region. In IR spectroscopy, molecules show characteristic absorption of the infrared radiation, which helps in determining the structure of the molecule. This technique identifies the chemical bonding for thin films and solid samples. It is also used to identify the functional groups and impurities present in the sample.

Working principle: When the sample is irradiated by IR rays, sample molecules absorb rays which cause a change in the dipole moment of the molecule. This cause the vibrational energy levels to get transferred from ground to excited state, vibrational energy gap gives the frequency of absorption peak. The iintensity of the

peaks depends on the change of dipole moment and transitions among the energy levels. An FTIR spectrum is plotted between wave-number and absorbance/transmittance respectively. Compounds possess characteristic vibrational frequencies; hence FTIR spectroscopy is used to characterize inorganic, organic and biological molecules. Intensity of an IR band is directly proportional to the concentration of the chemical compound; thereby it can also be used for quantitative analysis. Components of FT-IR spectrophotometer include:

1. Source of IR radiation - Nernst Filament is use as a source.
2. Beam Splitter - Radiations are divided in to two beams of equal intensity. One passes through the sample and the other is taken as a reference beam.
3. Two Mirrors - reflect the beam passed through the sample and the reference beam toward a light chopping device. This device again transfers the beams to the mono-chromator which converts the polychromatic light to monochromatic light.
4. Detector - The monochromatic light containing sample and reference beam are detected , converted to electrical signal , amplifies and is obtained on a read-out device[14].

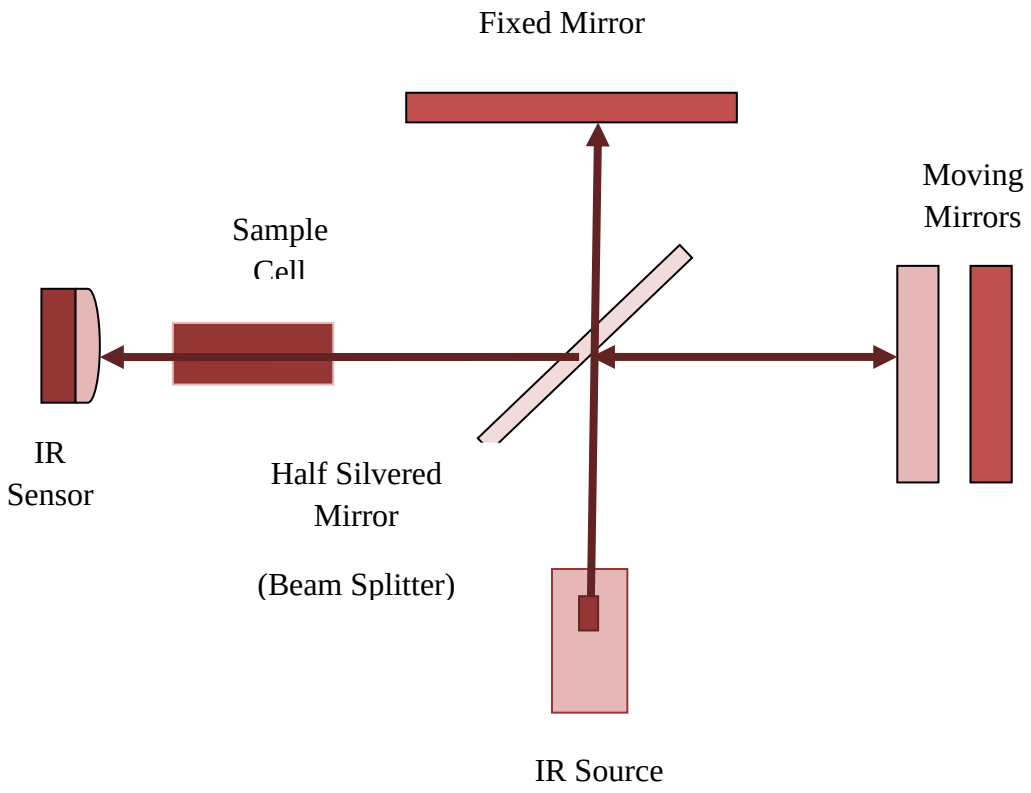

Figure 3.12 Schematic representation of FT-IR

3.4.5 UV-VIS Spectro-photo meter:

UV-VIS spectro-photo meter is use to study the absorption, transmittance and reflectance of a materials by the analytical information obtained within a certain wavelength. A light of certain wavelength (energy) is incident on the sample; some of the light is absorbed while remaining light is transmitted. Absorbance of light at a specific wavelength results in the excitation of electron. Energy difference between the already occupied orbital and the orbital to which the electron is promoted corresponds to the wavelength of absorbed radiation. Several bands are form in absorption spectrum because of this transition of electrons in orbitals. The photo-detector measures the energy of transmitted radiation which gives the absorbance of the sample.

Working Principle: It works on the principle of Beer-Lambert law. Which states that "when a monochromatic light beam passes through the solution, there comes a direct relation between rate of decrease in the intensity with thickness to the conc. of solution i.e., A=Ecl (where A=absorbance, E= absorptivity coefficient, l=path length, c=concentration of the solution). This relation is established as, transmittance refers to the ratio between transmitted light to incident light. Absorbance is the inverse of transmittance.

UV-VIS spectro-photometer consists of following components:

1. Source of Light: Hydrogen-deuterium discharge lamp and tungsten filament lamp are use as light source. Hydrogen-deuterium discharge lamp for UV radiation while tungsten filament lamp is use for visible region.
2. Mono-chromator: it consists of entrance slit, prism, exit slit and mirrors. A solenoid mirror is used to reflect UV radiations towards mono-chromator. It convert the poly-chromatic light to mono-chromatic light
3. Beam splitter: Through the exit slit of the mono-chromator light beam falls on beam splitter. It split light into two portions. One passes through the sample while the other through the reference compartment.
4. Optical Chopper: The reflected light beams from the sample and reference compartment is reflected to the optical chopper. The chopper rotates at with a frequency of 10 cycles/sec and reflects the two beams to the detector.

5. Detector: Photo-diode is use as a detector which convert the generated signals into electrical signal.
6. Read-out device: The generated electrical signal is amplified and obtained on read-on device as a graph between wavelength and absorption.

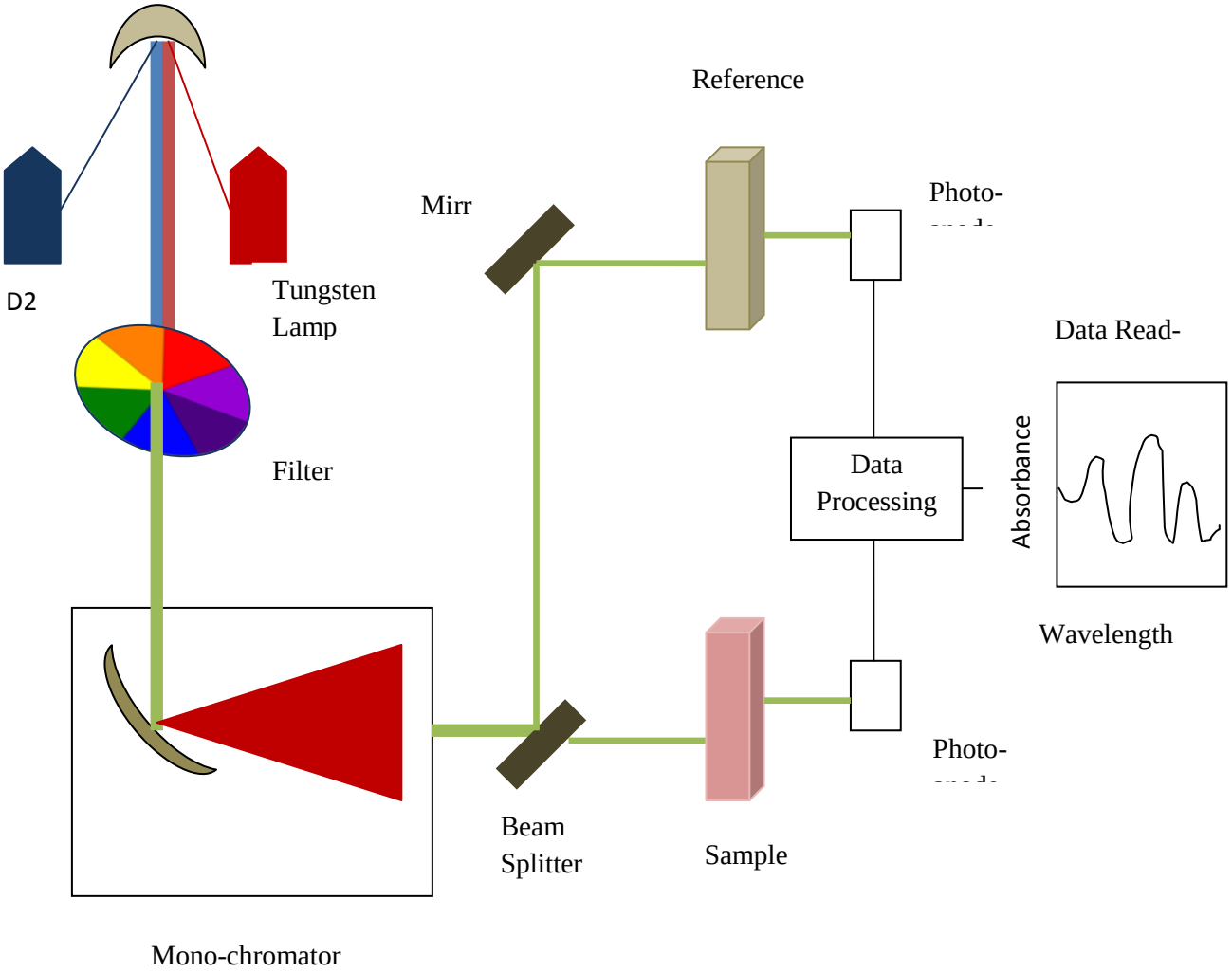

Figure 3.13 Schematic diagram and working of UV-VIS NIR Spectro-photometer

3.4.6 Hall Effect Measurement system

Hall Effect measurement system is use to determine the electrical properties of semi-conductor thin films like charge carrier type and density, mobility, conductivity, resistivity and sheet resistance.

Working principle: Hall Effect measurement system work on the principle of Lorentz force. Lorentz force is the combination of electric and magnetic force. When an electron moves along the electric field direction perpendicular to the applied magnetic field , it encounter an magnetic force equal to -qv X B. The direction of this magnetic force is determined by right hand rule, i.e in the opposite direction in which thumb is pointed. In this case the lorentz force is the combination of both electric and magnetic force and is calculated as, - q(**E** + **v** x **B**) where E is electric field and B is magnetic field. Suppose a constant current I flows along the x-axis in presence of z-directed magnetic field. The charges experience a lorentz force and a hall voltage is produce. In case of negative (n) charge, the current direction is towards the negative y-axis and in case of holes (p type), in the opposite direction. This calculated hall voltage can be use to calculate the bulk density/ charge density by ns=IB/qlVHl.

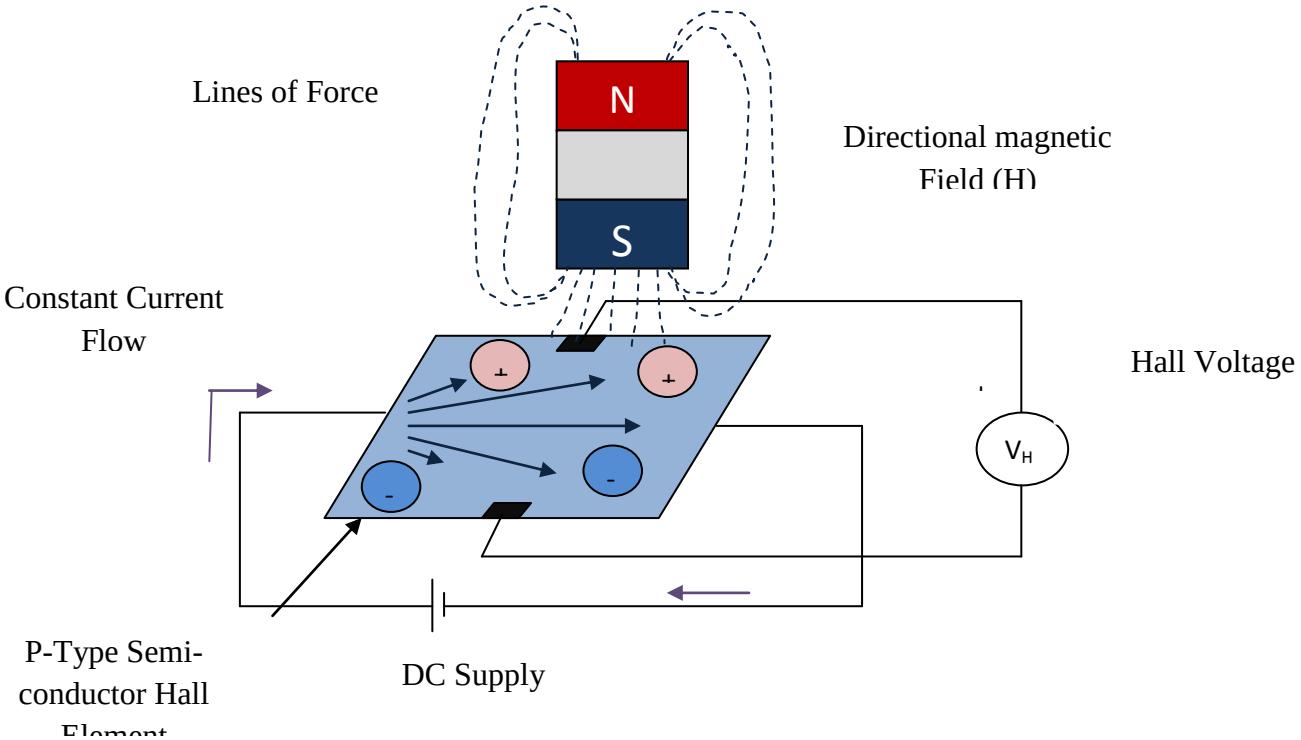

Figure 3.14 Schematic Description of Hall Effect Measurement System

Hall voltage is negative for n-type materials and positive for p-type materials. Now, the sheet resistance of the sample is determined by van der Pauw resistivity measurement technique. This technique requires four ohmic contacts and it require a

square sample of the conductive sample. In this measurement , van der Pauw resistivity measurement technique suggest that there are two types of resistance RA and RB , which are related to sheet resistance as,

exp(-πRA/RS) + exp(-πRB/RS) = 1. Mobility is calculated by $\eta=1/(qnsRs)$ and similarly bulk resistivity is calculated as $\varrho=Rsd$ is the conductive layer thickness i.e d is known.

Hall Effect measurement system can also be use to calculated IV or IR curves for a conductive film in the required range of current. For better measurements, the sample must have,

1. Flat sample of uniform thickness.
2. Better ohmic contacts. Sample must be symmetric.
3. Sample uniformity and its thickness must be known.

3.4.7 Ellipso-meter:

Ellipsometery is a optical thin film characterization technique that is use to determine the optical constants, Di-electric properties and the thickness of the film. Ellipsometery stands for “elliptically polarized light” , which means that it study the properties of the thin-film by the change in polarization. It is a technique in which the angle of incident and angle of reflection are equal.

Working Principle: When a incident radiation falls on the sample, there is a change in the polarization. The polarization state of the light before incident on the sample is sub-divided into two parts s and p where s is the oscillating perpendicular while p is oscillating parallel to the incident radiation.

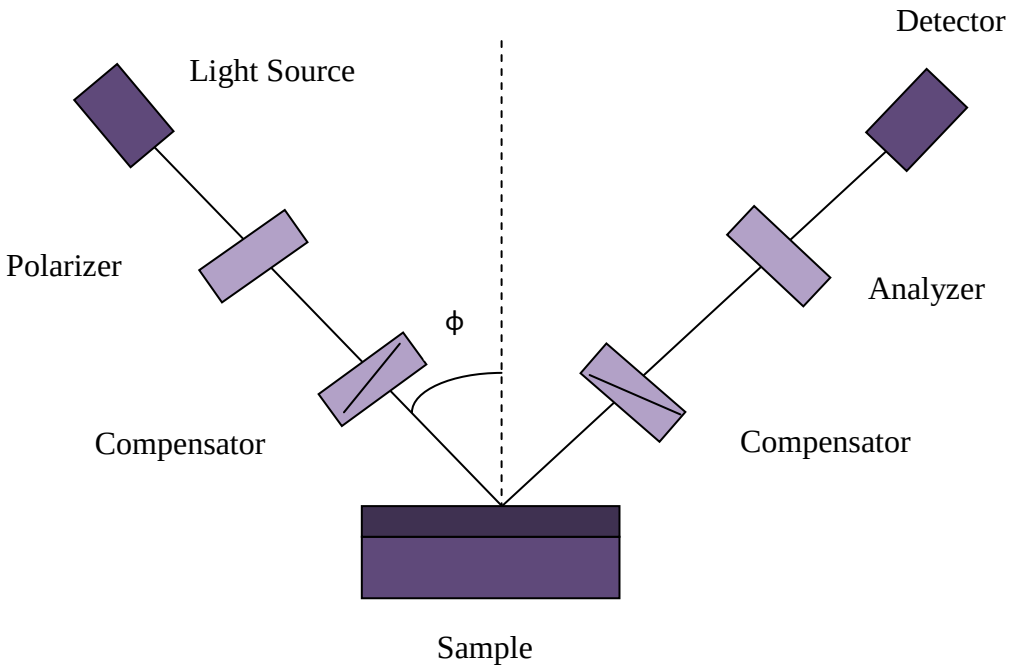

Figure 3.15 Schematic Diagram of Mechanism of Ellipsometery

After the light is reflected from the sample these counter parts of the polarized list change to rs and rp. This change in polarization quantify two quantities, Ψ (amplitude ratio) and Δ (phase difference). Afterwards the generated signal depends on the thickness of the sample. It can thus determine the thickness of single or multi-layer sample with great accuracy because each layer has different polarization with respect to the incident radiation.

Ellipsometer have following components,

1. Light Source - Emit Electro-magnetic light.

2. Polarizer - linearly polarize the light.

3. Optical compensator.

4. Sample stage - sample is placed here. The polarized light falls on the sample and is reflected back.

5. Analyzer - it is like a polarizer which transfers the reflected light to the detector.

6. Detector - Detected the reflected light.

3.4.8 2-4 probe meter:

2 and 4 probe meter is used to determine the resistivity or conductivity of the thin-film. These techniques give voltage from different values of current. These current and voltage gives the resistivity.

3.4.8.1 2 Probe Meter:

For a sample of uniform surface, the resisivity is measured by the voltage drop created by the passage of variable current. In 2 probe meter current is supplied (in from probe 1 and out from probe 2). The current is measured using ammeter. While the voltage drop created due to the current is measured using voltmeter. If the length of the sample as well as the area of cross-section is known, the resisitivity of the sample is calculated by

$$\rho = \frac{V}{I}\frac{A}{l}$$

There are several issues with 2 probe measurement like,

1. The voltage drop from the current flow will not be separable from the voltage drop in the device under test.

2. Contact Resistance of the measuring probes.

3.4.8.2 4 Probe Meter:

In 4 probe meter, 4 tungsten probes are used. A current is supply via 2 outer probes and the voltage across these 2 probes is measured by the 2 inner probes. Voltmeter is use to measure the voltage. Probe spacing is usually ≈ 1mm.

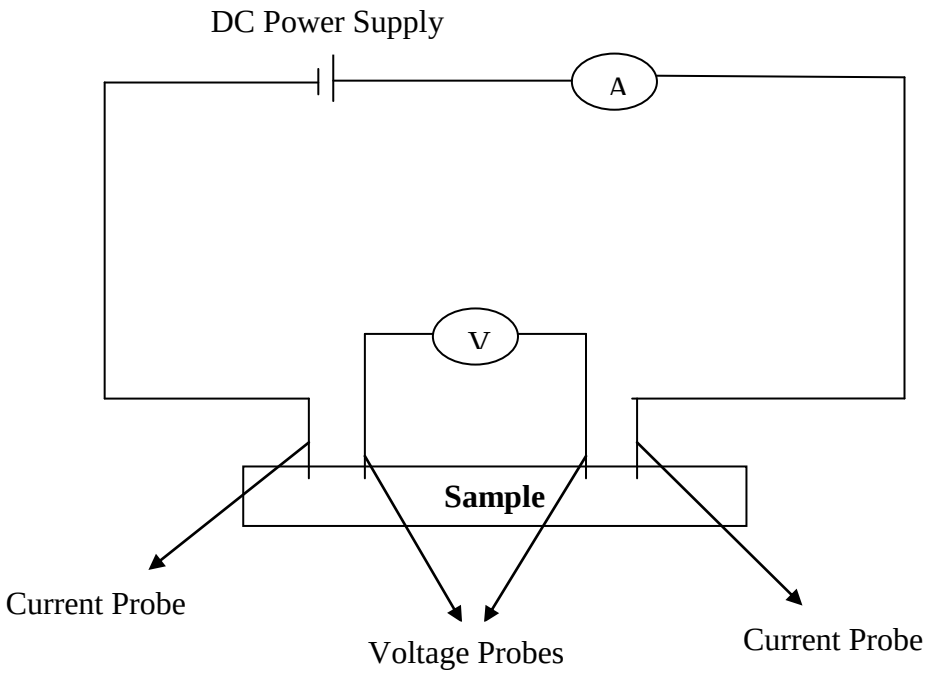

Figure 3.16 Pictorial Description of 4-probe measurements

Due to high impedance of the voltmeter, the inner two probes will not draw any current which annihilate the contact resistance as voltage drop can easily be separated from the current flow. The voltage drop in the current carrying wire will not affect the overall voltage drop.

Summary:

This chapter gives an overview of experimental and characterization techniques used forr this research. For fabrication of nano-fibres electro-spinnning and co-axial electro-spinning is used. Characterization of the prepared films is performed via SEM, XRD, FT-IR, EDS and Hall Effect measurement system. A-Si solar cells were fabricated using PECVD for deposition of passivation layer and emitter layer while sputtering was done to deposit TCO (ITO) and metallic contacts (Ag). For contact resistance measurement of the a-Si hetro-junction solar cells, the measurements of resistance and I-V in dark for transfer length measurement (TLM) patterns were performed via 4-probe, 2-probe measurement technique and multi-meter. For Indium oxide (IO) as transparent conductive oxide layer (TCO) of a-Si hetro-junction solar cells, the deposition is carried out via RF sputtering tool and the thickness was measurement using ellipsometery, and electrical properties was studied using hall effect measurement system

Reference

[1] Y. E. Kiyak and E. Cakmak, "Nanofiber Production Methods," *Electron. J. Text. Technol. Tekst. Teknol. Elektron. Derg. Kiyak E.Y., Cakmak E. Electron. J. Text. Technol.*, vol. 8, no. 83, pp. 49–6049, 2014.

[2] W. E. Teo and S. Ramakrishna, "A review on electrospinning design and nanofibre assemblies," *Nanotechnology*, vol. 17, no. 14, 2006.

[3] J. M. Deitzel, J. D. Kleinmeyer, J. K. Hirvonen, and N. C. B. Tan, "Controlled deposition of electrospun poly (ethylene oxide) ® bers," *Polymer (Guildf).*, vol. 42, pp. 8163–8170, 2001.

[4] G. Taylor, "Electrically Driven Jets," *Proc. R. Soc. A Math. Phys. Eng. Sci.*, vol. 313, no. 1515, pp. 453–475, 1969.

[5] Y. Wu, J. Y. Yu, J. H. He, and Y. Q. Wan, "Controlling stability of the electrospun fiber by magnetic field," *Chaos, Solitons and Fractals*, vol. 32, no. 1, pp. 5–7, 2007.

[6] L. A. Andrady, "Science and Technology of Polymer Nanofibers.," *Sci. Technol. Polym. Nanofibers*, pp. 1–26, 2008.

[7] L. Larrondo and R. S. J. Manley, "Electrostatic fiber spinning from polymer melts. II. Examination of the flow field in an electrically driven jet," *... Polym. Sci. Polym. ...*, vol. 19, pp. 921–932, 1981.

[8] A. Patanaik, R. D. Anandjiwala, R. S. Rengasamy, A. Ghosh, and H. Pal, "Nanotechnology in fibrous materials-a new perspective," *Text. Prog.*, vol. 39, no. 2, pp. 67–120, 2007.

[9] T. Mitarai, A. Shander, M. Tight, N. Fabrics, F. N. Martin, and J. T. English, "An Introduction to electrospinning and nanofibres," *J. Cardiothorac. Vasc. Anesth.*, vol. 27, no. 4 Suppl, pp. S1-2, 2013.

[10] J.-H. He, Y. Liu, L.-F. Mo, Y.-Q. Wan, and L. Xu, "Electrospun nanofibres and their applications," *iSmithers, Shawbury, Shrewsbury, Shropshire, UK*, p.

260, 2008.

[11] J.E. Mahan, “Physical Vapor Deposition of Thin Film”, John Wiley & Sons, Inc. (2000), ISBM 0-471-33001-9.

[12] A. R. Clarke, Microscopy techniques for materials science. CRC Press (electronic resource), 2002

[13] J. Goldstein. Scanning electron microscopy and x-ray microanalysis. Kluwer Academia/Plenum Publishers, 2003

[14] R. F. Egerton. Physical principles of electron microscopy: an introduction to TEM, SEM, and AEM. Springer, 2005.

[14] Stuart, Barbara. Infrared Spectroscopy. John Wiley & Sons, Inc., 2005

CHAPTER 4:

EXPERIMENTATION

Following Experiments were performed to achieve the objectives of this research. Three different sets of experiments were performed and electrical properties were studied.

1. TiO_2, SnO_2 and TiO_2/SnO_2 nano-fibres deposition on conductive glass with graphene nano-platlets sensitization.

2. Various TLM pattern a-Si hetro-junction solar cells.

3. Indium oxide RF sputtering on glass and a-Si.

4.1 Synthesis of Metal Oxide nano-fibres:

TiO_2 and TiO_2/SnO_2 composite based nano-fibres were grown on conductive glass using Le-10 Bioinicia Electro-spinning setup. The conductive glass used was cleaned by sonication in distilled water followed by sonication in ethanol for 10 minutes. Aluminium foil and cleaned FTO was attached in front of the needle on the collector plate via a conductive carbon tape. Three types of fibres were grown and Electro-spinning parameters like voltage, feed rate and collector to needle distance was optimized to get the finest fibres.

4.1.1 TiO_2 nano-fibres:

Titanium iso-propoxide, absolute ethanol, Glacial acetic acid and, Poly-vinyl-pyrrolidone (PVP,Mw= 3,000,000 g·mol−1) were used to prepare TiO_2 nano-fibres. Solution of Ethanol and Glacial acetic acid was made in a ratio of 4:1, followed by stirring for 10 minutes. 1.8g PVP was added to the above solution to get a viscous polymer solution. After stirring the polymer solution for 1 hour, 0.5g of Titanium iso-propoxide was added to the solution. The colour of the solution changes to light yellowish. The solution was stirred until a homogenous mixture is obtained. This highly viscous polymeric solution was inserted into a 5ml syringe in a horizontally

attached electro-spinning setup. . A high voltage of 17.4kV was attached to the needle and the solution was injected to the needle at the feed rate of 750µl/h. The needle collector distance was set at 15cm. A stable taylor cone can be seen at the tip of the needle. The as-spun fibres deposited on FTO and Aluminium foil were dried for 1 hour at 100^{o}C in a vacuum oven. The heating rate was set at 1^{o}C/min. The dried nano-fibres were calcinated at 500^{o}C for 1 hour in a Tube furnace in Air. To reach the calcination temperature a heating rate of 3◦C/min was maintained. The isothermal plateau was maintained for 60 minutes and subsequent cooling was at the natural rate.

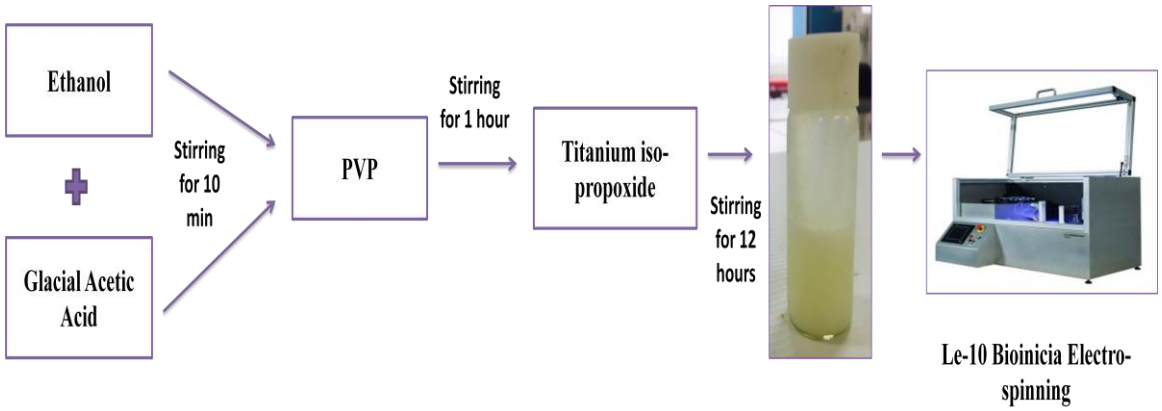

Figure 4.1 Schematic Representation of Synthesis of TiO_2 nano-fibres

4.1.2 SnO_2 nano-fibres:

Stannous chloride di-hydrate, absolute ethanol, Glacial acetic acid and, Poly-vinyl-pyrrolidone (PVP,Mw= 3,000,000 g·mol−1) were used to prepare SnO_2 nano-fibres. Solution of Ethanol and Glacial acetic acid was made in a ratio of 4:1, followed by stirring for 10 minutes. 1.8g PVP was added to the above solution to get a viscous polymer solution. After stirring the polymer solution for 1 hour, 0.5g of stannous chloride di-hydrate was added to the solution. The solution was stirred until a homogenous mixture is obtained. This highly viscous polymeric solution was injected into a 5ml syringe in a horizontally attached electro-spinning setup. . A high voltage of 19.3kV was attached to the needle and the solution was injected to the needle at the feed rate of 750µl/h. The needle collector distance was set at 15cm. A

stable taylor cone can be seen at the tip of the needle. The as-spun fibres deposited on FTO and Aluminium foil were dried for 1 hour at 100°C in a vacuum oven. The heating rate was set at 1°C/min. The dried nano-fibres were calcinated at 500°C for 1 hour in a Tube furnace in Air. To reach the calcination temperature a heating rate of 3°C/min was maintained. The isothermal plateau was maintained for 60 minutes and subsequent cooling was at the natural rate.

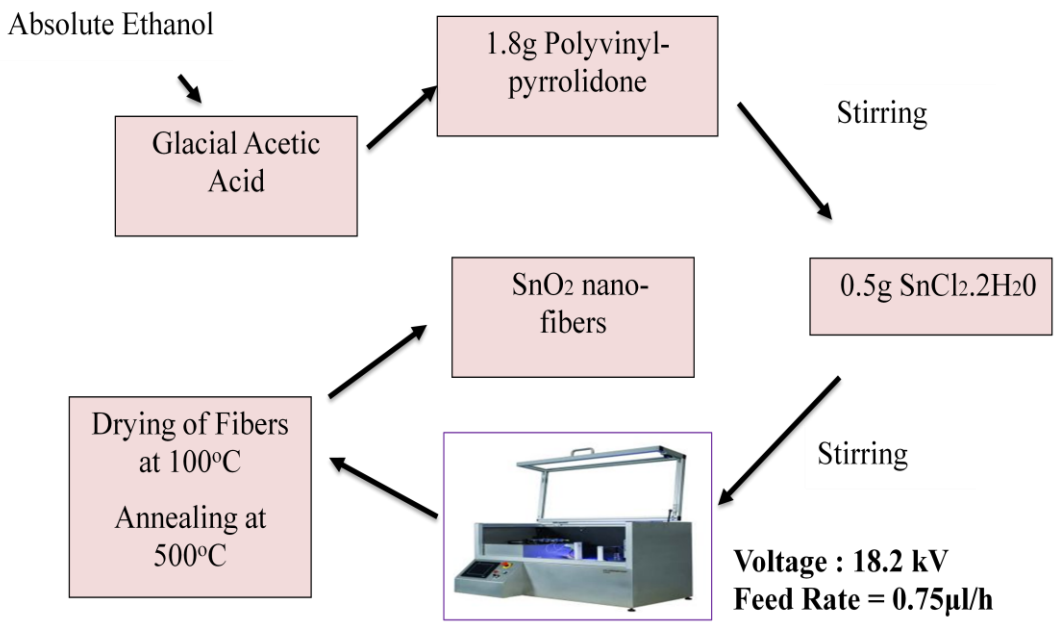

Figure 4.2 Step wise synthesis of SnO_2 nano-fibres

4.1.3 TiO_2/SnO_2 nano-fibres:

Like TiO_2 and SnO_2 nano-fibres, TiO_2/SnO_2 composite nano-fibres were also prepared using the same procedure. Solution of Ethanol and Glacial acetic acid was made in a ratio of 4:1, followed by stirring for 10 minutes. 2 different polymer concentrations were use to study solution concentration effect on fibre structure. The concentration of the materials was as shown in table.

	Ethanol	Glacial Acetic Acid	PVP	Titanium iso-propoxide	Stannic Chloride Di-hydrate
Solution A	4ml	1ml	1.6 g	0.25 g	0.2g
Solution B	4ml	1ml	1.8g	0.25 g	0.2 g

Table 4.1 Solvent, polymer and precursor ratio for Solution A and B of TiO_2-SnO_2 nano-fibres

This highly viscous polymeric solution was inserted into two 5ml syringes in a horizontally attached electro-spinning setup. . A high voltage of 17.8kV was attached to the needle and the solution was injected to the needle at the feed rate of 750µl/h. The needle collector distance was set at 15cm. The sample was deposited for 45 minutes at ambient temperature. The as-spun fibres deposited on FTO were dried for 1 hour at 100^{o}C in a vacuum oven. The heating rate was set at 1^{o}C/min. The dried nano-fibres were calcinated at 500^{o}C for 1 hour in a Tube furnace in Air. To reach the calcination temperature a heating rate of 3◦C/min was maintained.

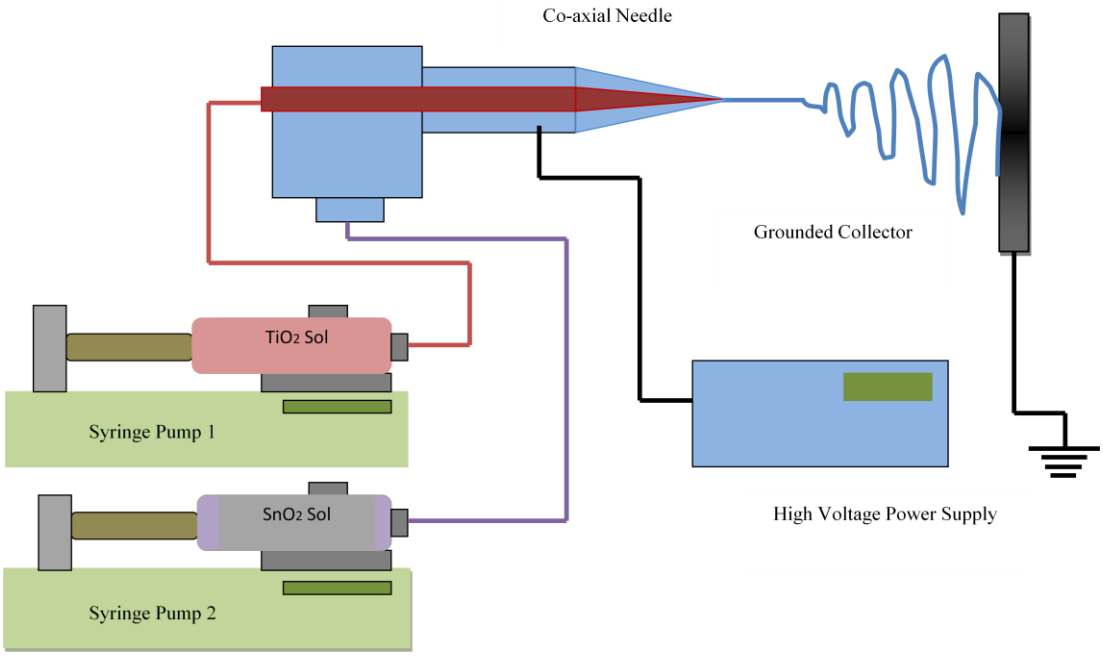

Figure 4.3 Schematic diagram of Synthesis of TiO_2/SnO_2 nano-fibres

4.1.4 Characterization of Fibres:

The structure and morphology of TiO_2 nanofiber were characterized by different techniques. The morphology was imaged by using Vega3 Tescan scanning electron microscope (SEM) and elemental composition of the samples was analysed using Energy Dispersive X-ray spectroscopy. The crystallinity was studied using D8 advanced X-Ray Diffractro-meter. The Electrical conductivity of the prepared film was measured using Hall Effect measurement system (Ecopia HMS-3000). The optical properties of the TiO_2-SnO_2 film were studied using UV-3600 plus UV-VIS NIR Spectrophotometer. Alpha (BRUKER) spectrophotometer was use to study the FTIR analysis in the range of 4000 cm-1 to 500 cm-1.

4.2 Graphene Sensitization:

The prepared TiO_2, SnO_2 and TiO_2/SnO_2 composite nano-fibres on FTO was sensitized by graphene nano-platlets. Graphene nano-platlets solution was made in which the deposited TiO_2, TiO_2/SnO_2 nano-fibres were sensitized for 24 hours followed by drying to evaporate the solvent use to dissolve graphene nano-platlets.

5mg of graphene nano-platlets were dissolved in 10 ml of DMF followed by sonication until graphene is dissolved in DMF. The TiO_2, TiO_2/SnO_2 nano-fibre deposited on FTO were dipped into the prepared solution for 24 hours followed by drying at 150^oC to completely evaporate DMF.

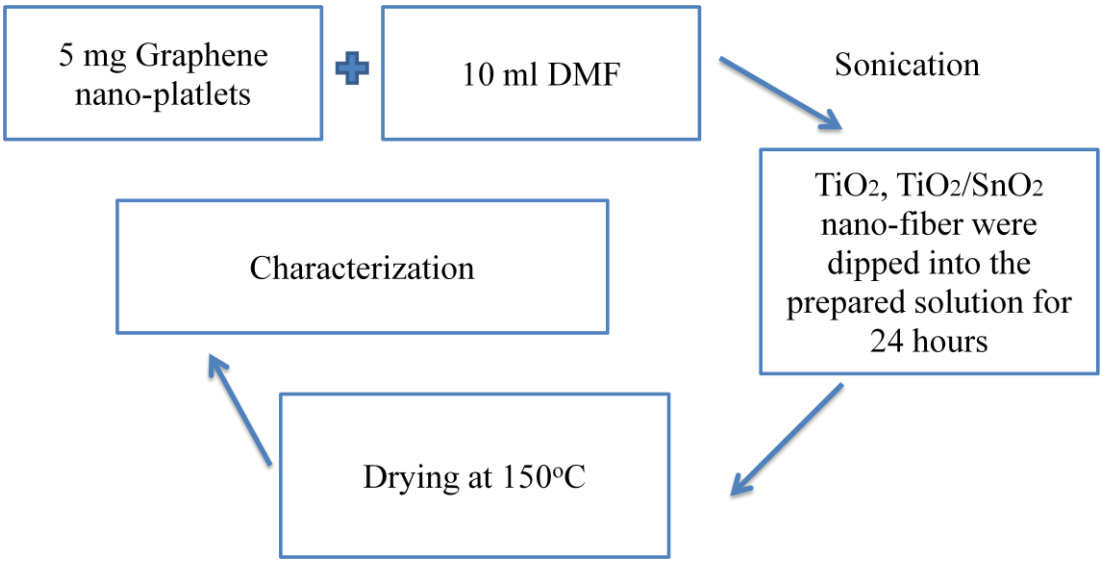

Figure 4.4 Step wise synthesis of Sensitization of nano-fibers by graphene nano-platlets

4.2.1 Characterization:

The prepared TiO_2, TiO_2/SnO_2 on FTO glass sensitized with graphene was characterized using Hall Effect measurement system (Ecopia HMS-3000) to study its electrical conductivity.

4.3 TLM Pattern a-Si Hetro-junction solar cells:

The Cells are made in the form of TLM patterns with distance between metal contacts ranging from 250nm to 8000nm as shown in figure 1. The cells were prepared by depsoition of a-Si, ITO (anti-reflective coating) and Ag(metal contacts). At first Boron- and phosphorous-doped monocrystalline CZ silicon wafers were textured in KOH an cleaned in RCA-B and Piranha to remove all the metal and organic contaminants. The wafers were then dipped in 5% HF solution to remove the native oxide layer and immediately put under vacuum for a-Si:H deposition. a-Si:H stacks were deposited using PECVD (Applied Materials P-5000). The highly doped a-Si:H n+ and p+ layer are deposited on the front and rear side of a i-Si. Gases use during PECVD for Si deposition is usually SiH_4. How-ever for the doping of the p+ and n+ to the gas following gases are mixed with SiH_4.

- p+ doping – Tri-methyl boron(TMB) and diborane(B_2H_6).
- n+ doping – phosphine (PH_3).

The gases for doping are highly diluted in H_2. For fabrication of these layers, adequate chamber cleaning procedure should be attained for better deposition of the film. The thickness of the a-S:H was varied to study its effect. Indium tin oxide (ITO) films were reactively sputtered at room temperature using an MRC 944 tool with a DC power supply using a target with a 90/10 In_2O_3/SnO_2 ratio.Followed by the deposition of Ag as metal contact. The thickness of a:Si:H and ITO films was measured using a Woollam M-2000 spectroscopic ellipsometer.

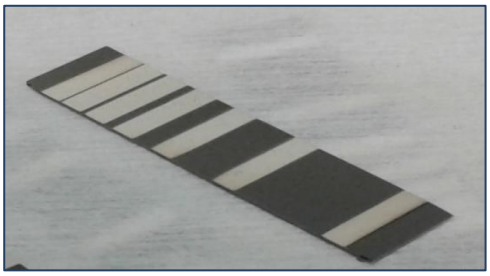

Figure 4.5 TLM patterned Cell of a-Si:H HJ solar cells

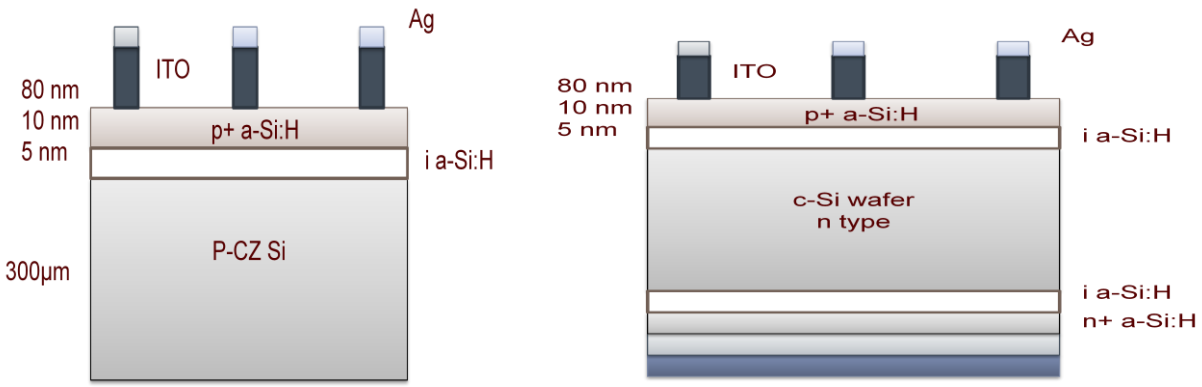

Figure 4.6 (a) Structure of a typical cell of TLM Pattern Figure 4.5 (b) Complete cell of a a-Si:H hetro-junction solar cell.

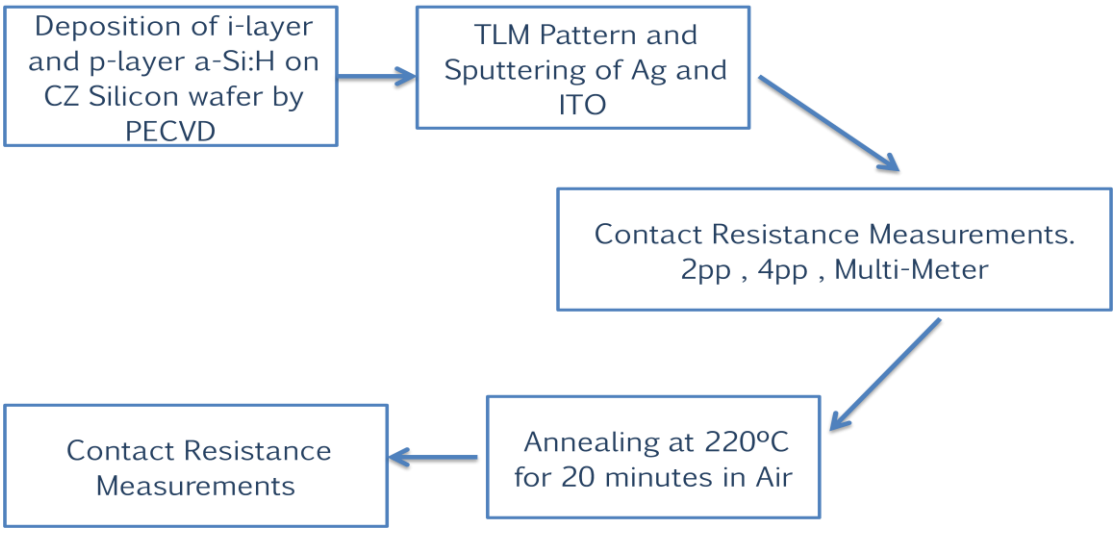

Figure 4.7 Step wise fabrication of TLM patterned a-Si:H hetro-junction solar cell.

Following samples were prepared and there electrical properties (contact Resistance) were studied using 2-probe and 4-probe measurement system.

1. 6nm thick a-Si:H layer on n-type Si and 6nm thick a-Si:H on p-type Si

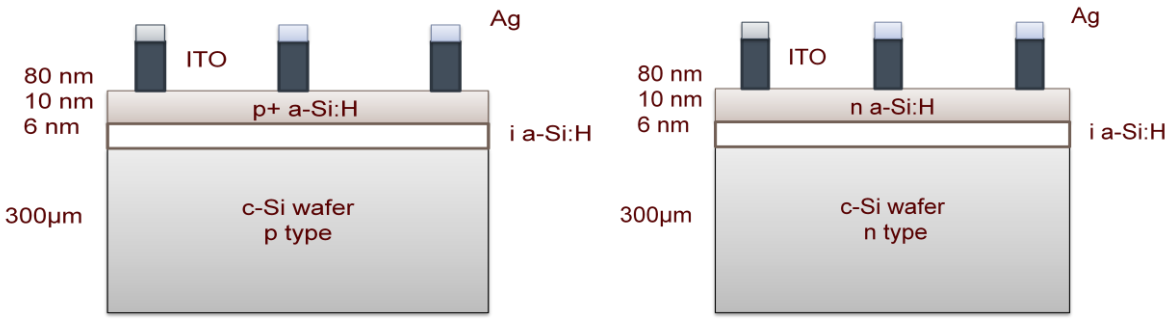

2. 4nm, 8nm, 12nm and 16nm thick a-Si:H layered cells.

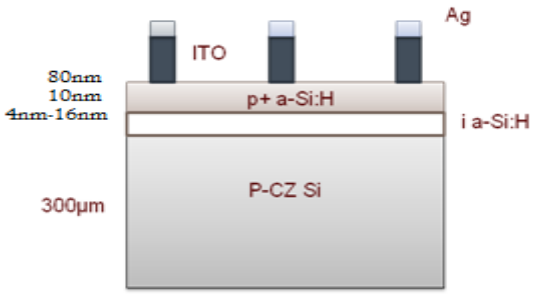

3. No a-Si:H layer and 5nm, 10nm, 20nm ,40nm thick p-type Si layer.

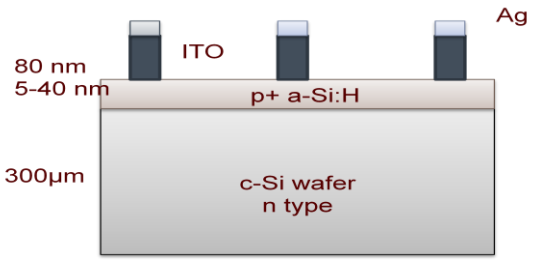

4. 4nm, 8nm, 12nm and 16nm thick a-Si:H layer cells with variable annealing temperature. Annealing temperature was varied from 150 to 250 ^{o}C.

5. Effect of varing trimethylboron (TMB) gas flow in PECVD before and after annealing.

4.4 Indium oxide RF sputtering on a-Si:

The RF sputtering of Indium oxide was carried out using R_2D_2 equipment. This equipment is use for RF sputtering of IO, ZnO and Ag. In this equipment, after placing the sample an initial pressure is maintained. This pressure was kept constant for all the depositions. Indium oxide is sputtered on a a-Si deposited on soda lime glass to achieve a thickness of 70-80nm. a-Si:H layer thickness is 6-7 nm. a-Si:H deposition was carried out in PECVD (Applied Materials P-5000). For Thickness measurements and sputtering time measurements the O_2 pressure was taken as 0.420 and Ar pressure as 10. For a-Si:H. O_2 concentration was varied to 0.220 , 0.420 , 0.620 and 0.820 to study the electrical properties.

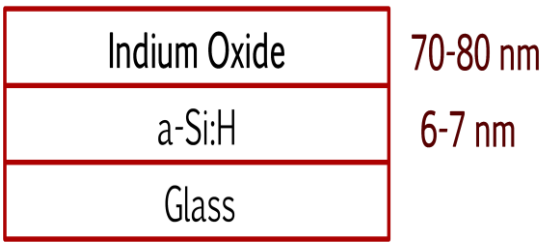

Figure 4.8 Schematic representation of indium oxide deposited on glass and a-Si:H

4.4.1 Characterization of Samples:

The samples were tested before and after annealing in air for 20 min at 220^{o}C. Hall Effect Measurement tool (Ecopia HMS-3000) was used to study the electrical properties and J.A.Woollam Ellipsometer for measuring thickness of the deposited Indium oxide layer.

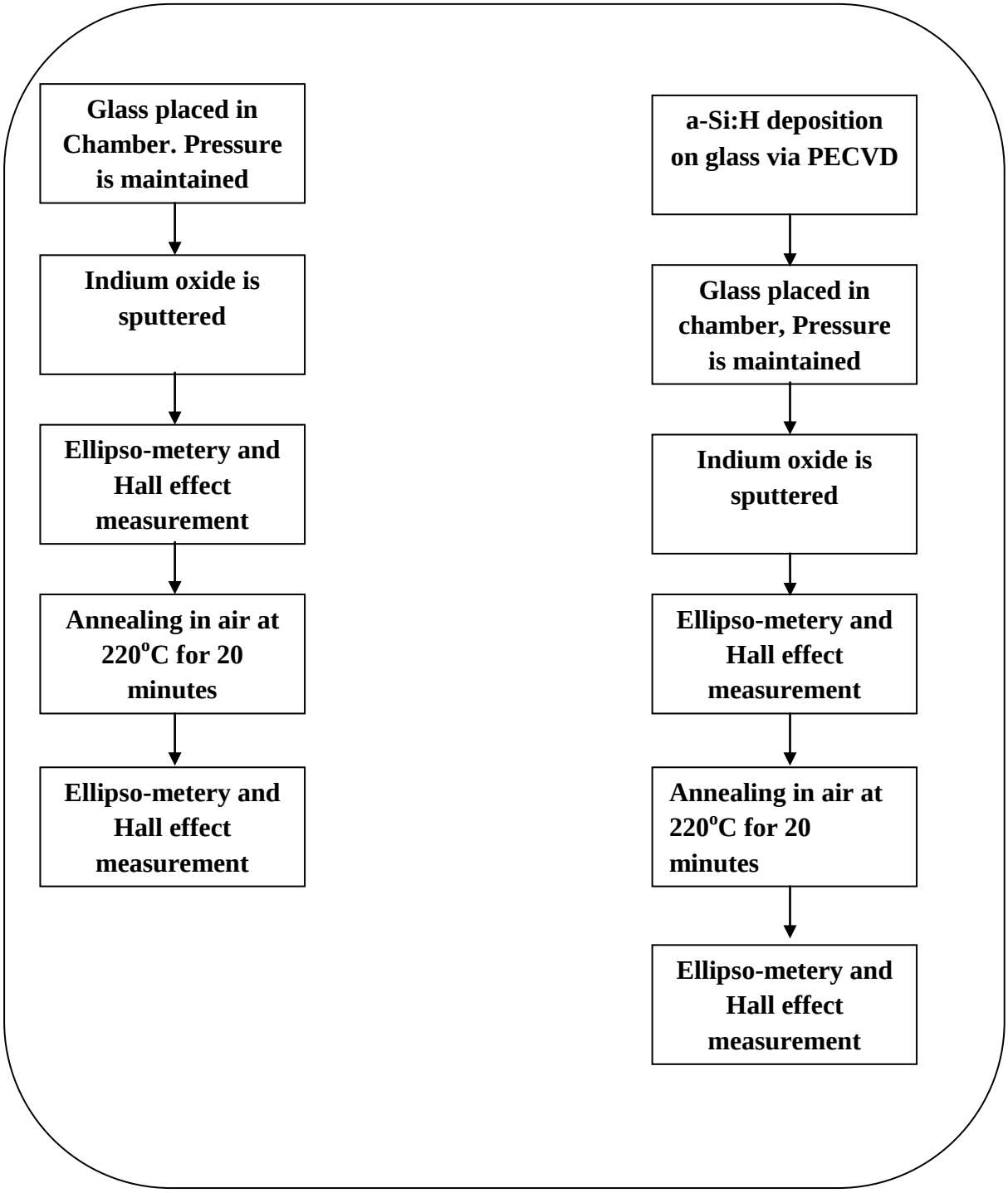

Table 4.2 Step-wise synthesis of IO on a-Si-Glass.

Summary:

This chapter explained all the experiments carried out for this research. For contact resistance measurement of a-Si hetro-junction solar cells, TLM patterns were made with variable spacing between metal contacts. Cells were made by using PECVD, while ITO and Ag were deposited by sputtering. The performance of the cell when its constituent layers are varied was studied using 2 probe and 4 probe measurement system. Similarly in case of IO as anti-reflective coating, IO was first sputtered on glass and then on a-Si by using RF sputtering tool. The thickness of IO layer and its electrical properties were studied using ellipsometer and Hall Effect measurement system respectively. The electrical, structural and optical properties of TiO2, SnO2 and TiO2/SnO2 nano-fibers were studied. The film was fabricated using solution electro-spinning and co-axial electro-spinning. The prepared fibre film is characterized by SEM, XRD, EDX and FT-IR. The electrical and optical properties of TiO2/SnO2 nano-fibres based photo-anode with graphene nano-platlets sensitization were studied. The fibers fabricated using co-axial spinning and solution spinning, were at first dipped into graphene/DMF solution for 24 hours. After graphene nano-platlets sensitization, the prepared film is tested by Hall Effect measurement system and UV-VIS spectro-photometer.

CHAPTER 5:

RESULTS AND DISCUSSIONS

5.1 Analysis of co-axial electro-spun Nano-fibres prepared using electro-spinning:

TiO_2, SnO_2 and TiO_2/SnO_2 nano-fibres were prepared using solution Electro-spinning. Composite TiO_2/SnO_2 increase the conductivity of the film for better electron transport and dye absorption when use in advance generation solar cells.

5.1.1 Crystal structure of Nano-fibres:

The crystal structure of TiO_2/SnO_2 nano-fibres, bare TiO_2 nano-fibres and bare SnO2 nano-fibres was studied using X-ray diffraction. This can determine its functionality for a variety of applications.

5.1.1.1 TiO_2 nano-fibres:

The XRD of bare TiO_2 nano-fibres is shown in figure in 2Ɵ range of 20^o to 80^o. It shows major anatase peaks as per JCPDS card number 21-1272. The 2θ at peak 25.8°

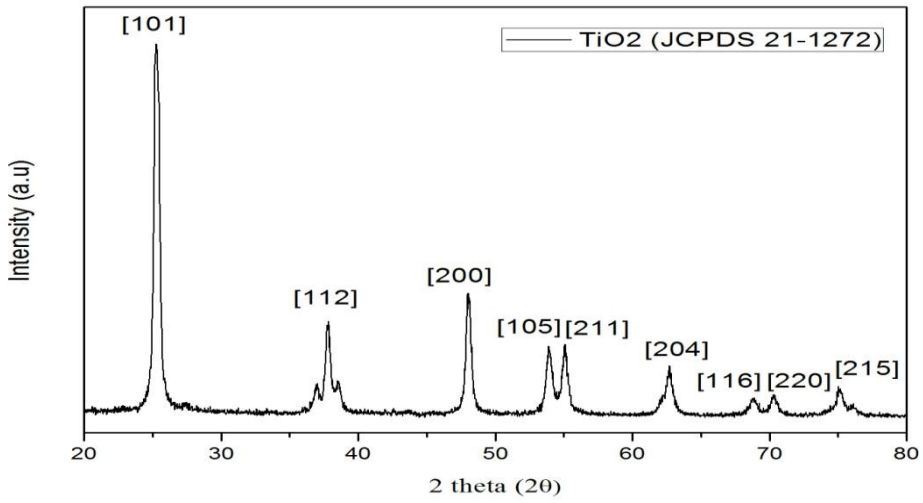

Figure 5.1 XRD Pattern of Bare TiO_2 nano-fibres (JCPDS 21-1272) prepared using Electro-spinning

confirms the TiO_2 anatase structure[1].

Strong diffraction peaks at 25.8^o and 48.01^o indicates anatase phase of TiO2. There is no unwanted/false diffraction peak found in the sample, which shows that there is no impurity in the sample. The XRD pattern of TiO_2 shows peaks at 25.8°, 37.7°, 48.01°, 53.8^o , 55.03^o& 62.10° can be assigned to [101], [112], [200], [105] , [211] & [204] planes respectively with tetragonal anatase structure. Anatase phase of TiO2 show properties like large mobility and wider optical absorption gap.

5.1.1.2 SnO_2 nano-fibres:

XRD pattern of SnO_2 nano-fibres is shown in figure. SnO_2 is present in its rutile phase. The broad diffraction peak of SnO_2 at 26.3^o shows its rutile phase. The XRD pattern in figure shows peaks at 26.3^o, 33.6^o, 52.8^o and 62.8^o can be assigned to planes of [110], [101],[211] and [310] respectively as per (JCPDS card 41-1445). Like TiO_2 nano-fibres there is no false peak present.

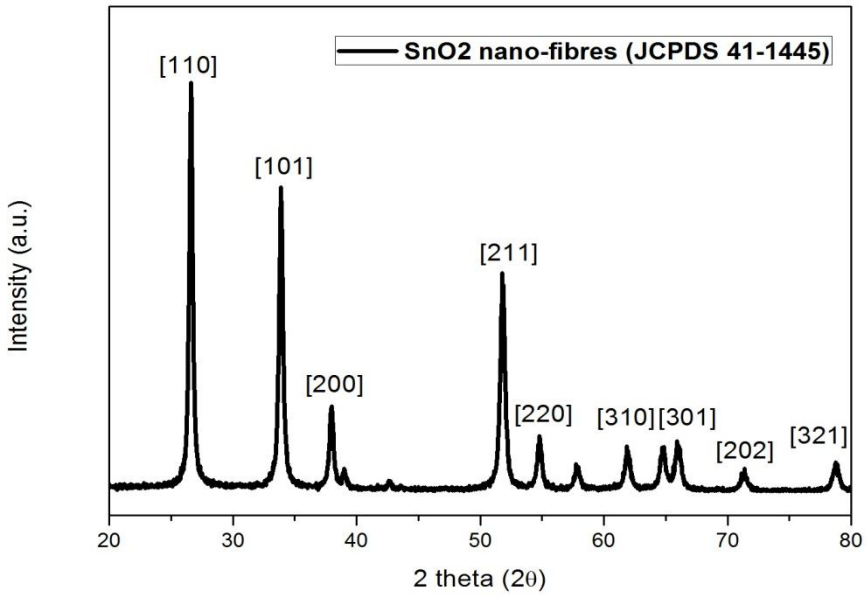

Figure 5.2 XRD Pattern of Bare SnO_2 nano-fibres (JCPDS 41-1445) prepared using Electro-spinning

5.1.1.3 TiO_2-SnO_2 co-axial electro-spun nano-fibers:

The XRD pattern of TiO_2-SnO_2 nano-fibres is shown in figure. For core-shell TiO_2/SnO_2 nano-fibres, anatase phase of TiO2 (JCPDS 41-1445) and tetragonal rutile phase of SnO_2 (JCPDS 41-1445) is present. No other impurity peak was observed and sample can be clearly indicated as nano-composite rather than an alloy[2].

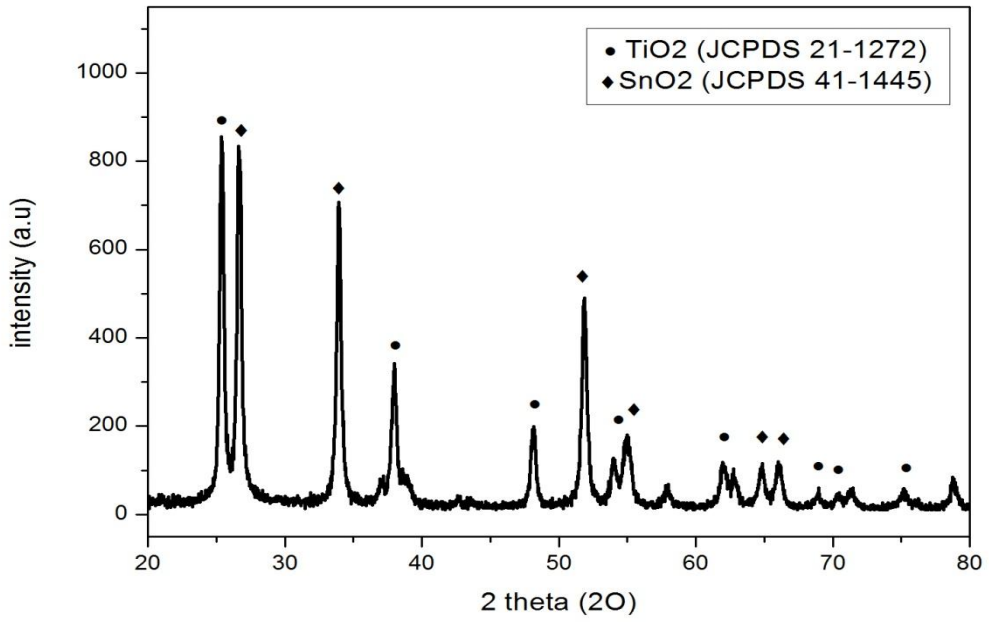

Figure 5.3 XRD Pattern of TiO_2-SnO_2 nano-fibres prepared using co-axial Electro-spinning

5.1.2 Morphology and Structure of prepared Nano-fibres:

The high resolution SEM images of Bare TiO_2, Bare SnO_2 and TiO_2/SnO_2 nano-fibres are shown in figure. Figure shows that after annealing of nano-fibres at 500^oC, the fibres are continuous but few of them are broken because of evaporation of polymer. After annealing, the surface of the fibres is rough because of the evaporation of PVP during the process of calcinations. The round like structure and circular cross section of TiO_2-SnO_2 nano-fibres in figure 5.4 (c,d) shows that core shell nano-fibres are formed. SnO_2 is the shell material and TiO_2 is the core material. As seen in the figure 5.4 (c,d) the fibers structure is similar to TiO_2 structure which

depicts that the core material is TiO_2 [5]. However EDX confirm the presence of Sn, Ti and O in the core-shell nano-fibers. Moreover, there are several bead structures which are because of the high viscosity of the precursor solution. It is reported that the factors that are involve in formation of beads include viscosity and surface tension of the precursor solution inserted in the syringe[3]. High viscosity of the solution will persuade the formation of fibres with wider diameter[4]. Variation of diameter with increase in viscosity of the solution for electro-spinning was studied for TiO_2/SnO_2 nano-fibres. The diameter of the fibres is increased by a quarter when the polymer concentration is increased to 1.8g to 2g in the solution to be electro-spun.

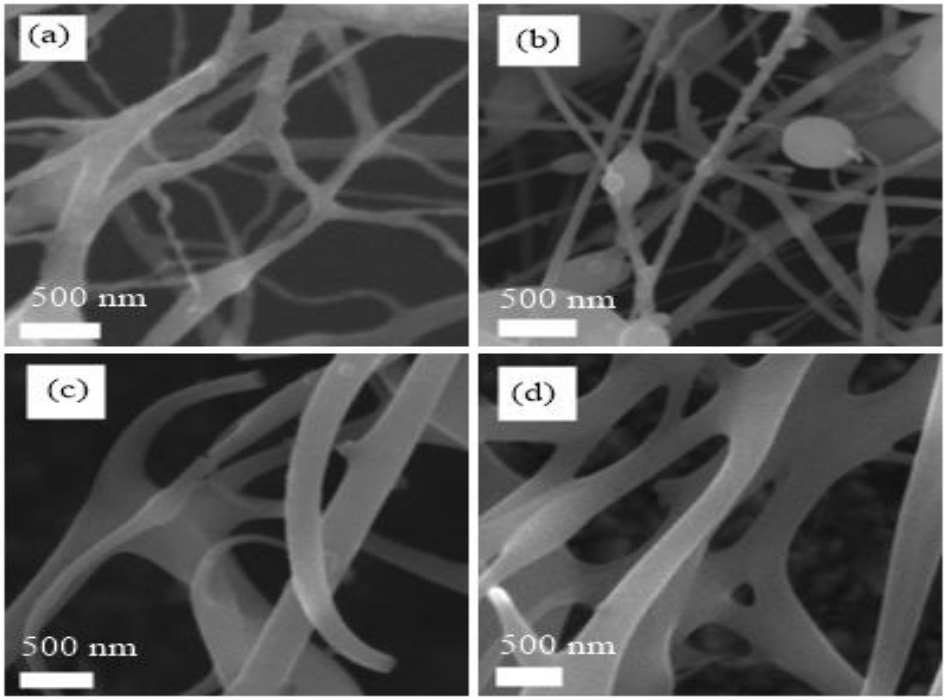

Figure 5.4 Nano-fibres annealed (a) TiO_2 nano-fibres (b) SnO_2 nano-fibres (c) TiO_2/SnO_2 nano-fibres with 1.8g of PVP (d) TiO_2/SnO_2 nano-fibres with 2g of PVP.

The average diameter for TiO_2/SnO_2 nano-fibres with precursor to polymer ratio of 1:3.8 is 40nm to 160nm while for ratio of 1:4 it increases to 80nm to 170nm. The average diameter was taken with 15 values of fibre diameter. The average diameter of the nano-fibres is less than the prepared nano-fibres before annealing. This effect is due to the evaporation of solvent and PVP after annealing. During the calcination process, the organic matters in electro spun fibres were decomposed, and then

crystallization of TiO_2 and SnO_2 take place[5]. Annealing effect was studied for bare TiO_2 nano-fibres, which shows that the diameter of the fibres decreases to half after annealing. Moreover when fibres are heated at high temperature, the fibres were tangled together and the morphology of fibres changes from fibrous to hollow structures[6]. Less diameter fibres will offer large surface area to volume ratio, which will show better dye absorption. Large the size of the nano-structure more will be the light scattering[5]. For bare TiO_2 and SnO_2 nano-fibres, the average diameter is less than 100nm. The average diameter of all the prepared nano-fibres after annealing is shown in figure

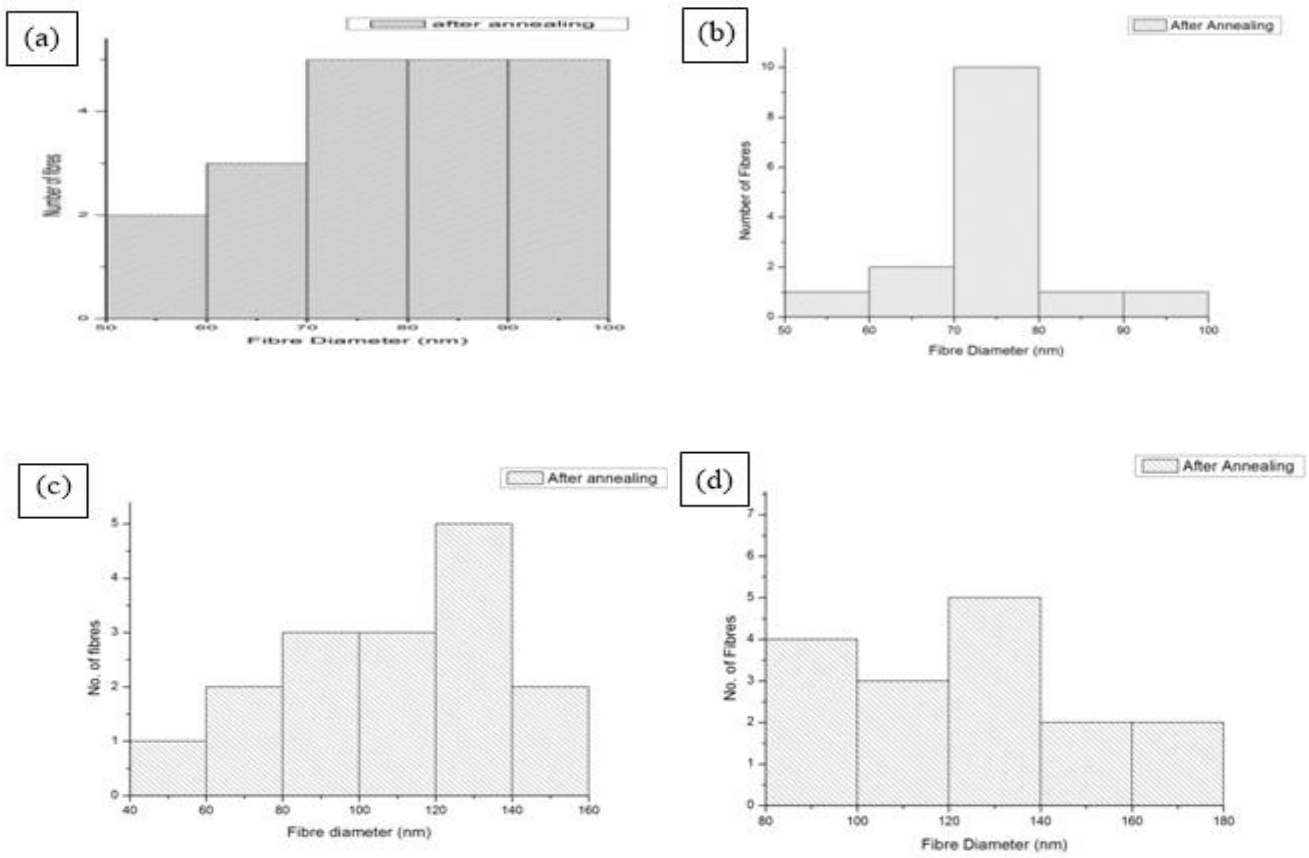

Figure 5.5 Average Diameter (a) TiO_2 nano-fibres (b) SnO_2 nano-fibres (c) TiO_2/SnO_2 nano-fibres with 1.8g PVP (d) TiO_2/SnO_2 with 2g PVP

The EDS of nano-fibres show presence of Ti, Sn and O. Amount of oxygen in high after annealing indicates that the annealing is done in air. There is no impurity present which indicates that the polymer is completely evaporated after annealing.

Sample	Atom %		
	Ti	Sn	O
TiO_2 Nano-fibres	**12.15**	**-**	**87.85**
SnO_2 Nano-fibres	**-**	**11.85**	**88.15**
TiO_2/SnO_2 nano-fibres 1.8g PVP	**7.86**	**9.22**	**82.92**
TiO_2/SnO_2 nano-fibres 2g PVP	**6.02**	**8.02**	**85.98**

Table 5.1: Summary of EDX Result

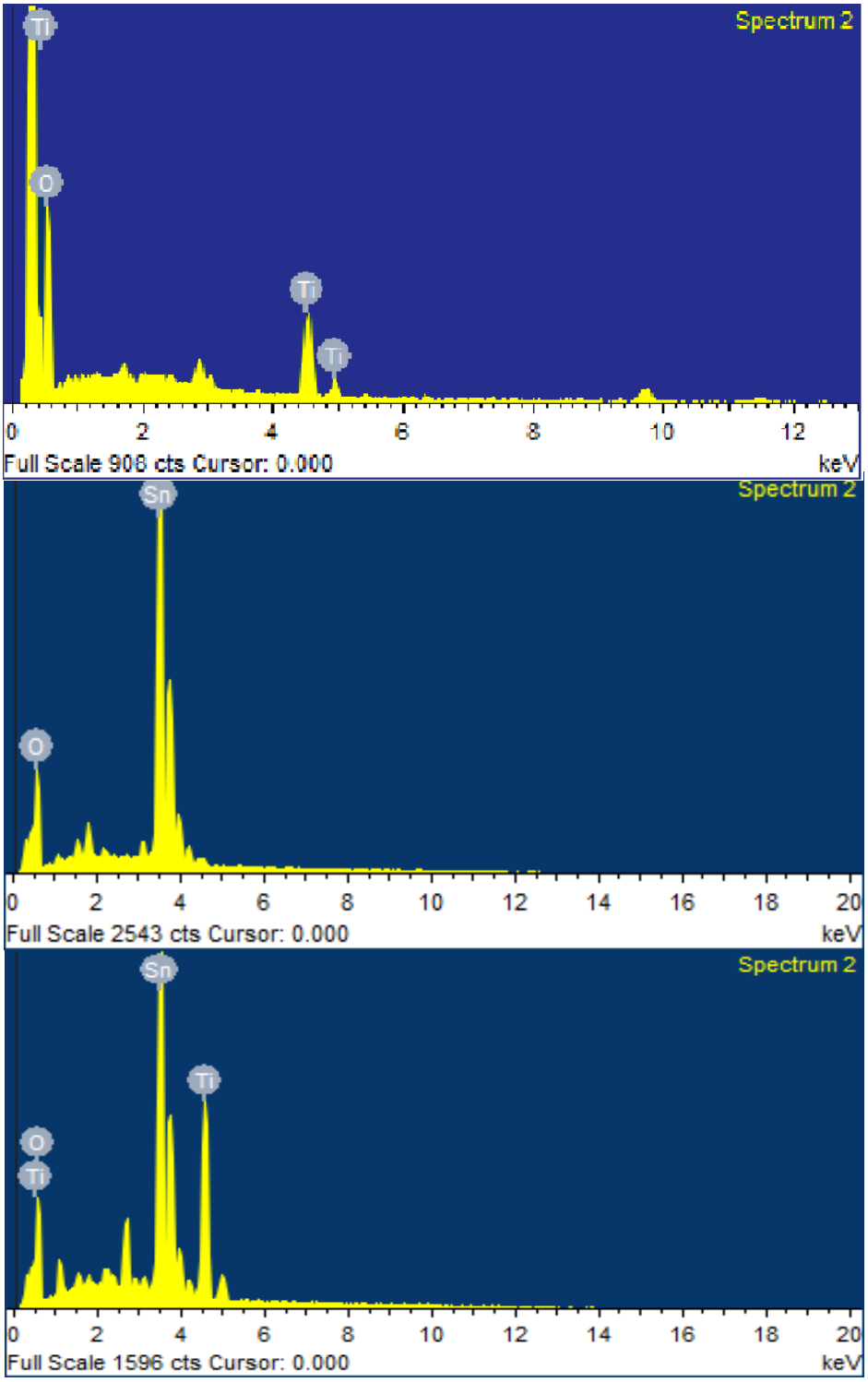

Figure 5.6 EDX Spectra of TiO_2 nano-fibres, SnO_2 nano-fibres and TiO_2/SnO_2 nano-fibres after annealing

The EDS pattern shows prominent peaks of Ti and O in case of TiO_2 nano-fibres, Sn and O in case of SnO_2 nano-fibres and Ti, Sn and O in-case of TiO_2/SnO_2 nano-fibres shown in figure 5.6. No impurities are observed.

5.1.3 FTIR Analysis of TiO_2-SnO_2 nanofibres

Figure4 show FTIR spectra of TiO_2/SnO_2 nano-fibre before and after calcination. There are several sharp peaks before annealing. These peaks are due to the polymer and solvent present before annealing. A prominent peak is seen at 1655cm^{-1} which represent the functional unit of C=O in PVP[7]. The other peak at 1277cm^{-1} represent C-N bond stretching mode. Moreover peak at around 1400cm^{-1} represent vibration of CH_2 bond of PVP. A small peak at around 1050cm^{-1} represents the vibration bend of Ti-O-C. A broad peak in between 3250cm^{-1} and 3600cm^{-1} shows the absorption of moisture and solvent during the process of electro-spinning. After annealing there is no major peak in ftir spectra. All the peaks vanish which shows that no impurity is present. The polymer and the solvent are properly evaporated after annealing[8].

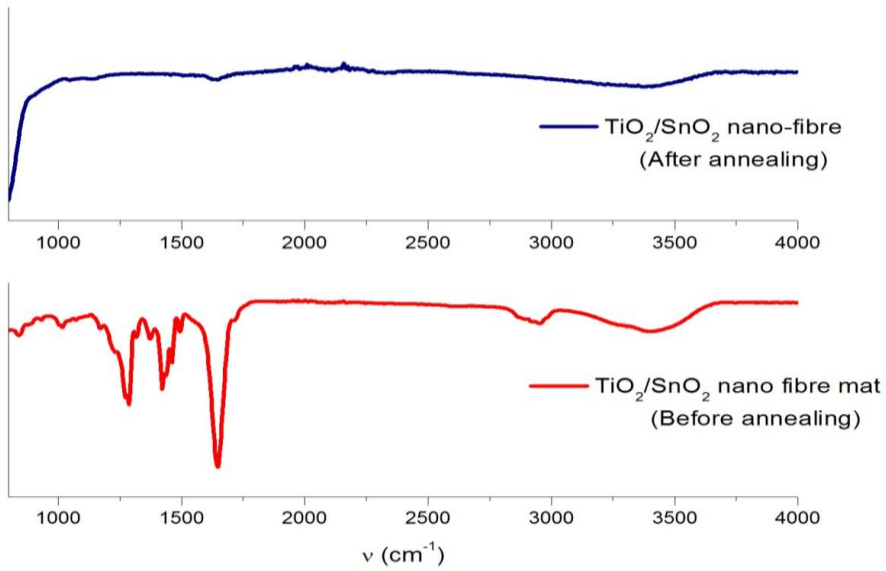

Figure 5.7 FTIR Spectra of TiO_2-SnO_2 nano-fibres (a) before annealing (b) after annealing

5.1.4 Study of optical properties of Bare TiO_2 and TiO_2-SnO_2 nano-fibres:

The optical properties were studied in wavelength range of 300nm to 800nm using UV-VIS NIR spectrophotometer. The absorption curve for the Bare TiO_2 nano-fibres and TiO_2-SnO_2 nano-fibres (Sample A) shows absorption curve in the range of 300nm to 400nm. TiO2-SnO2 nano-fibres show higher absorption then TiO_2 nano-fibres because of the in-corporation of SnO2[9]. The band-gap of the prepared materials was calculated by using tauc plot. The band-gap of TiO_2-SnO_2 increase which means increase in Fermi level and open circuit voltage for a typical DSSC solar cell. Moreover it will facilitate electron transfer from excited state of electron to the external circuit.

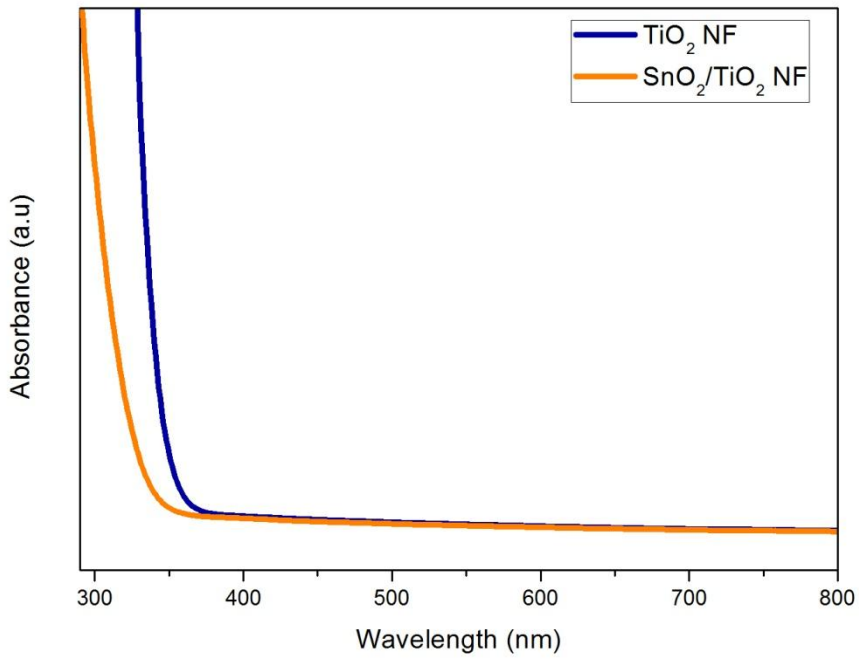

Figure 5.8 UV-Vis absorption spectra of prepared bare TiO_2 nano-fibres and TiO_2-SnO_2 nano-fibres.

5.2 Graphene Sensitization of nano-fibres:

The prepared TiO_2 nanofibres and TiO_2/SnO_2 nano-fibres are sensitized with graphene nano-platelets.

5.2.1 Crystal Structure of Graphene nano-platelets:

The crystal structure of Graphene Nano-platelets was studied using XRD. As shown in figure, the peak at 26.6^o represents the structure of graphene nano-platelets. The peak in XRD pattern of graphene nano-platelets at 26.6^o, 43.9^o and 54.2^o can be assigned to [002], [100] and [004] planes respectively. No impurity peak is observed.

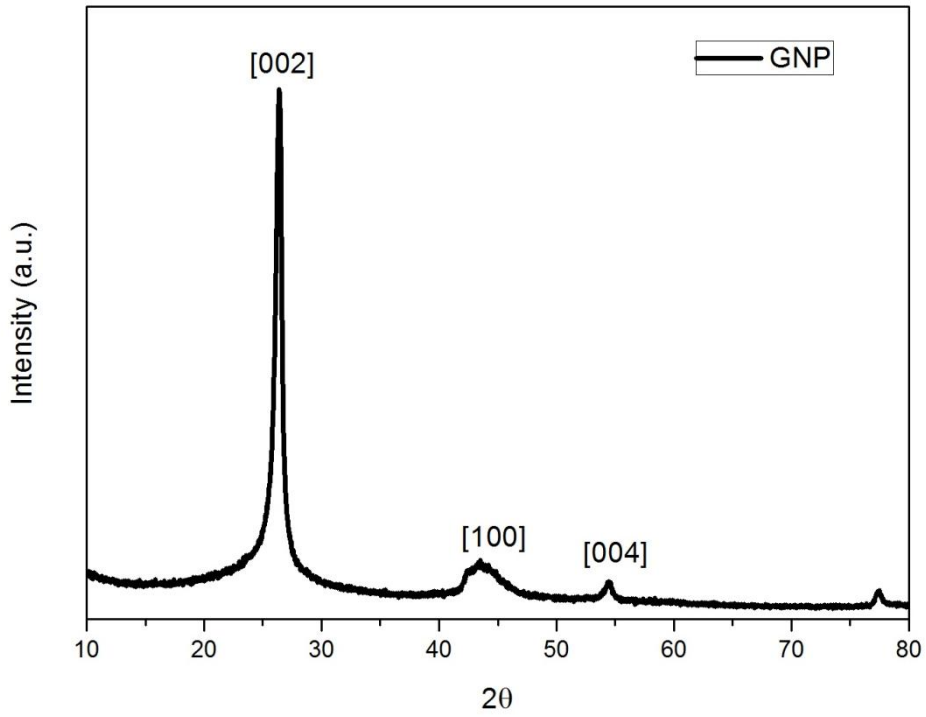

Figure 5.9 XRD pattern of Graphene nano-platelets.

5.2.2 Electrical properties of Graphene Sensitized films:

Electrical properties of TiO_2 and TiO_2-SnO_2 nano-fibres deposited on FTO were studied before and after graphene sensitization using Hall Effect measurement system. The conductivity of the film increases by addition of SnO_2 to TiO_2 nano-fibres. Addition of SnO_2 stabilizes the anatase phase of TiO_2. Similarly with addition

of SnO_2 the value of specific surface area will also increases, as a result of rise of the fibers with variable diameter. The hetro-structure of TiO_2/SnO_2 will also facilitate charge separation which results in the reduction of recombination of electron. The electron in TiO_2 will flow to SnO_2, because the work function of TiO_2 is smaller than SnO_2. This phenomenon could result in an increase of the electrons concentration in the SnO_2 layer, which results an increase in conductivity of the film. The working anode of solar cell should have high conductivity to facilitate the movement of electron from dye to the external circuit easily[10].

Sample	Before Sensitization			After Sensitization		
	Mobility M^2(V.s)	**Carrier concentration**	**Conductivity (S.m)**	**Mobility M^2(V.s)**	**Carrier concentration**	**Conductivity (S.m)**
TiO_2 nano-fibres	3.206 E+03	3.566E+13	1.831E-02	6.112E+02	9.023E+17	8.836E+01
TiO_2-SnO_2 Nano-fibres (Sample	1.175E+02	7.475E+17	1.407E+01	7.874E+03	4.861E+17	6.133E+02

A)						

Table 5.2 Electrical properties of TiO_2 nano-fibres and TiO_2-SnO_2 nano-fibres before and after graphene sensitization.

Conductivity also increases after graphene sensitization due to high conductivity of graphene nano-platelets. The conductivity, mobility and carrier concentration of TiO_2 nano-fibres, TiO_2-SnO_2 nano-fibres before and after graphene sensitization is shown in table 5.2.

5.2.3 Optical properties of Graphene sensitized films:

The optical properties were studied in wavelength range of 300nm to 700nm using UV-VIS NIR spectrophotometer. The absorption curve for TiO_2-SnO_2 nano-fibres (Sample A) shows absorption curve in the range of 300nm to 340nm. This shows that incorporation of Graphene increase the band-gap of the prepared anode.

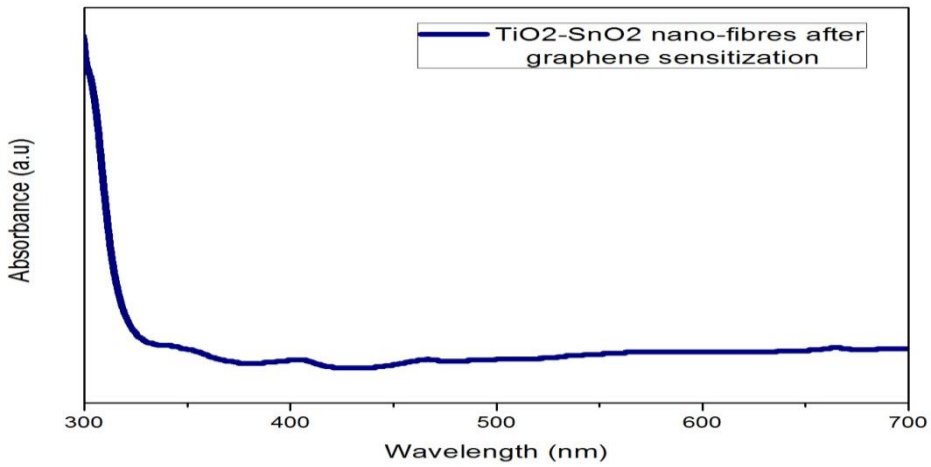

Figure 5.10 UV-VIS absorption spectra of TiO_2-SnO_2 nano-fibres after graphene sensitization

As per literature, the band-gap of dye must be higher than that of the semi-conductor anode next to it. But it shows absorption in UV region which shows that less light will be absorbed.

5.3 TLM Pattern a-Si Hetro-junction solar cells:

5.3.1 n-type and p-type doped Si on a-Si:

For a TLM structure, two cases were studied. In the first case, the stack is formed by n doped a-Si, **6nm** i-layer a-Si:H on n-Si. In the other case, the stack is formed by p doped a-Si, **6nm** i-layer a-Si:H on p-Si. The I-V measurements were done using 4-probe method for all the metal contact spacing. The objective was to measure the sheet resistance and contact resistivity. Sheet Resistance is calculated as Rs=Slope*W[11]. Where slope is value calculated by drawing a gradient line on the steepness of I-V curve and W is the width of the metal contacts. Contact Resistance is calculated by $\rho_c=R_c*LT*W$, Where Rc is contact resistance, LT is transfer length. LT*W can be treated as the effective area of the contact.

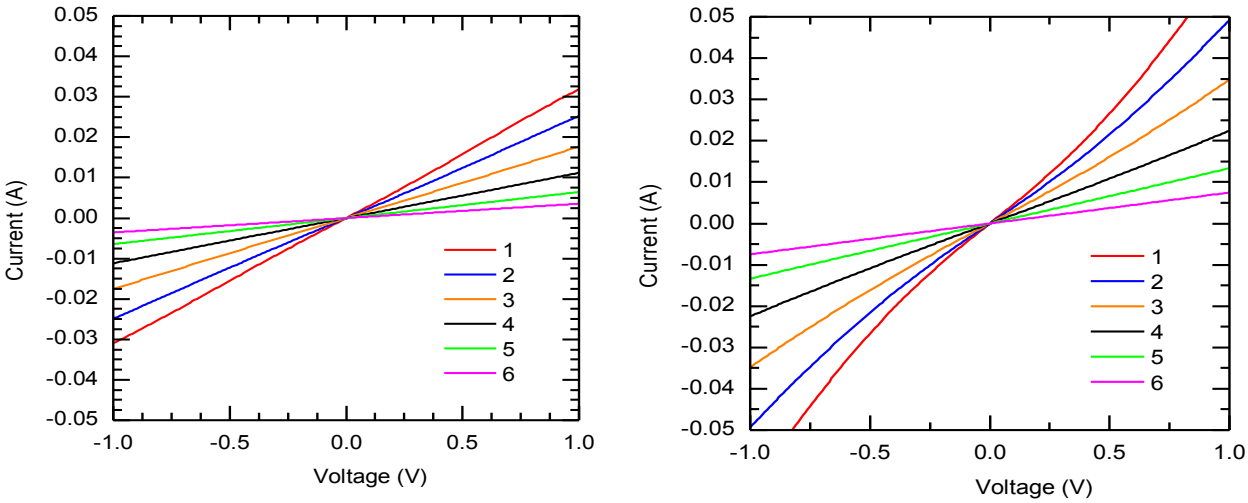

Figure 5.11 (a) I-V graph in case of n doped a-Si, 6nm **i-layer a-Si:H on n-Si where 1-6 represent spacing between the metal contacts. (b) I-V graph in case of p doped a-Si,** 6nm **i-layer a-Si:H on p-Si**

The I-V curves calculated were plotted. The sheet resistance and contact resistivity were calculated. In the first case were n doped a-Si is sputtered on n-Si, The sheet resistance is **235** Ω/sq where as contact resistivity is **0.38** Ω.cm^2. Similarly in the other case where p doped a-Si is sputtered on p-Si, the sheet resistance **140** Ω/sq where as contact resistivity is **0.32** Ω.cm^2. Which shows that in case of p doped a-Si, **6nm** i-layer a-Si:H on p-Si The sheet resistance as well as contact resistivity is low[12].

5.3.2 Effect of Spacing between the Metal Contacts on I-V curves:

A study was carried out that shows how the ohmic and schottky behavior varies with case in spacing between the metal contacts when intrinsic a-Si layer is varied from 4nm, 8nm, 12nm and 16nm using 2 probe measurements. Three different spacing between the metal contacts were studied which are 250nm, 500nm and 1000nm. This shows that schottky behavior decreases with increase in spacing between the metal contacts[13].

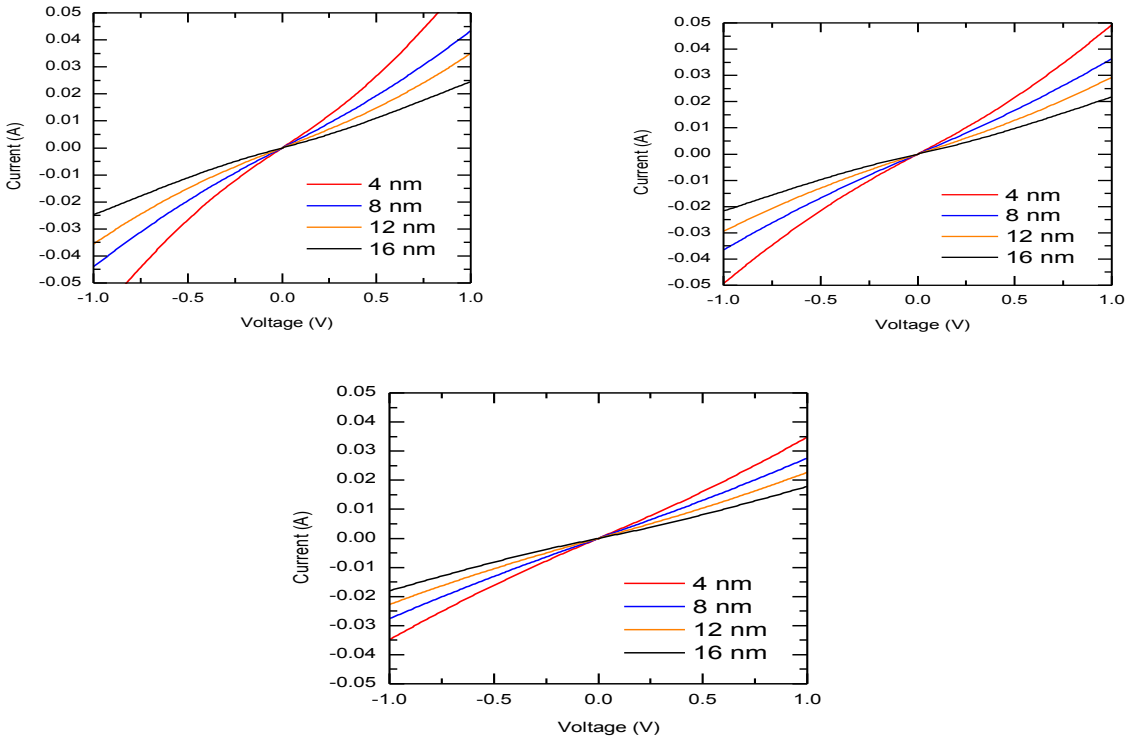

Figure 5.12 (a) Graph between current and voltage with 250nm spacing (b) Graph between current and voltage with 500nm spacing (c) Graph between current and voltage with 1000nm spacing

With increase in schottky behavior, the Voc decreases considerably resulting in decrease in cell efficiency.

5.3.3 No-i layer and varing p-layers:

In the next schematic a cell was made with no i-a-Si and different p a-Si layers thickness of a TLM pattern.

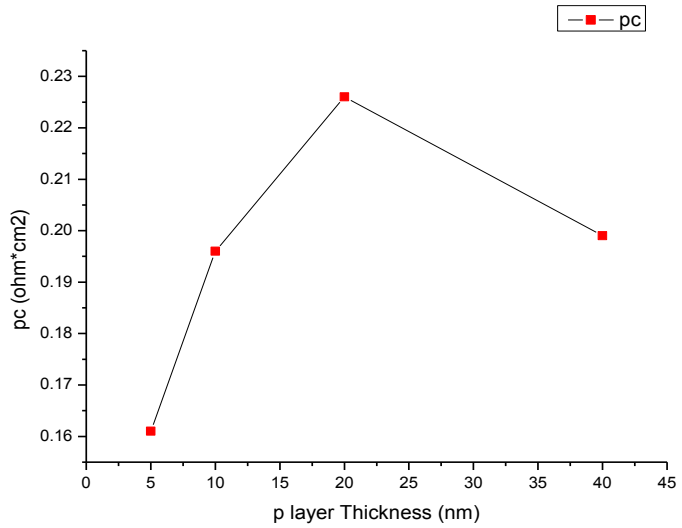

Figure 5.13 Graph between different p-layer thickness of 5nm, 10nm, 20nm and 40nm and contact resistivity.

The p a-Si:H layer act as passivation layer with result in decrease in interfacial surface defects. The Contact resistivity of the cell increases with increase in p-layer thickness. The lowest contact resistivity is for 5nm thickness of p a-Si:H of approximately 0.16 ohm*cm^2. With increase in p-layer thickness the contact resistance increases because of diffusion length. The chances of charge recombination decreases in case of less thickness of passivation layer because of lower diffusion length.

5.3.4 Effect of Annealing Temperature:

The Effect of Annealing time and annealing temperature were studied with 4 different i-layer a-Si:H thickness i.e 4nm , 8nm, 12nm and 16nm. For Annealing temperature, at 150^{o}C the contact resistivity for 4nm thickness of i-layer a-Si:H

thickness is extremely low. With increase in the temperature, the contact resistivity increase for all the thickness of i-layer a-Si:H layer. Moreover, the contact resistivity increases with the increase in i-layer a-Si:H layer thickness.

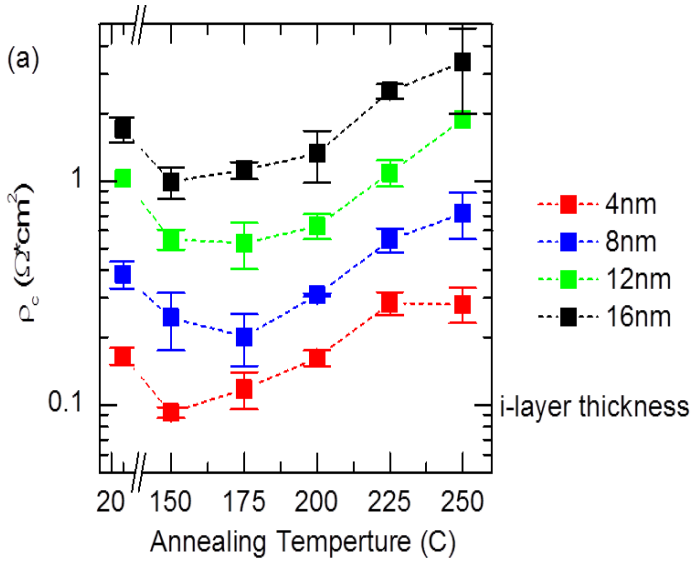

Figure 5.14 Graph between contact resistivity and annealing time for 4 different i-layer a-Si:H thickness

5.3.5 TMB Flow in PECVD chamber:

Plasma-enhanced chemical vapor deposition (PECVD) of thin film silicon is a key process in solar cells manufacturing[14]. Plasma is created within the chamber followed by a chemical reaction. The plasma is usually created by the RF (radio frequency) discharge. Several gases are used within the chamber including trimethylboron (TMB), SiH_4/H_2 and phosphine. To achieve the doping of materials these gases are mixed together. We studied the effect of contact resistivity on TMB flow before and after annealing.

In this case, the samples prepared with different TMB flows after cleaning of the chamber were annealed at 220^{o}c for 20 minutes. Due to the change in morphological

structure during the process of annealing[15], the after annealing sample with different TMB flows have low contact resistivity as compared to the other ones.

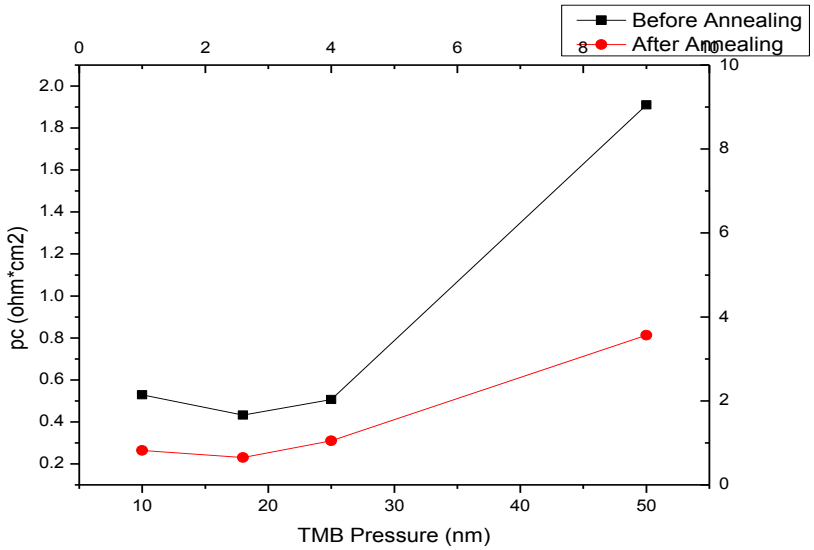

Figure 3.15 Graph between different TMB flow and contact resistivity before and after annealing.

The miniumum contact resistance was observed at 17 torr. However with increase in gas pressure, the collision of ions increases within the chamber resulting in uneven deposition on surface.

5.4 IO as TCO in a-Si:H Hetro-junction solar cells:

The required thickness was achieved on a-Si deposited on soda lime glass by carrying out multiple experiments in which sputtering time is varied keeping all other parameters like pressure, O_2 concentration and Ar concentration as constant

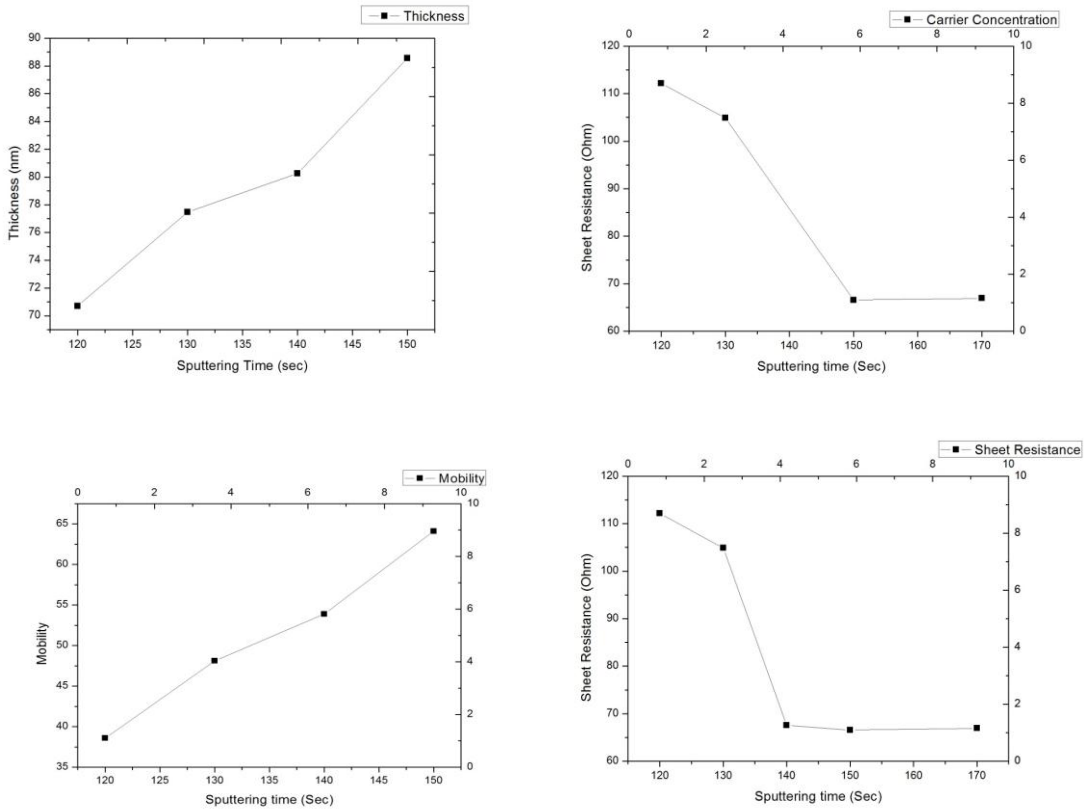

Figure 3.16 (a) graph between thickness of the deposited film and sputtering time (b) graph between carrier concentration and sputtering time (c) graph between mobility and sputtering time (d) graph between sheet resistance and sputtering time

quantities. The Electrical properties were studied using Hall Effect Measurement system. All the measurements were done after annealing at 220°C for 20 minutes.

In Figure (a) Thickness increase with increase in the time for which indium oxide is sputtered on the a-Si deposited on glass. The more the time of sputtering, more will be the thickness of the film. The Mobility also increases as shown in figure (b)

because of the movement of charges and high crystallinity, but carrier concentration decrease because the deposited film is annealed in air[16]. Carrier concentration decreases after annealing in air because of formation of more oxygen vacancies. The sheet resistance also decrease because of increase in rate of mobility [17].

Various Indium oxide transparent conductive oxide films were deposited to get required thickness of 60-80nm. Two of the samples with thickness ranging from 60 to 80nm were prepared and their spectroscopic ellipsometric data was studied. The Electrical properties were studied before and after annealing at 220°C for 20 minutes in air.

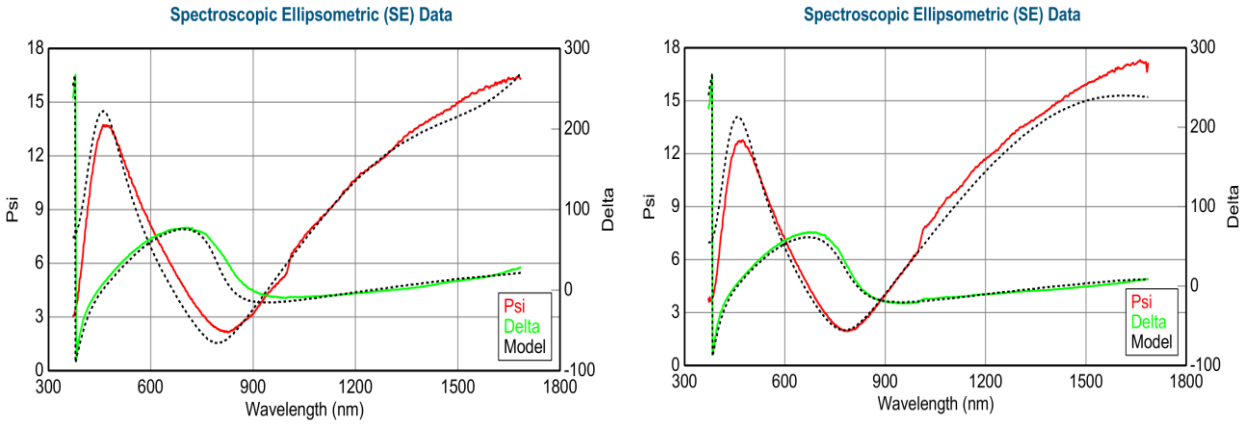

Figure 5.17 (a) Spectroscopic Ellipsometric data for sample 1 of thickness 60nm in comparsion with the model already created in ellipsometery (b) Spectroscopic Ellipsometric data for sample 2 of thickness 75.5nm in comparsion with the model already created in ellipsometer

Sample	Sputtering Time (sec)	Thickness (nm)	Before Annealing			After Annealing		
			Mobility	Carrier concentration	Rs	Mobility	Carrier Concentration	Rs
1	18	60.4	18.76	5.14E+20	54.1	56.63	2.14E+20	42.7
2	120	75.5	14.57	6.85E+20	50.1	57.26	2.17E+20	40.3

Table5.3 shows the Electrical properties of IO sputtered film with thickness of 60nm and 75nm.

The thickness of the film almost decreases to half with annealing in air [18]. The mobility increase after annealing of the film because of rapid electron movement, however the carrier concentration decreases. This effect is again due to oxygen vacancies recreated after annealing. The ellisopmetery data is in accordance with already created models. The Psi and Delta indicates the change in polarization that occurs when the measurement beam interact with the sample. These models help to calculate the predicted response from Fresnel's equations which describe each material with thickness and optical constants.

5.4.1 Effect of Increase in Oxygen Concentration:

The effect of oxygen concentration was also studied for an IO sputtered TCO on a soda lime glass.

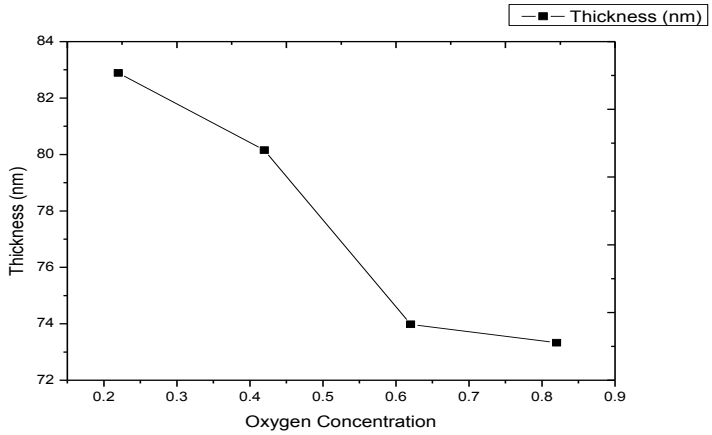

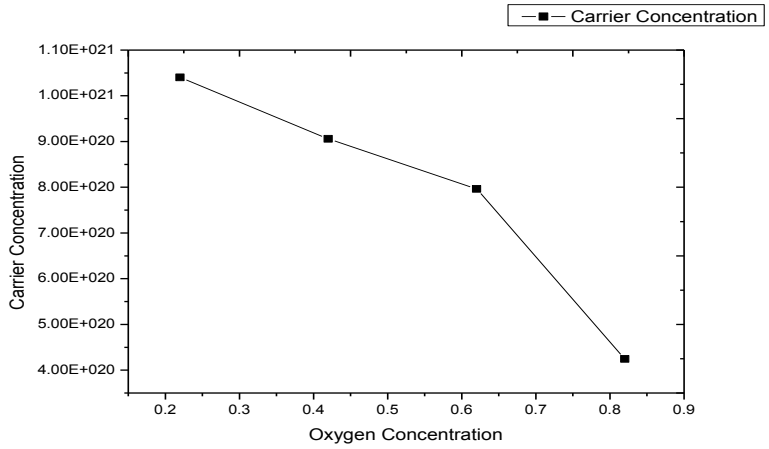

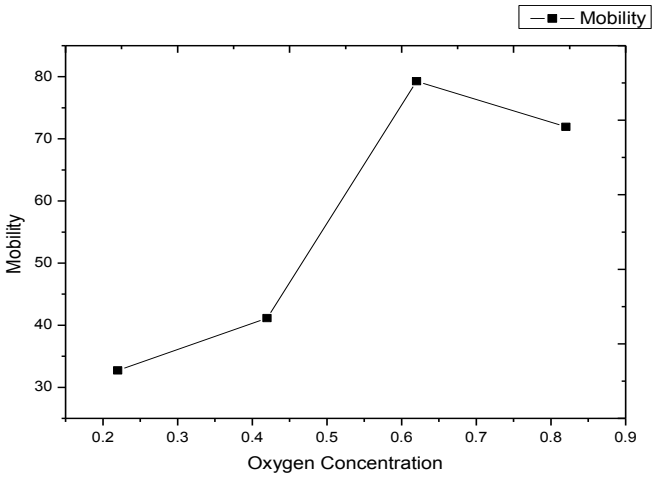

Figure 5.18 (a) graph between effect of Thickness of the film with increase in oxygen concentration (b) graph between effect of carrier concentration of the film with increase in oxygen concentration (c) graph between effect of mobility of the film with increase in oxygen concentration.

The effect of thickness, carrier concentration and mobility was studied when oxygen concentration is varied. The thickness of the film decreases with increase in oxygen concentration because increase in oxygen concentration decreases the grain size which decreases the thickness of the film[19]. The film is smoother with increases in oxygen concentration. The carrier concentration of the prepared film, decrease with increase in oxygen concentration. This effect is due to the decrease in oxygen vacancies because of incorporation of more oxygen ions[20]. The mobility of the film with increasing oxygen concentration shows a different behavior. It increase first and is maximum for 0.620% of oxygen, after which is decreases. The mobility depends on the structure of the film[21]. With increasing oxygen concentration, grain size defects are seen. The grain size increases which leads to the effect of scattering through grain boundaries a less important phenomenon. Which lead to increase in mobility. With further increase in mobility, surface defects increases. Because of more oxygen atoms ions pairs may attract additional oxygen atoms which produces electron trapping on the surface of the film. This electron trapping defect decreases the mobility of the film[22].

References

[1] M. M. . Ba-Abbad, A. A. H. . Kadhum, A. B. . Mohamad, M. S. . Takriff, and K. . Sopian, "Synthesis and catalytic activity of TiO 2 nanoparticles for photochemical oxidation of concentrated chlorophenols under direct solar radiation," *Int. J. Electrochem. Sci.*, vol. 7, no. 6, pp. 4871–4888, 2012.

[2] F. Li, X. Gao, R. Wang, T. Zhang, G. Lu, and N. Barsan, "Design of Core-Shell Heterostructure Nanofibers with Different Work Function and Their Sensing Properties to Trimethylamine," *ACS Appl. Mater. Interfaces*, vol. 8, no. 30, pp. 19799–19806, 2016.

[3] D. Y. Lee, B. Kim, S. Lee, M. Lee, and J. Lee, "Titania Nanofibers Prepared by Electrospinning," vol. 48, no. June 2006, pp. 1686–1690, 2006.

[4] M.-J. Jeng, Y.-L. Wung, L.-B. Chang, and L. Chow, "Particle Size Effects of TiO $_2$ Layers on the Solar Efficiency of Dye-Sensitized Solar Cells," *Int. J. Photoenergy*, vol. 2013, pp. 1–9, 2013.

[5] W. Nuansing, S. Ninmuang, W. Jarernboon, S. Maensiri, and S. Seraphin, "Structural characterization and morphology of electrospun TiO2 nanofibers," *Mater. Sci. Eng. B Solid-State Mater. Adv. Technol.*, vol. 131, no. 1–3, pp. 147–155, 2006.

[6] a Kumar, R. Jose, K. Fujihara, J. Wang, and S. Ramakrishna, "Structural and Optical Properties of Electrospun TiO 2 Nanofibers," *Chem. Mater.*, vol. 19, no. 26, pp. 6536–6542, 2007.

[7] N. Soltani *et al.*, "Influence of the polyvinyl pyrrolidone concentration on particle size and dispersion of ZnS nanoparticles synthesized by microwave irradiation," *Int. J. Mol. Sci.*, vol. 13, no. 10, pp. 12412–12427, 2012.

[8] M. Wang, Y. Song, M. Wang, X. Zhang, J. Wu, and T. Zhang, "Investigation on the role of the molecular weight of polyvinyl pyrrolidone in the shape

control of high-yield silver nanospheres and ... Investigation on the role of the molecular weight of polyvinyl pyrrolidone in the shape control of high-yield silver n," no. November, pp. 1–8, 2014.

[9] I. M. A. Mohamed, V. D. Dao, A. S. Yasin, H. S. Choi, K. A. Khalil, and N. A. M. Barakat, "Facile synthesis of GO@SnO2/TiO2 nanofibers and their behavior in photovoltaics," *J. Colloid Interface Sci.*, vol. 490, pp. 303–313, 2017.

[10] J. Gong, J. Liang, and K. Sumathy, "Review on dye-sensitized solar cells (DSSCs): Fundamental concepts and novel materials," *Renew. Sustain. Energy Rev.*, vol. 16, no. 8, pp. 5848–5860, 2012.

[11] U. Wurfel, A. Cuevas, and P. Wurfel, "Charge carrier separation in solar cells," *IEEE J. Photovoltaics*, vol. 5, no. 1, pp. 461–469, 2015.

[12] J. Bullock, A. Cuevas, T. Allen, and C. Battaglia, "Molybdenum oxide MoOx: A versatile hole contact for silicon solar cells," *Appl. Phys. Lett.*, vol. 105, no. 23, 2014.

[13] G. Nogay *et al.*, "Microcrystalline Silicon Carrier Collectors for Silicon Heterojunction Solar Cells and Impact on Low-Temperature Device Characteristics," vol. 6, no. i, pp. 2–4, 2002.

[14] O. Gabriel, S. Kirner, M. Klick, B. Stannowski, and R. Schlatmann, "Plasma monitoring and PECVD process control in thin film silicon-based solar cell manufacturing," *EPJ Photovoltaics*, vol. 5, p. 55202, 2014.

[15] J. Wu *et al.*, "Effect of post-annealing treatment on the contact resistance of small molecule solar cells," pp. 2780–2784, 2011.

[16] K. Sreenivas, T. Sudersena Rao, A. Mansingh, and S. Chandra, "Preparation and characterization of rf sputtered indium tin oxide films," *J. Appl. Phys.*, vol. 57, no. 2, pp. 384–392, 1985.

[17] J. R. Bellingham, P. W.A., and C. . Adkins, "Electrical and optical properties of amorphous indium oxide," *J. Pphys. Condens. Matter*, vol. 2, no. 6207–6221, 1990.

[18] Y. Shigesato, S. Takaki, and T. Haranoh, “Electrical and structural properties of low resistivity tin-doped indium oxide films,” *J. Appl. Phys.*, vol. 71, no. 7, pp. 3356–3364, 1992.

[19] M. Buchanan, J. B. Webb, and D. F. Williams, “Preparation of conducting and transparent thin films of tin-doped indium oxide by magnetron sputtering,” *Appl. Phys. Lett.*, vol. 37, no. 2, pp. 213–215, 1980.

[20] W.-F. Wu and B.-S. Chiou, “Effect of oxygen concentration in the sputtering ambient on the microstructure, electrical and optical properties of radio-frequency magnetron-sputtered indium tin oxide films,” *Semicond. Sci. Technol.*, vol. 11, no. 2, pp. 196–202, 1999.

[21] N. Kikuchi, E. Kusano, E. Kishio, A. Kinbara, and H. Nanto, “Effects of excess oxygen introduced during sputter deposition on carrier mobility in as-deposited and postannealed indium–tin–oxide films,” *J. Vac. Sci. Technol. A Vacuum, Surfaces, Film.*, vol. 19, no. 4, p. 1636, 2001.

[22] M. A. Martlnez, “Post-deposition annealing effects in RF reactive magnetron sputtered indium tin oxide thin films,” vol. 26, pp. 309–321, 1992.

CHAPTER 6:

CONCLUSION AND FUTURE RECOMMENDATION:

6.1 Conclusion:

6.1.1 Nano-fibres Based photo-anode:

1. TiO_2 nano-fibres, SnO_2 nano-fibres were successfully synthesized by PVP as a polymer using Electro-spinning. SEM, XRD and EDX confirm the formation of TiO_2 and SnO_2 nano-fibres. The fiber diameter was in the range of 50nm to 100nm.
2. TiO_2-SnO_2 nano-fibres were synthesized using co-axial Electro-spinning. Both the solution was inserted via same syringe. XRD, SEM, EDX, UV-VIS and FTIR confirm the formation of nano-fibres. The fiber diameter was in the range of 40nm to 160nm. The fiber diameter increases with increase in the polymer concentration by about a quarter.
3. Electrical properties studied via Hall Effect measurement system confirm that the conductivity of the prepared film increase after addition of SnO_2 nano-fibres to TiO_2 nano-fibres. The conductivity of film by addition of SnO_2 to TiO_2 nano-fibers increases the conductivity to around 3 times then TiO_2 nano-fibers.
4. Prepared TiO_2 nano-fibres and TiO_2-SnO_2 nano-fibres were successfully sensitized by Graphene nano-platelets using DMF as a solvent.
5. Conductivity of the sensitized films was studied, which shows that sensitization increase the conductivity of the film. The conductivity after sensitization increases twice the un-sensitized nano-fibers. Moreover, the band-gap of the film also increases after sensitization.

6.1.2 TLM Pattern a-Si Hetro-junction solar cells:

TLM pattern with various i-layer, p-layer, Ag and TCO layer were successfully prepared using PECVD and sputtering. The spacing between the metal contacts was varied using laser patterns. Following conclusions were depicted by various conditions,

- Two cases were studied, one with n doped a-Si is sputtered on i-layer a-Si and in other case p doped a-Si is sputtered on i layer a-Si. The results illustrate that in case of p doped a-Si, **6nm** i-layer a-Si:H on p-Si The sheet resistance as well as contact resistivity is low.
- By increasing the spacing between metal contacts the schottky behaviour increase and the contacts become more ohmic. With increase in schottky behavior, the Voc decreases considerably resulting in decrease in cell efficiency.
- With no i-layer and various p-layer thicknesses, contact resistance increases because of diffusion length. The minimum contact resistance is for 5 nm thickness of p-layer.
- The effect of annealing temperature was also studied. More the thickness of i-layer, more is the contact resistance. Highest contact resistance is for 16 nm thick i-layer in order of $1\Omega*cm^3$.
- With increase in annealing temperature the contact resistivity increase. From these results, suitable temperature for the annealing of these cells is considered to be 170ºC.
- The TMB gas flow within the PECVD chamber was also varied and its effect was studied on contact resistance of the cells. Gas flow of 18 sccm gives the lowest contact resistance, while annealing decreases the contact resistance. The miniumum contact resistance after annealing was observed at 17 torr.

6.1.3 Indium oxide RF sputtering on a-Si:

1. Indium oxide was successfully deposited on a-Si—Glass using RF sputtering (in presence of Ar and O_2).
2. With increase in sputtering time from 120 seconds to 150 seconds, the thickness of the film and mobility increases but sheet resistance and carrier concentration decreases. Mobility increases because of the movement of charges and high crystallinity. Moreover carrier concentration decreases after annealing in air because of formation of more oxygen vacancies. The sheet resistance also decrease because of increase in rate of mobility.
3. Samples of TCO thickness of 60nm to 75nm were successfully prepared. Thickness of the prepared film was confirmed using Ellipsometry.
4. The effect of change in oxygen concentration was studied. The thickness of the film, carrier concentration decreases while the mobility increases with increase in oxygen concentration. Thickness and mobility are partially affected by the grain size. However, carrier concentration reduces due to decrease in oxygen vacancies.

6.2 Future Recommendation:

1. Study of effect of various Electro-spinning parameters on TiO_2-SnO_2 nano-fibres. These parameters include voltage, feed-rate, distance between needle and collector and molecular weight of polymer used.

2. To prepare various metal oxides composite nano-fibres based materials and study their electrical properties.

3. Study the properties of other nano-structure based TiO_2-SnO_2 with graphene sensitization.

4. Using other graphene based materials as dye, including graphene oxide, reduced graphene oxide.

5. Study of I-V characteristics of TiO_2-SnO_2 nano-fibres with graphene sensitization.

6. Effect on series resistance under illumination when layer of a-Si Hetro-junction solar cell are varied.

7. Effect on Series Resistance when IO is used as an Anti-Reflective coating in a cell.

8. Comparison of Properties of IO and IZO used as Anti-Reflective Coatings.

Dedicated to

my Mother

for her love, support and encouragement

Acknowledgements:

All praise to the great **Allah Almighty** who has bestowed me with the opportunity to seek knowledge and enabled me to fulfill the obligation to explore the world of science up to my maximum limits.

I would like to express my sincere gratitude to my **research supervisor Dr. Zuhair S. Khan** for his motivation, continuous support, patience and immense knowledge. He has guided me completely through-out my research work. Working under his supervision has indeed broadened my vision.

I am also thank-full to Dr. Zachary Holman for his guidance and support during my research exchange to ASU, Arizona. He not only facilitates me but also provide me to avail all the required trainings and guidance for the assigned projects. I would like to pay my sincere appreciation to my mentors Mehdi Leilaeioun and Will Weigand.

I am also really thankful to my GEC members, Dr Nadia Shahzad, Dr Pervez Akhtar, and Dr. Sofia for sparing precious time from their busy schedules, for suggestions as well as moral support. I am indeed indebted to Dr. Nadia Shahzad for her unlimited support, valuable advice and guidance in my research work. Besides this I would like to thank the USPCASE faculty for being extremely cooperative especially Sir Asghar Ali, Sir Amir Satti, Sir Naveed Ahmed, Sir Qamar-ud-din and Miss Anam Qadir. I would like to pay sincere thankfulness to Dr. Muhammad Rafi from NILOP for all the enthusiasm and guidance.

A special thanks to my group members at advance energy materials lab including Humaira Asghar, Hina Pervaiz, Maria Batool, Maria Sattar, Ussama Khalid Barki and Awais Mehboob.

Last but not the least, I would pay my regards to my mother and sister for their un-parallel love and encouragement throughout my research work.

Presented at 3rd Conference on Emerging Materials and Processes (Nov 13-14 CEMP 2017) Conference held at the SCME, NUST, Islamabad.

Annexure I

Synthesis and characterization of TiO_2 nano-fibres on FTO glass via Electro-spinning

Maham Akhlaq[1*], Hina Pervaiz[1], Dr. Zuhair S.Khan[1]

[1] US Pakistan Center for Advanced Studies in Energy (USPCAS-E), National University of Science and Technology (NUST), H-12 Islamabad.

* **Corresponding author:** Maham Akhlaq **Postal Address:** 22 A/2 Gulberg 3 Lahore **Email Address:** 15esemaham@uspcase.nust.edu.pk **Contact Number:** +92332-4236481

Abstract:

Nano-fibres are an emerging type of nano-structures that can be use in solar cells owning to their porous structure and outstanding electrical and optical properties. Electro-spinning has been considered as a simple and efficient method for producing polycrystalline nano-fibres from a rich variety of materials including metal oxides and polymers with diameter ranging from 50nm to 500nm. Metal oxides including TiO2 gives excellent properties as nano-fibres like large surface area of fibres which give tremendous applications in solar cells. In this paper, we have fabricated and characterized TiO2 nano-fibres for photo-anode applications using poly-vinyl-pyrrolidone (PVP) polymer using Le-10 Bioinicia Electro-spinning setup and studied its optical properties. The morphology of the as-spun fibres was studied. The nano-fibres were collected using Electro-spinning on a FTO glass attached on the grounded collector followed by calcinations at 450˚C. These calcinated nanofibers are characterized by X-ray diffraction, Scanning Electron Microscopy (SEM) and UV-Vis Spectroscopy to study the structural and optical properties of the nano-fibres.

Keywords: Electro-spinning, TiO_2, FTO Glass.

1. Introduction:

Nano-materials have recently engrossed a substantial amount of attention due to their exceptional electrical, physical, chemical, and magnetic properties. Among few major types of Nano-Materials, Nano-Fiber is an important one-dimensional nano-material that can be used in various filtration techniques and as an Anode in solar cells and Lithium Ion batteries, etc. Nano-fibers are highly engineered fibers with a diameter of 50nm to 500nm. They are best known for their low density, large specific surface area, small fibre diameter, high porosity, small pore size and possibility to incorporate certain additives. There are numerous methods for preparation of Nano-fibers including electrospinning and spinning bi-component fibers. However, the electro spinning method is the most familiar one in industry as well as laboratory[1]. Electro-spinning is an uncomplicated and systematic method for producing polycrystalline nano-fibres from a large variety of materials including oxides and polymers [2]. Electro spinning is a process that spins fibers of diameters ranging from 10nm to several hundred

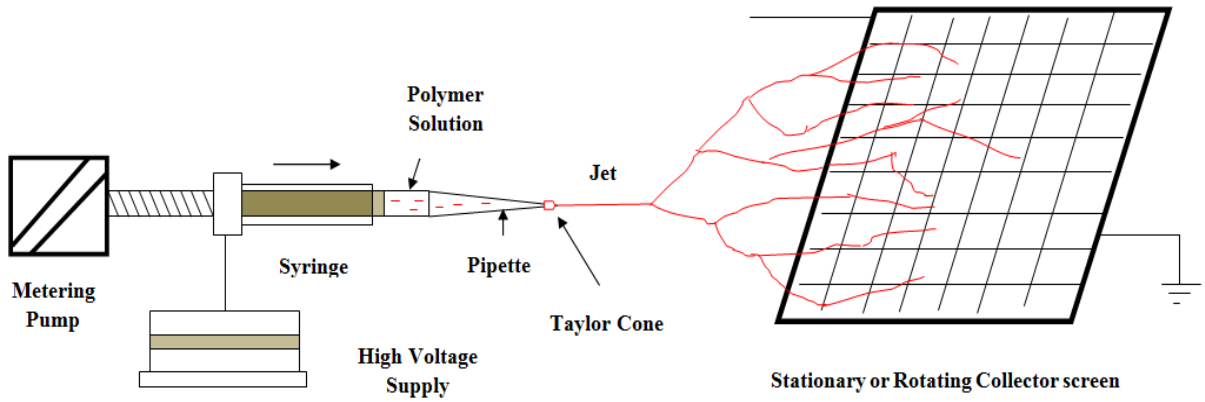

Figure 4: Schematic diagram of the Electro spinning setup. The jet of fibres is collected on the flat plate collector attached in front of the needle.

nano-meters by formation and stretching/elongation of an electrified polymer fluid jet [3]. A typical Laboratory setup of electro spinning consists of a syringe containing the polymer solution, connected to a high-voltage, a syringe pump and a collector. The liquid in the syringe is extruded from the needle tip at a rate set by a syringe pump attached to it. With sufficiently high voltage the body of the droplet become charged and due to electro static repulsion it is stretched and is erupted from the needle, jet form on the needle or the Taylor cone create charged liquid jet that is collected on the collector plate. The collector varies from a flat plate to a rotating drum (with variable sizes).

Metal oxides like TiO2, SnO2 and ZnO nano-fibres have shown marvellous efficiency when used in advanced generation solar cells owning to their wider band-gap, large surface area to volume ratio and porous structure. Titanium dioxide (TiO2) being an efficient metal oxide because it is low cost, exceptional optical properties and electrical properties, superior chemical stability [4] can be an excellent choice for use in advanced generation solar cells. Titanium (IV) oxide exists in nature in three forms, rutile, anatase and brookite. Anatase appears to be more dynamic of the two phases[5]. Anatase TiO2 nano-fibres have received much interest recently[6] owing to their potential application in photo-catalysis [7] and dye-sensitized solar cells (DSSC)[8]. TiO2 nano-fibres offer faster electron transportation rate, high porosity and larger surface area to volume ratio [9]. In this paper we have grown TiO2 nano-fibres on FTO glass for their use as anode material for advance generation solar cells and studied its morphology and optical properties.

2. Experimental

Titanium iso-propoxide, absolute ethanol, Glacial acetic acid and, Poly-vinyl-pyrrolidone (PVP,Mw= 3,000,000 g·mol−1) were purchased from Sigma Aldrich. Solution of Ethanol and Glacial acetic acid was made in a ratio of 4:1, followed by stirring for 10 minutes. 1.8g PVP was added to the above solution to get a viscous polymer solution. After stirring the polymer solution for 1 hour, a small amount of Titanium iso-propoxide was added to the solution. The colour of the solution changes to light yellowish. The solution was stirred until a homogenous mixture is obtained.

This highly viscous polymeric solution was inserted into a 5ml syringe in a horizontally attached electro-spinning setup.

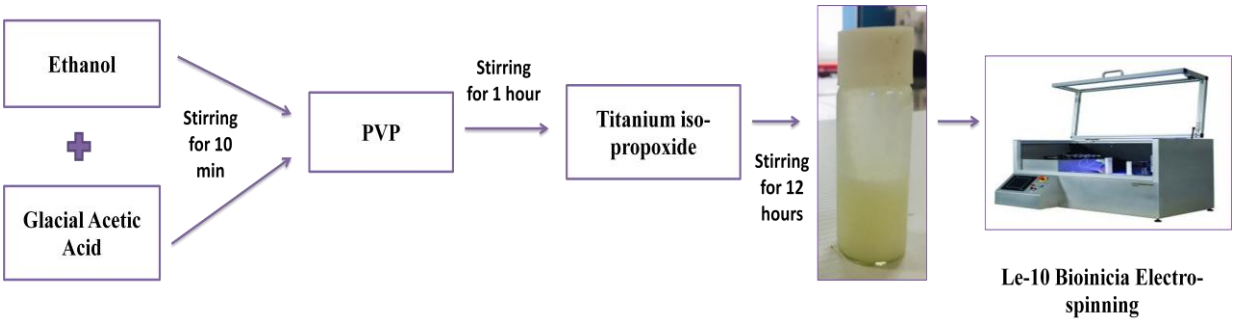

Figure 2: Synthesis procedure for deposition of TiO2 nano-fibres on FTO glass

Aluminium foil and FTO was attached to the collector plate via a conductive carbon tape. In this research, high voltage was attached to the needle and the solution was injected to the needle at the feed rate of 750µl/h. The needle collector distance was set at 15cm. A stable taylor cone can be seen at the tip of the needle. The sample was deposited for 45 minutes at ambient temperature. The as-spun fibres deposited on FTO were dried for 1 hour at 100^{o}C in a vacuum oven. The heating rate was set at 1^{o}C/min. The dried nano-fibres were calcinated at 450^{o}C for 1 hour in a Tube furnace in Air. To reach the calcination temperature a heating rate of 3◦C/min was maintained. The isothermal plateau was maintained for 60 minutes and subsequent cooling was at the natural rate.

2.1 Characterization of TiO2 Fibers:

The structure and morphology of TiO_2 nanofiber were characterized by different techniques. The morphology was imaged by using Optical Microscopy (EQ MM-500T) using scope-tek software and Vega3 Tescan scanning electron microscope (SEM). The crystallinity was studied using D8 advanced X-Ray Diffractro-meter. The optical properties were studied using UV-3600 plus UV-VIS NIR Spectrophotometer.

3. Results and Discussions:

The as-spun TiO2 nano-fibers were first dried at 100°C to remove the volatile impurities and polymer. This is followed by annealing at 450°C for 2 hours. Figure 3 (a) shows XRD pattern of TiO2 nano-fibers after drying at 100^{o}C. There is no major peak which shows that there is not any phase of TiO2 present. Figure 3 (b) shows XRD pattern of TiO2 nano-fibres annealed at 450°C for 2 hours. X-ray diffraction spectrum of TiO2 nano-fibers showed major anatase peaks at 25.3°.The nano-fibers show amorphous peaks[10]. This amorphous behaviour is because after annealing certain tanglement of TiO2 fibres take place because of the evaporation of the polymer with disturb the periodicity. Now the atoms of TiO2 are not randomly distributed. X-rays will be scattered in many directions leading to an uneven distribution of particles in a wide range (2 Theta) instead of high intensity narrower peaks(like crystalline structures). Figure 3 (c) shows major peaks of TiO2 nano-fibres annealed at 500^{o}C. The peaks and phases are close to the reported value. The lattice parameters of the anatase phase of TiO2 were calculated to be a) 3.517 Å and c) 9.016 Å, which is quite close to the reported values (JCPDS Card number 21-1272) [11]. The TiO2 phase change from anatase to rutile occurs after 450^{o}C.

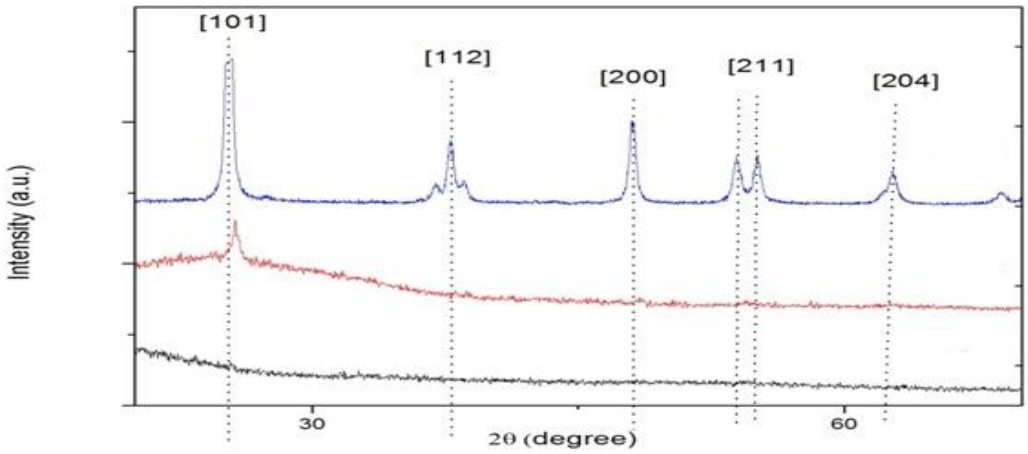

Figure 3 (a) XRD of as-spun TiO2 nano-fibres after drying at 100^{o}C (a) XRD of TiO2 nano-fibres deposited on FTO, after drying at 100°C (b) XRD of TiO2 nano-fibres deposited on FTO, Annealed at 350^{o}C (JCPDS Card number -21-1272) (c)) XRD of TiO2 nano-fibres deposited on FTO, Annealed at 450^{o}C

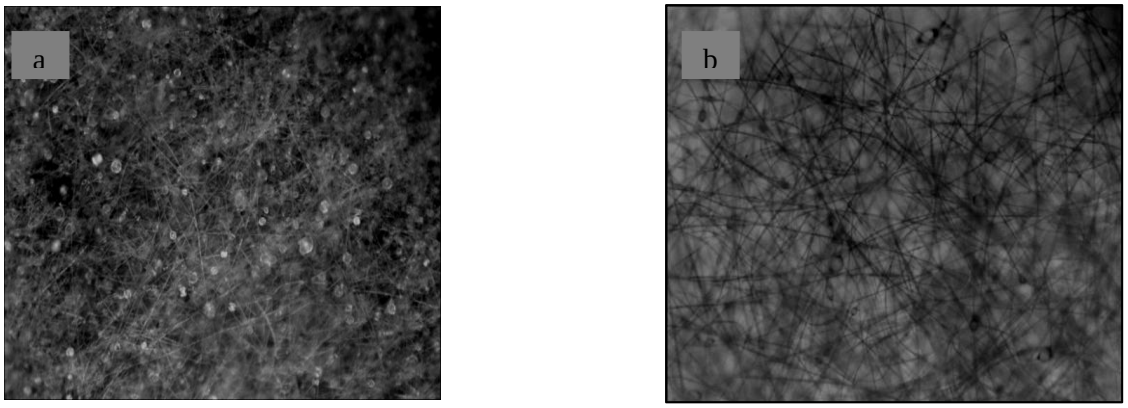

Figure 4: OM Images of as-spun nano-fibres on FTO glass (a) 20X Magnification (b) 50X magnification

The morphology of as-spun nano-fibres was characterized by using optical microscope (MM-500T). In Figure 4 (a) at 20X magnification there are various beads structures but a network of smooth fibres can be seen. In Figure 4 (b) at 50X magnification, there is a smooth net of fibres. The fibres are continuous and of very small diameter.

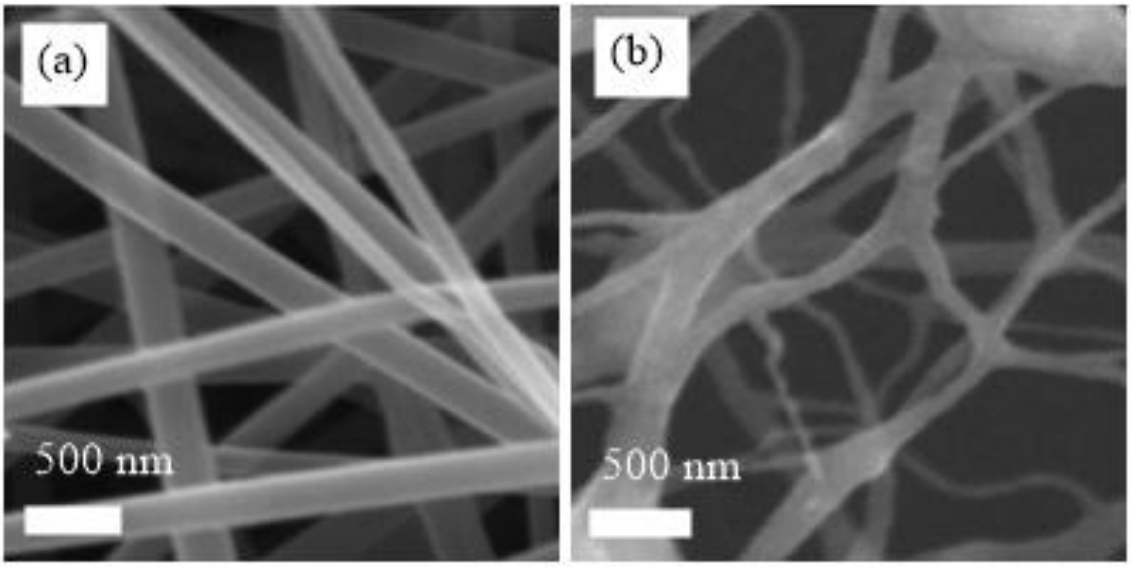

Figure 5: (a) TiO2 nano-fibres after drying at 100^{o}C for 1 hour. (b) TiO2 nano-fibres after annealing at 450^{o}C

Figure 5 (a) SEM image of TiO2 nano-fibres after drying at 100^{o}C for 1 hour. This drying is carried out for the evaporation of all the solvents (ethanol and glacial acetic acid). The fibres are smooth and continuous. There are several bead structures which are because of the high viscosity of the precursor solution. It is reported that the factors that are involve in formation of beads include viscosity and surface tension of the precursor solution inserted in the syringe [12]. Moreover the diameter of the fibres before annealing ranges from 100nm to 200nm as shown in figure 6 (a). There is a decrease in diameter of the fibre but the beads structures remains. The fibres are round shaped. These structures appear after annealing at 450^{o}C. After annealing the fibres diameter decrease due to evaporation of polymer PVP and due to heating

at high temperature, the fibres were tangled together and the morphology of fibres changes

from fibrous to flat materials [10]. The fibres are not smooth and continuous. The fibre diameter after annealing decreases to 50nm to 100nm as shown in Figure 6 (b). Most of the fibres lay in diameter range of 70nm to 100nm after annealing. Decrease in fibre diameter will give more space for dye loading which increases the efficiency of the cell.

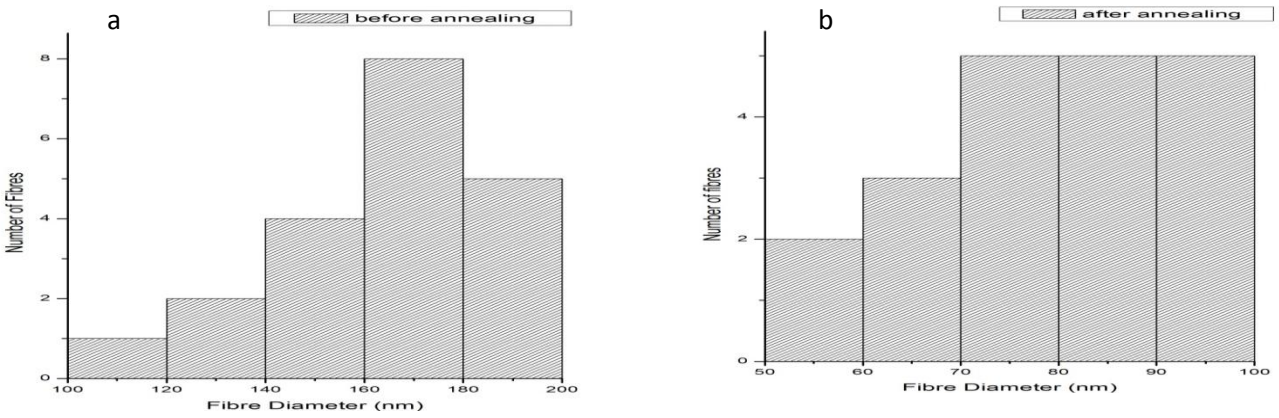

Figure 6: (a) Diameter of fibres before annealing TiO2 nanofibres at 450^{o}C for 1 hour (b) diameter of fibres after annealing TiO2 nanofibres at 450^{o}C for 1 hour

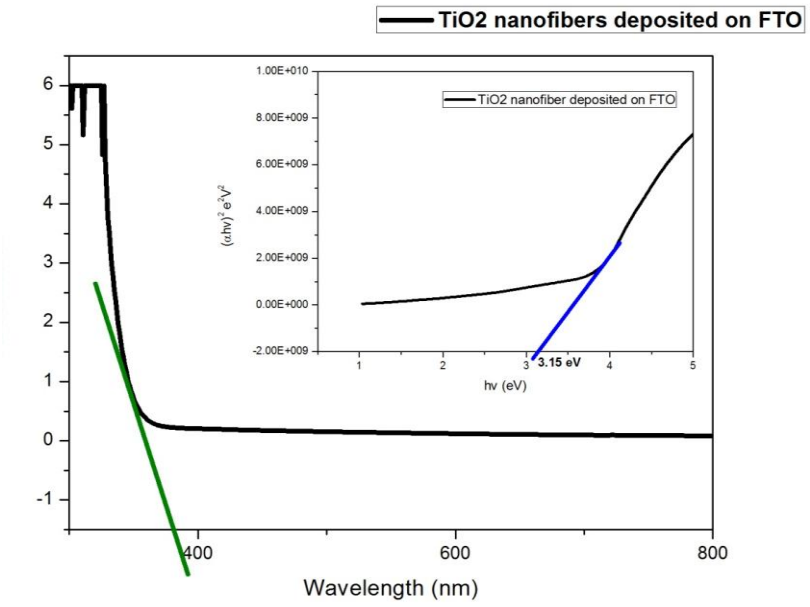

Figure 7: Absorption spectrum of TiO2 nano-fibres and tauc plot of TiO2 nano-fibres extracted from absorption spectrum for band-gap calculation.

The UV-Vis spectra of the electro-spun TiO2 film deposited on FTO glass were studied using UV-3600 plus UV-VIS NIR spectrophotometer from wavelength ranging from 300nm to 800nm. The absorption curve is shown at 390nm in figure 7, which means TiO2 gives absorption in visible region. Using the graph between absorption and wavelength, Eg(band-gap) was calculated by using transmittance. $\%T=(\log_{10}^{-A})/100$ where A is the absorbance. $Eg=1240/\lambda(nm)$ where λ is the wavelength. And Eg (eV) is the band-gap. Absorption co-efficient was calculated using $\alpha = 1/t \ \ln(1/\%T)$, where %T is the % transmittance of the solution. The absorption mainly depends on the thickness of the film. With increase in thickness more dye molecules can be absorbed which can increase the absorption spectrum of the thin-film[13]. The band-gap of TiO2 nano-fibres deposited on glass gives a wider band-gap of 3.15eV. As compared to typical TiO2 nano-particles P25 having absorption offset at 370nm and band-gap of 3.22eV, there is a band-gap narrowing in case of TiO2 nano-fibres. This shift in the absorption offset is due to scattering of light not due to band-gap narrowing[14]. Moreover the P25 TiO2 nano-particles give absorption in ultra-violet region compared to TiO2 nano-fibres having absorption

offset in visible region. The visible light scattering in case of TiO2 nano-fibres will certainly increase the light absorbance in the photo-anode and thus enhance the device performance[14].

4. Conclusion:

TiO2 nano-fibres were successfully grown on FTO glass using solution Electro-spinning technique. XRD pattern give the confirmation of TiO2 anatase structure when compared with the dried TiO2 nano-fibre mat. The OM images and SEM images shows the formation of nano-fibres in diameter ranging from 50nm to 100nm. SEM images concluded that the nano-fibre diameter decrease after annealing at 450^{o}C for 1 hour which is because of the evaporation of all the solvents and polymer materials and the fibre structure changes to round like structures because of entanglement of fibres after annealing. The band-gap of the TiO2 nano-fibres was calculated to be 3.15eV and the fibres give absorption in visible region. More light absorbance will take place in visible region with maximum dye loading due to small diameter of the fibres.

5. Acknowledgments:

Authors wish to thank USAID and PGP NUST for their financial support to carry out this research. Special thanks to people at AEM&S for assistance and guidance during the use of lab equipments. We also want to thank Engr. Naveed Ahmed and Sir Qamar-ud-din for their help during the characterization of the samples and Dr. Muhammad Rafi from NILOP for his guidance.

References

[1] O. Jirsák and T. Dao, “Production, properties and end-uses of nanofibres,” *Nanotechnol. Constr. 3*, pp. 1–5, 2009.

[2] R. Rani and S. Sharma, “Preparation and Characterization of SnO 2 Nanofibers via Electrospinning,” *J. Adv. Nanoparticle*, vol. 5, no. February, pp. 53–59, 2016.

[3] D. H. Reneker and A. L. Yarin, “Electrospinning jets and polymer nanofibers,” *Polymer (Guildf).*, vol. 49, no. 10, pp. 2387–2425, 2008.

[4] B. Ding, C. K. Kim, H. Y. Kim, M. K. Se, and S. J. Park, “Titanium dioxide nanoribers prepared by using electrospinning method,” *Fibers Polym.*, vol. 5, no. 2, pp. 105–109, 2004.

[5] A. Wold, “Photocatalytic properties of titanium dioxide (TiO2),” *Chem. Mater.*, vol. 2912, no. 16, pp. 280–283, 1993.

[6] M. Zukalová, A. Zukal, L. Kavan, M. K. Nazeeruddin, P. Liska, and M. Grätzel, “Organized mesoporous TiO2 films exhibiting greatly enhanced performance in dye-sensitized solar cells.,” *Nano Lett.*, vol. 5, no. 9, pp. 1789–1792, 2005.

[7] A. FUJISHIMA and K. HONDA, “Electrochemical Photolysis of Water at a Semiconductor Electrode,” *Nature*, vol. 238, no. 5358, pp. 37–38, 1972.

[8] B. O’Regan and M. Gratzel, “A Low-Cost, High-Efficiency Solar-Cell Based on Dye-Sensitized Colloidal TiO_2 Films,” *Nature*, vol. 353, no. 6346, pp. 737–740, 1991.

[9] D. J. Lockwood and J. yu Bin Ding, *Electrospun Nanofi bers for Energy and Environmental Applications*. 2015.

[10] a Kumar, R. Jose, K. Fujihara, J. Wang, and S. Ramakrishna, “Structural and Optical Properties of Electrospun TiO 2 Nanofibers,” *Chem. Mater.*, vol. 19, no. 26, pp. 6536–6542, 2007.

[11] P. D. File, D. K. Smith, and R. Jenkins, “ICDD and the The Powder Diffraction File Past , Present and Future,” *Computer (Long. Beach. Calif).*, no. Icdd, pp. 1–17, 1941.

[12] D. Y. Lee, B. Kim, S. Lee, M. Lee, and J. Lee, “Titania Nanofibers Prepared by Electrospinning,” vol. 48, no. June 2006, pp. 1686–1690, 2006.

[13] S. Sumardiasih, W. M. Obina, N. A. Ilahi, R. Suryana, S. D. Hastuti, and F. Nurosyid, “International Conference on Recent Trends in Physics 2016

(ICRTP2016),” *J. Phys. Conf. Ser.*, vol. 755, p. 11001, 2016.

[14] F. H. Bijarbooneh *et al.*, “Structurally stabilized mesoporous TiO[sub 2] nanofibres for efficient dye-sensitized solar cells,” *APL Mater.*, vol. 1, no. 3, pp. 32106–32107, 2013.